Electrochemical Activation of Small Molecules by Monolayer Molybdenum Disulphide

HIU MING LAU

Supervised by Professor John S. Foord & Professor S.C. Edman Tsang



A thesis submitted in conformity with the requirements
for the degree of Doctor of Philosophy in Theoretical and Physical Chemistry

University of Oxford
Department of Chemistry
St Cross College

2019

Declaration

All research works reported in this thesis has not previously been accepted in substance for any degree and is not being concurrently submitted in candidature for any degree. This thesis is conducted by the author unless stated otherwise. All materials from other sources has been properly and fully acknowledged.

Hiu Ming Lau

Acknowledgments

This doctorate dissertation would never have been completed without the constant guidance, support, opportunities and advice from my supervisors, Prof. John S. Foord and Prof. SC Edman Tsang. Therefore, I have to express my most sincere gratitude to them. Their inexhaustible passion for science has also deeply inspired me to always stay diligent and enthusiastic in my future career and life.

I am thankful to all the members in both the JSF research group and SCET research group, past and present. Not only they have taught me valuable chemical knowledges and practical laboratory skills, they are also the important companions in my doctoral journey.

Throughout my doctoral studies, I received countless help from my research collaborators, the technicians in the Department of Chemistry and staffs from St. Cross College. For this, I would like to specially express my greatest appreciation to:

Ms. Xiao Wei Lu, Mr. Jiří Kulhavý, Ms. Jiaying Mo, Dr. Jianwei Zheng for insightful discussion on MoS_2;

Mr. Simon Wu, Dr. Tai-Sing Wu, and Prof. Yun-Liang Soo for technical assistance on XAS analysis;

Dr. Ryuichi Kato, Dr. Kazu Suenaga Soo for technical support on STEM imaging;

Dr. Lilin Lu and Dr. Matthew T. Darby for technical support and discussion on VASP simulation packages;

Dr. Emina Hadzifejzovic, Dr. Nick Rees, and Prof. Tim Claridge for technical assistance on NMR spectroscopy;

Mr. Jiawen Zhang, Prof. Kylie Vincent for technical supports on FTIR spectroscopy.

Last but not least, this thesis is dedicated to my family and friends for their endless love, support, and encouragement. They are the reasons of my happiness and I hope I have made them proud.

Abstract

Molybdenum disulphide (MoS_2) is an earth-abundant layered semiconductor that can be exfoliated into monolayer nanosheets. Due to its potential applications in catalysing electrochemical reactions, recent researches have been focused on modifying MoS_2 monolayer into a highly active and cost-effective heterogeneous electrocatalyst. In this thesis, high-quality monolayer MoS_2 with different polytypes was functionalised by doping different single heteroatoms onto the surface. Subsequently, the catalytic activity of as-modified MoS_2 samples for electrochemical hydrogen production (HER) and carbon dioxide reduction (CO_2RR) was examined. In-depth characterisations with the support of computational simulations were conducted to investigate their structural and electronic properties.

MoS_2 nanosheets with the semiconducting polytype (2H), prepared via BuLi exfoliation of bulk MoS_2, have been doped with single transition metal atoms to produce 2D monolayer catalysts used for the electrochemical hydrogen evolution reaction. High-angle annular dark-field imaging scanning transmission electron microscopy (HAADF-STEM) show the direct proof of single transition metal atoms reside on the surface basal sites. The incorporated atoms subtly modify the electrocatalytic activities of the monolayer MoS_2, which is dependent on their electronic and stereospecific properties. It is found that these dopants play important roles in tuning the hydrogen adsorption enthalpies on exposed surface S atoms and Mo atoms in HER. Electrochemical testing, characterization and computational modelling demonstrate that Co dopants can significantly enhance the HER activity by the dominant Co-S interaction whereas Ni dopants substantially lowers the HER rate due to the Ni-Mo interaction on the same basal site. The two transition metal dopants show opposite doping behavior even though they are neighbors in the periodic table.

The study of the uncommon metallic MoS_2 and particularly the doping effect with transition metal (TM) is rather limited due to the instability of this polytype (1T) at high temperature. A simple ambient temperature modification method using sonication was developed to dope the monolayer metallic MoS_2 with various TM precursors. It is found that 1T-$^{S}MoS_2$ is more superior than corresponding semiconducting monolayer MoS_2 (2H-$^{S}MoS_2$) and the inclusion of 3 wt% Pt or Pd can also further enhance the HER activity. Scanning transmission electron microscopy coupled with electron energy loss spectroscopy (STEM-EELS) and X-ray adsorption spectroscopy (XAS) show the active single TM atom doping on this surface is to account for the high activity. Kinetic and density functional theory (DFT) analyses also illustrate that the metallic nature of 1T-$^{S}MoS_2$ greatly facilitates the first proton reduction step from water, rendering it non-rate limiting as contrast to that of 2H-$^{S}MoS_2$. The inclusion of TM single doper such as Pd, despite at low loading, can offer the dramatic acceleration on the rate limiting recombination of H to H_2. As a result, a bifunctional catalysis for HER over this tailored composite structure is demonstrated. The electrocatalytic ability of heteroatoms doped 1T-$^{S}MoS_2$ was further tested for electrochemical CO_2RR. Electrochemical system coupled with in-situ Fourier-transform infrared spectrometer (FTIR) shows that *CO intermediate formed on the Re and In doped 1T-$^{S}MoS_2$ can be further reduced into hydrocarbons upon increasing the applied potential, suggesting that the reaction is potential dependent. The NMR results suggested that Re and In can help to facilitate the production of higher-order alcohols from the CO_2RR. DFT calculations demonstrated that the incorporation of these two single atom dopants does not encourage the competitive hydrogen evolution reaction while facilitate CO_2RR in our aqueous electrochemical system.

Preface

This thesis is a collection of three selected chemistry projects conducted by the author during his PhD studies at University of Oxford from 2015 to 2019. All the three project chapters are interrelated as they all involve studying electrochemical systems catalysed by single atoms doped molybdenum disulphide monolayer nanosheets. Since results presented in early chapters will be discussed again in latter analysis, readers are expected to study the thesis in chronological order to grasp a clearer picture.

Chapter 1 first introduces background of molybdenum sulphide. It is then followed by reviewing recent advances in single atom electrocatalysis of monolayer materials for electrochemical applications.

Chapter 2 describes the details of experimental theories and techniques employed in all of the included experiments.

Chapter 3 first studies the doping effect of Co and Ni atoms on semiconducting molybdenum sulphide monolayers for electrochemical hydrogen production. The results of this project have been published in the following scientific journal:

Lau, T. H. M.; Lu, X.; Kulhavý, J.; Wu, S.; Lu, L.; Wu, T. S.; Kato, R.; Foord, J. S.; Soo, Y. L.; Suenaga, K.; Tsang, S. C. E. Transition Metal Atom Doping of the Basal Plane of MoS_2 monolayer Nanosheets for Electrochemical Hydrogen Evolution. Chem. Sci. 2018, 9, 4769–4776.

Chapter 4 further investigates the structure-activity relationship of Pd, and Pt doped metallic molybdenum sulphide monolayers for electrochemical hydrogen production. The results of this project have been published in the following scientific journal:

Lau, T. H. M.; Wu, S.; Kato, R.; Wu, T.-S.; Kulhavý, J.; Mo, J.; Zheng, J.; Foord, J. S.; Soo, Y.-L.; Suenaga, K.; Darby, M. T.; Tsang, S. C. E. Engineering Monolayer 1T-MoS_2 into a Bifunctional Electrocatalyst via Sonochemical Doping of Isolated Transition Metal Atoms. ACS Catal. 2019, 9, 7527–7534.

Chapter 5 studies the catalytic behaviour of Re, and In doped metallic molybdenum sulphide monolayers for electrochemical carbon dioxide reduction.

Chapter 6 concludes the thesis and suggests possible future works.

Table of Contents

Chapter 1: Introduction

1.1. Molybdenum Disulphide 1

1.1.1. Polytypes of MoS_2 2

1.2. Single layered MoS_2 ($^{S}MoS_2$) 5

1.2.1. Synthetic Methods of $^{S}MoS_2$ 7

1.2.2. Modifying SMoS2 for improved electrocatalytic reactions 9

1.3. Electrochemical Hydrogen Evolution Reaction 13

1.3.1. Introduction to Electrochemical HER 14

1.3.2. Key Parameters for HER Catalyst Evaluation 16

1.4. Recent Development of Heteroatoms doped Monolayer Materials for HER 19

1.4.1. Graphene-based materials 20

1.4.2. Graphitic Carbon Nitride 21

1.4.3. MoS2 22

1.5. Electrocatalytic Carbon Dioxide Reduction Reactions 26

1.5.1. Introduction to Electrochemical CO_2RR 27

1.5.2. Key parameters for CO_2RR Catalyst Evaluation 29

1.5.3. The CO_2 Reduction Reaction 30

1.5.4. Possible Reaction Pathways of CO_2RR 31

1.6. Recent Development of Heteroatoms doped Monolayer Materials for CO_2RR 35

1.6.1. Graphene Based Materials 36

1.6.2. MoS_2 Monolayers 37

1.7. Scope of Research 38

1.8. Reference 39

Chapter 2: Experimental Theories and Techniques

2.1. Chapter Overview 44

2.2. Microscopic Techniques 44

2.2.1. Atomic Force Microscopy 45

2.2.2. Transmission Electronic Microscopy 46

2.2.3. High-Angle Annular Dark-Field Scanning transition electron microscopy 47

2.3. Spectroscopic Techniques 49

2.3.1. X-ray Photoelectron Spectroscopy 49

2.3.2. X-ray Absorption Spectroscopy 50

2.3.3. Electron Paramagnetic Resonance 52

2.3.4. Nuclear Magnetic Resonance Spectroscopy 53

2.3.5. Fourier-Transform Infrared Spectroscopy 54

2.4. Electrochemical Theories and Methods 55

2.4.1. Electrochemical Equilibrium 55

2.4.2. Electrode Kinetics 56

2.4.3. Modes of Mass Transport 58

2.4.4. Faradaic and Nonfaradaic Processes 60

2.4.5. Electrochemical Cell 61

2.4.6. Electrochemical Techniques 62

2.5. Computational Chemistry 64

2.5.1. Schrödinger Equation 64

2.5.2. Density Functional Theory 65

2.6. Reference 67

Chapter 3: Hydrothermal Deposition of Single Transition Metal Atoms on 2H Molybdenum Disulphide Monolayers for Electrochemical Hydrogen Evolution Reaction

3.1	Introduction	68
3.2	Experimental Details	71
	3.2.1. Synthesis of $^{S}MoS_2$	71
	3.2.2. Synthesis of TM-$^{S}MoS_2$	71
	3.2.3. Electrochemical Cell	72
	3.2.4. Density Functional Theory	73
3.3	Structural Analyses of $^{S}MoS_2$ and TM-$^{S}MoS_2$	74
	3.3.1. Morphology of $^{S}MoS_2$	74
	3.3.2. Thickness Determination of Exfoliated $^{S}MoS_2$	75
	3.3.3. Sulphur Defects on $^{S}MoS_2$	76
	3.3.4. Doping Concentration of Transition Metals	77
3.4	Electrochemical Testing for Hydrogen Production	78
	3.4.1. Linear Sweep Voltammetry	78
	3.4.2. Tafel Analysis of Co-$^{S}MoS_2$ and Ni-$^{S}MoS_2$	79
	3.4.3. Stability Test of Co-$^{S}MoS_2$ and Ni-$^{S}MoS_2$	80
3.5	Doping Environment of isolated TM atoms	81
	3.5.1. HR-STEM images	81
	3.5.2. EXAFS	86
3.6	The role of single TM atoms for H adsorption	88
3.7	Conclusions	92
3.8	References	93

Chapter 4: Sonochemical Doping of Single Transition Metal Atoms on 1T Metallic Molybdenum Disulphide Monolayers for Electrochemical Hydrogen Evolution Reaction

4.1	Introduction	99
4.2	Computational and Experimental Details	103
	4.2.1. Synthesis of single transition metal atoms doped 1T monolayer MoS_2	103
	4.2.2. Electrochemical Measurement	103
	4.2.3. Density Functional Theory	104
4.3	Structural Characterisation of 1T-TM-$^{S}MoS_2$	106
	4.3.1. HR-STEM images with HAADF	106
	4.3.2. Chemical Environment of Pt and Pd adatoms	111
4.4	Electrochemical analysis for HER	116
	4.4.1. Electrocatalytic Performance and Stability of Catalyst	116
	4.4.2. Tafel Analysis of TM-1T-$^{S}MoS_2$	118
4.5	HER Mechanism of 1T- $^{S}MoS_2$	119
	4.5.1. Adsorption of H on 1T- $^{S}MoS_2$	119
	4.5.2. Recombination of H* on 1T- $^{S}MoS_2$	121
4.6	HER Mechanism of TM- doped 1T- $^{S}MoS_2$	124
	4.6.1. Adsorption of H on TM- doped 1T- $^{S}MoS_2$	124
	4.6.2. Recombination of H* on TM-1T- $^{S}MoS_2$	128
4.7	Conclusions	132
4.8	References	133

Chapter 5: Rhenium and Indium doped 1T-$^{S}MoS_2$ for Electrochemical Reduction of Carbon Dioxide

5.1. Introduction 137

5.2. Computational and Experimental Details 139

5.2.1. Electrochemical Measurement 139

5.2.2. Density Functional Theory 140

5.3. Structural Characterisation of Re and In doped 1T-$^{S}MoS_2$ 142

5.4. Electrochemical analysis of Re and In doped 1T-$^{S}MoS_2$ for CO_2RR 146

5.5. Product Analysis by Liquid ^{1}H NMR 149

5.6. The function of Re and In dopants on 1T-$^{S}MoS_2$ for electrochemical CO_2RR 153

5.6.1. Competitive Hydrogen Evolution Reaction 153

5.6.2. Reducing Adsorbed CO 154

5.7. Conclusions 155

5.8. References 156

Chapter 6: Conclusion and Future Works

6. Conclusions and Future Works 159

Abbreviations

Abbreviations	Meaning
HER	Hydrogen evolution reaction
CVD	Chemical vapour deposition
CO_2RR	Carbon dioxide reduction reaction
OER	Oxygen evolution reaction
TOF	Turnover frequency
ECSA	Electrochemical active surface area
DFT	Density functional theory
RDS	Rate determining step
FE	Faradaic efficiency
AFM	Atomic force microscopy
TEM	Transmission electron microscopy
HAADF-STEM	High-angle annular dark-field scanning transition electron microscopy
XPS	X-ray photoelectron spectroscopy
XAS	X-ray absorption spectroscopy
XANES	X-ray absorption near-edge structure
EXAFS	Extended X-ray absorption fine structure
WT	Wavelet transform
EPR	Electron paramagnetic resonance
NMR	Nuclear magnetic resonance
FTIR	Fourier transform infrared spectroscopy
EDL	Electrical double layer
IHL	Inner Helmholtz layer
OHL	Outer Helmholtz layer
LSV	Linear sweep voltammetry
LDA	Local density approximation
GGA	Generalised gradient approximation

Abbreviations	Meaning
RHE	Reversible hydrogen electrode
VASP	Vienna ab initio simulation packages
PBE	Perdew-Burke-Ernzerhof functional
PAW	Projector-augmented wave
DOS	Density of states
HRTEM	High resolution transmission electron microscopy
ICP-MS	Inductively coupled plasma mass spectrometry
ADF	Annular dark-field
EELS	Electron energy loss spectroscopy
VB	Valence band
CB	Conduction band
TM	Transition metal
SSNMR	Solid-state nuclear magnetic resonance

Chapter 1

Introduction

1.1. Molybdenum Disulphide

Molybdenum Disulphide is an inorganic compound with a chemical formula of MoS_2. Pure MoS_2 is generally obtained via simple mechanical processing of the earth abundant molybdenite ores. The physical properties of MoS_2 are very similar to that of graphite and it is hard to differentiate between the two without specific experiments. Both of them have a slivery black appearance and a layered chemical structure of which individual layers stack upon each other. These layers are held only by weak van der Waals force which makes both materials very low in hardness. They are also relatively inactive to dilute acids and oxygen. Thanks to all these properties, graphite and MoS_2 are often used as solid lubricants[1] for engineering and industrial applications.

In 2004, single atomic thick crystal graphite, also known as graphene, was successfully isolated from bulk graphite[2]. Graphene offers impressive material properties that far exceed those of graphite. It is considered to be the strongest material ever recorded and it also possesses excellent heat and electrical conductivity. This discovery prompted intensive research on utilising graphene in different scientific and industrial applications. Developing other two-dimensional materials has also become an emerging research direction in recent years. As the inorganic analog of graphene, single layered MoS_2 ($^{s}MoS_2$) can also be isolated from bulk MoS_2. When comparing to its bulk counterpart, $^{S}MoS_2$ possesses superior electronic, optical, mechanical, and catalytic properties that are important for sensing[3,4], catalysis[5,6], and energy storage applications[7,8]. This discovery

also opens new opportunities for monolayer MoS_2 materials as heterogeneous catalyst in the production of chemicals. From this perspective, we will be investigating adatoms functionalised $^{S}MoS_2$ for electrocatalytic reactions. Further details regarding the material properties of MoS_2 will therefore be discussed in following sections.

1.1.1. Polytypes of MoS_2

Based on previous research, there are three common polytypes (allotrope) of MoS_2 reported: 2H-MoS_2 (2-layers hexagonal system), 3R-MoS_2 (3-layers rhombohedral system) and 1T-MoS_2 (1-layer tetrahedral system). (Figure 1.1) Naturally occurring MoS_2 crystals found in molybdenite ores have the 2H phase while both 3R-MoS_2 and 1T-MoS_2 are metastable and usually are only obtained via phase transition in chemical reactions. Structural details of each poly-type will be described separately here.

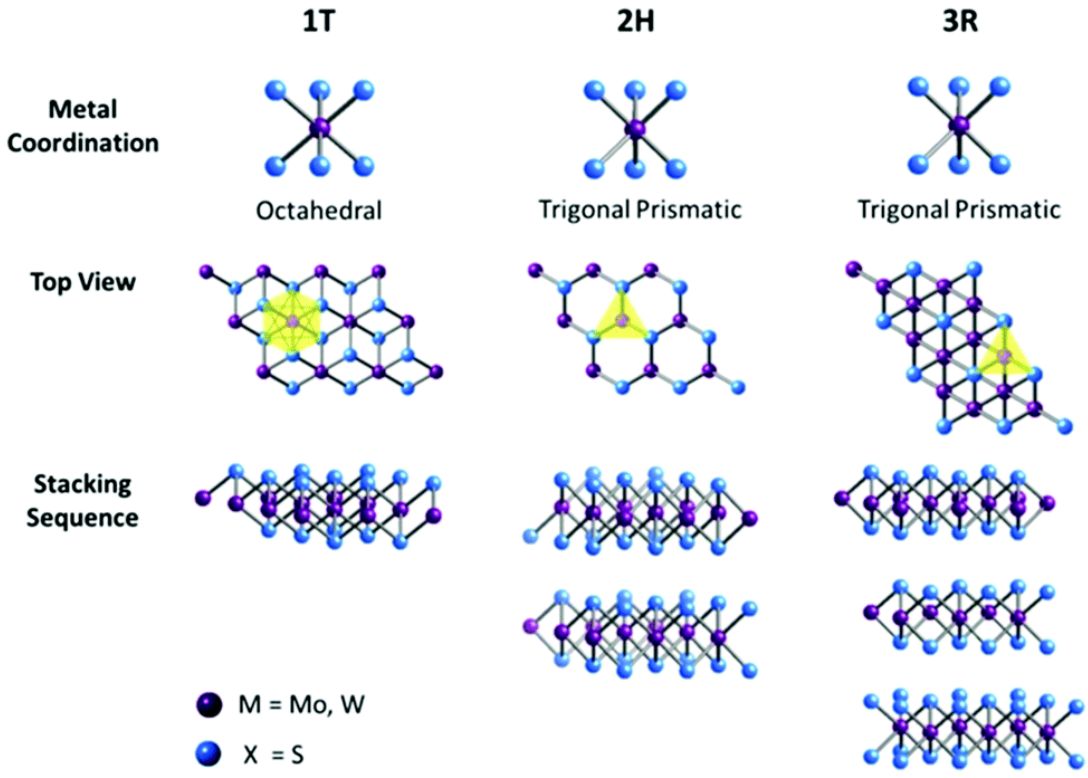


Figure 1.1 Structures of different polytype of MoS2. Reprinted with permission from Ref[9]

1.1.1.1. **Chemical Structure of 2H-MoS_2**

2H-MoS_2 (Space group: P63/mmc, Stacking order: AbA BaB) is the most stable among the three allotropes. A single tri-atomic 2H-MoS_2 layer consists of a hexagonal plane of molybdenum atoms sandwiched between two other hexagonal planes of sulphur atoms via strong in-plane covalent bondings. Each Mo atom is located at the centre of the trigonal prism coordination and surrounded by six S atoms. 2H-MoS_2 has a unit cell in which two layers are stacked in hexagonal symmetry. Adjacent layers are then held by weak out-of-plane van der Waals interactions.[10] 2H-MoS_2 is a semiconductor with an indirect band gap of approximately 1.2eV. The semiconducting features come from the induced splitting of the hexagonal symmetry, where the five Mo4d (d_{xz}, d_{yz}, $d_{x^2-y^2}$, d_{xy} and d_{z^2}) orbitals are split into three groups of closely spaced energies (occupied d_{z^2}, partially occupied $d_{x^2-y^2}$, d_{xy}, and unoccupied d_{xz}, d_{yz}) (Figure 1.2).

1.1.1.2. **Chemical Structure of 3R-MoS_2**

Both 2H-MoS_2 and 3R-MoS_2 have the same trigonal prismatic configuration of Mo atoms surrounded by 6 S atoms within layers. However, 3R-MoS_2 (Space group: R3m, Stacking order: AbA BcB CaC) has a unit cell in which three layers are stacked in rhombohedral symmetry, i.e. adjacent layers are displaced slightly from each other without any rotation. Due to their similar structure, both 2H-MoS_2 and 3R-MoS_2 are semiconductors. 3R-MoS_2 is metastable and it can only be observed under high pressure condition. However, 3R-like stacking defects can also be found commonly in 2H-MoS_2 nanostructures.[11]

1.1.1.3. **Chemical Structure of 1T-MoS2**

For 1T-MoS_2 (Space group: P3m1, Stacking order: AbC), one of its S atom layers is distorted with respect to the Mo layer. Due to such structural modification, the original trigonal prismatic unit cell of monolayer 2H-MoS_2 becomes an octahedral coordination system of Mo atoms. Each Mo is located at the centre of this octahedral configuration and

is evenly surrounded by six S atoms. Density of state (DOS) of 1T-MoS_2 from computational calculations show that the Mo 4d states form a single wide band near the Fermi level.[2] According to crystal field theory, the origin of this band is due to octahedral symmetry splitting of Mo 4d orbitals into two different groups (degenerated Mo 4d $d_{xy,}$ $d_{yz,}$ d_{zx} with two electrons occupied and unoccupied Mo 4d d_{z2}, $d_x2\text{-}_y2$) (Figure 1.2). This also explains the paramagnetic behaviour of 1T-MoS_2. Unlike 2H-MoS_2 and 3R-MoS_2, 1T-MoS_2 is metallic and possesses an electrical conductivity of around 10^7 times higher than that of 2H-MoS_2.[12] All the basal S atoms can accept and donate electrons like a metal surface. The 1T phase is also thermally metastable and can easily be converted back to 2H-MoS_2 if heated above 95°C.[13]

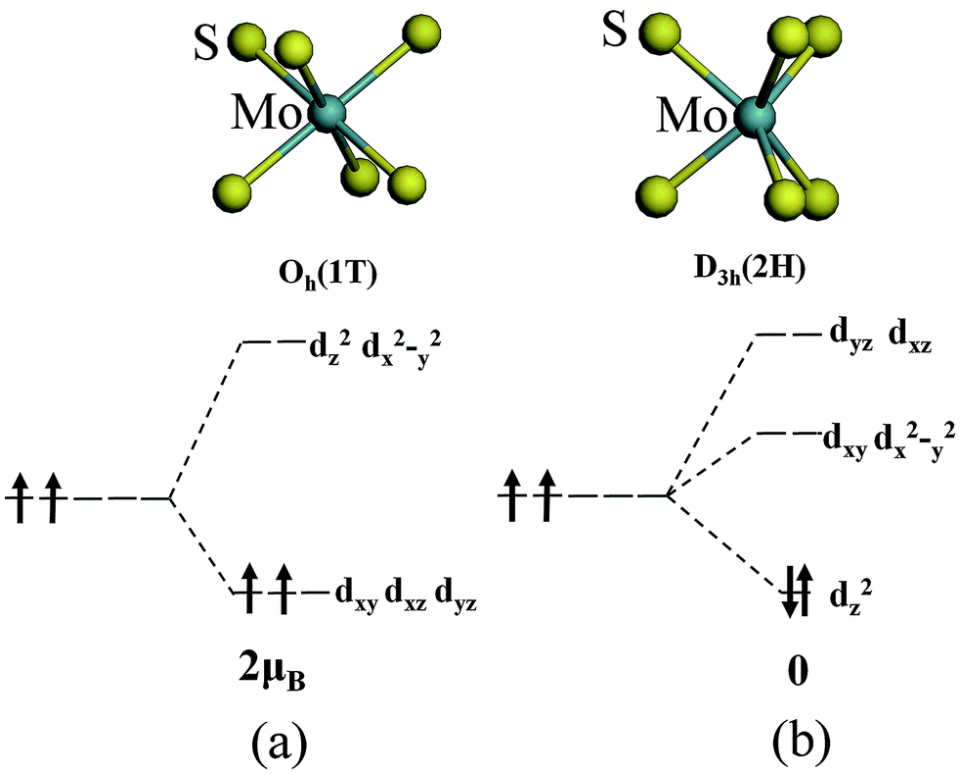


Figure 1.2 The Mo 4d orbits under the crystal fields of (a) 1T phase and (b) 2H. Reprinted with the permission from Ref[14].

1.2. Single layered MoS_2 ($^{S}MoS_2$)

While graphene is an excellent catalyst support because of its excellent electrical conductivity and large surface area, it is a zero band gap material and it provides nearly no catalytic activity without any prior functionalisation. In contrary, ultrathin 3R and 2H-MoS_2 can function as a semiconducting heterogeneous catalyst for various photoelectrical and electrochemical reactions. Previous results also suggested that the Mo edges **$(10\bar{1}0)$** and the S edges **$(1\bar{0}10)$** of MoS_2 particles are the two predominant active sites for most electrochemical reactions (Figure 1.3).[15] These edge sites can accept and donate electrons like a metal surface during reactions. Since they are preferentially exposed for reaction, it is one of the reasons why the thin 2H-MoS_2 shows the overall better performance in electrochemical catalysis. Conversely, the basal plane **(0001)** of 2H-MoS_2 has been verified to be chemically inert by experimental and computational analyses and thus is usually ignored as a contributor to catalytic activities.[16] This also explains why bulk MoS_2 exhibits poor electrochemical activity.

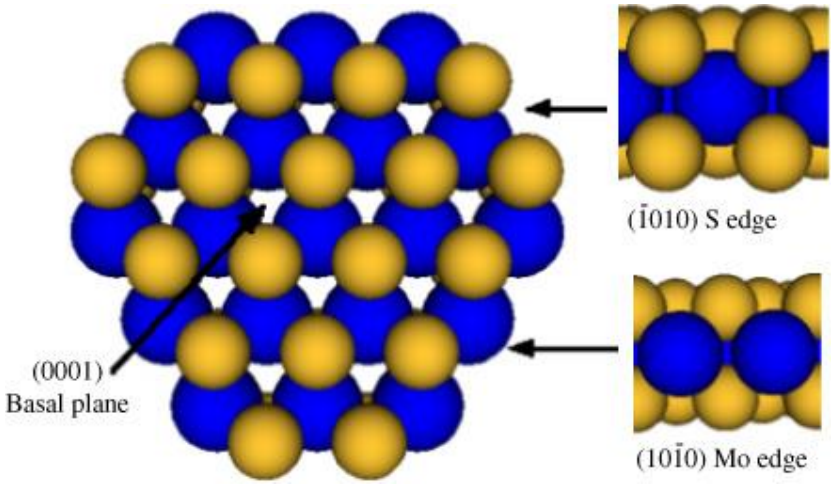


Figure 1.3 Structure of single 2H-MoS_2. Reprinted with permission from Ref[17].

However, the number of basal sites is far larger than edge sites, especially when MoS_2 becomes monolayer. This is the reason why many strategies were employed in the last

decades to create multi-layered MoS_2 nanomaterials by maximizing the ratio of exposed edge sites to inert basal sites. These strategies include the use of physical methods such as microwave plasma process[18], pulsed laser vaporisation[19], arc-discharge techniques[20], mechanical liquid exfoliation etc.; as well as chemical methods like thermal annealing[21], solvothermal[22] and hydrothermal[23] synthesis etc. Among all the polytypes, 2H-MoS_2 is by far the more popular one since it is more thermodynamically stable and economically viable. Although 3R-MoS_2 may have a higher catalytic activity for electrochemical hydrogen evolution reaction[9], the high pressure experimental and synthetic conditions required to preserve the metastable 3R phase make it less favourable in research studies. Also, while 1T-MoS_2 has been proved computationally to possess a metallic surface, it is challenging to further functionalise the material properties due to its metastability; any vigorous reaction conditions above 95^{o}C can potentially convert 1T phase back to 2H.[13]

Recently, it has been demonstrated experimentally and computationally that the 2H-MoS_2 basal plane can be activated by generating S defects on the surface, which renders the material highly active for the hydrogen evolution reaction (HER).[24] The S atoms near the defects behave like an exposed Mo edge sites which can help catalysing electrochemical reactions[24–26]. The synthesis functionalised $^{S}MoS_2$ therefore becomes an attractive topic once again. In this section, we will discuss techniques employed in synthesising and functionalising $^{S}MoS_2$. It should be noted that when we discuss $^{S}MoS_2$ here, we refer to triatomic MoS_2 layers with either a trigonal prismatic or an octahedral Mo atom coordination (1T). A single triatomic layer with trigonal prismatic Mo system can actually be regarded as another special polytype called 1H (one-layer, hexagonal system) but in this thesis we refer to both phases as “2H” and do not distinguish between the two to avoid unnecessary complications.

1.2.1. Synthetic Methods of $^{S}MoS_2$

Top-down and bottom-up methods are two major approaches to synthesise monolayer MoS_2. The top-down method is to isolate single MoS_2 layers from bulk MoS_2. This is usually done by weakening the interlayer van der Waals interactions. For the bottom-up method, single layered MoS_2 is synthesised by reacting Mo precursors such as MoO_3 with S sources to create MoS_2 from scratch. The bottom-up method is usually adopted in nanofabrication as the nanostructures created generally have fewer defects. In our case, the presence of defects, however, would actually help to expose active sites and boost the overall catalytic performance as aforementioned. It should be noted that in this thesis we would like to investigate triatomic-thick single-layered MoS_2 rather than multi-layered MoS_2. A reliable synthetic method for monolayer materials usually involves chemical interactions at atomic levels with precise control. If not, the product will become a mixture of layers with a wide range of thickness. For example, liquid-phase exfoliation method utilises sonochemistry to mechanically break bulk MoS_2 into thinner slabs.[27] While this method can produce high quality $^{S}MoS_2$, the yield of the monolayers is low. Therefore, we will be discussing two major reproducible methods to produce $^{S}MoS_2$.

1.2.1.1. **Chemical vapour deposition**

Chemical vapour deposition (CVD) is a bottom-up method that has long been used to synthesise layered materials such as graphene. The same technique can therefore be applied in synthesising $^{S}MoS_2$. Mo precursors such as MoO_2, MoO_3, and $MoCl_5$ etc. are first placed in a high temperature furnace up to around 700^{o}C to 800^{o}C, together with a substrate such as Si, SiO_2, and Al_2O_3 etc. [28–31] (Figure 1.4) Sulfurization takes place once the S source such as S powder, H_2S, or vaporised S is carried by Ar to the Mo precursors. The MoS_2 monolayers will be directly deposited onto the substrate. A magnet can be placed at the furnace tube entrance to remove any unwanted metal content. The MoS_2

layer product can be directly released from the substrate for further fabrication or functionalisation. The morphology, size and thickness of the as prepared thin MoS_2 layers can be fine-tuned accordingly through precise control of (1) the reaction condition such as temperature, humidity and pressure, (2) the size of the substrate, (3) the molecular size of the Mo and S source, and (4) flow of the carrier gas.[32]

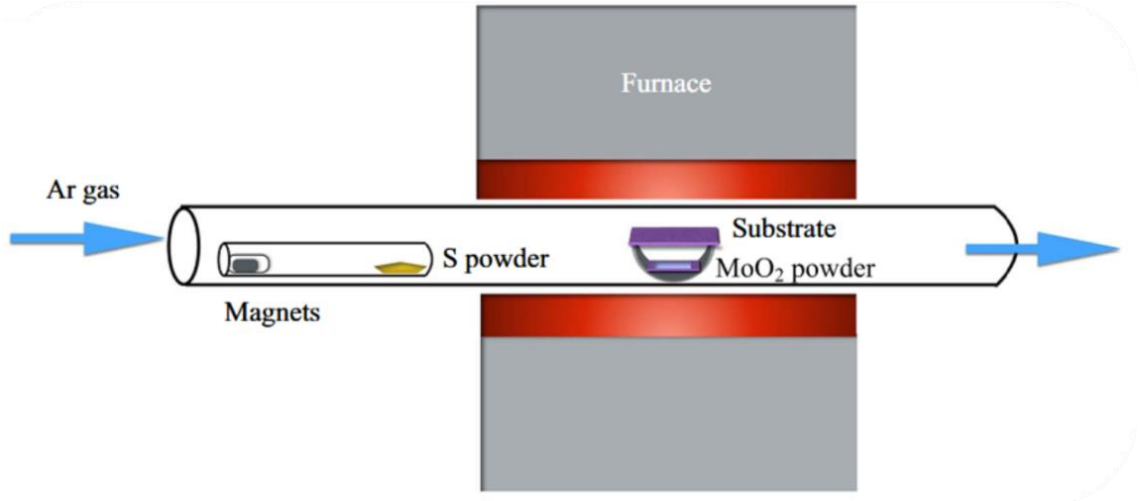


Figure 1.4 Schematic of a CVD setup for $^{S}MoS_2$ synthesis. Adapted with Permission from Ref.[28]

1.2.1.2. Sonication-assisted Alkali Metal Intercalation

Intercalation of alkali metal is the most common top-down method to synthesise $^{S}MoS_2$. Bulk MoS_2 powder is first soaked in a compound containing the intercalating alkali metal ions (e.g. K^+, Na^+, Li^+) with stirring in an inert atmosphere. During the intercalation process, electrons from the alkali metal transfers to the d orbital of the Mo centre. This results in diffusion of alkali metal atoms into the MoS_2 structure, forming an intercalated MoS_2 (Li_xMoS_2 ,Na_xMoS_2 or K_xMoS_2) with a destabilised lattice.[33] Further interaction (agitation) with water in a sonication bath creates an expansion of interlayer spacing which ultimately exfoliates the bulk 2H-MoS_2 into monolayer 1T-MoS_2.[34,35] The $^{S}MoS_2$ produced with this method is usually defected due to the vigorous exfoliation process. However, this wet chemistry method is also scalable and can yield a large amount of high quality monolayer MoS_2. The size of the monolayer nanosheets and the amount of defects

can also be controlled by the amount of (1) alkali metal ions and (2) bulk MoS_2 and (3) the sonicating power and (4) sonication frequency.[34,35]

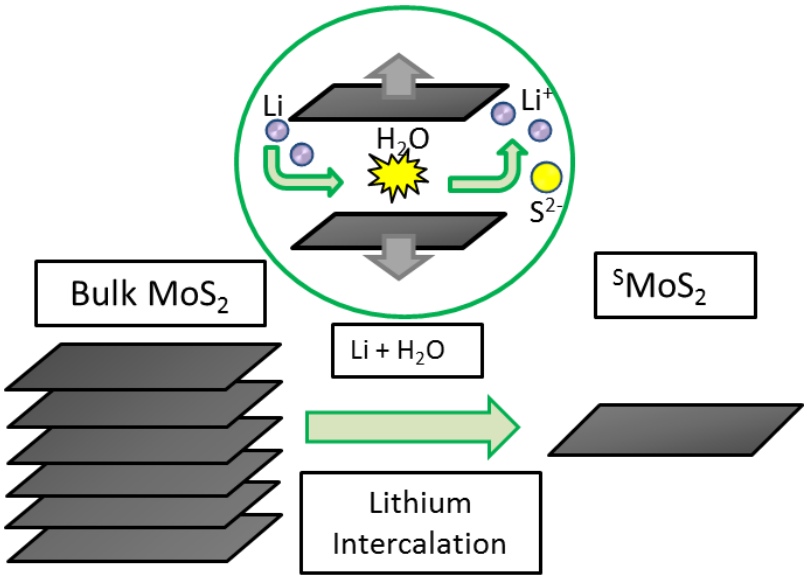


Figure 1.5 Schematic of Li intercalation reaction. Adapted with permission from Ref.[36]

1.2.2. Modifying $^{S}MoS_2$ for improved electrocatalytic reactions

An ideal catalyst for electrocatalytic reactions such as HER should possess a large amount of active sites with a fast charge transfer surface. As discussed, $^{S}MoS_2$ can exist in two different polytypes: 2H and 1T. Although 1T-$^{S}MoS_2$ has a metallic surface, it is difficult to structurally modify it due to its metastability. Semiconducting 2H-$^{S}MoS_2$ is therefore often the polytype to be modified via improving its sluggish kinetics of charge transfer at the surface and increasing the amount of active sites available. Herein, we will discuss some popular approaches to functionalise $^{S}MoS_2$ for electrocatalytic reactions.

1.2.2.1. **Engineering the Edge Sites**

There have been various attempts to increasing the electrochemically active sites for multi-layered MoS_2. For instance, thin MoS_2 nanosheets are grown vertically to expose more edge sites.[37] The same strategy can be applied to $^{S}MoS_2$ since the edge sites will always be exposed for monolayer nanosheets. Dendritic $^{S}MoS_2$ was grown on $SrTiO_3$

substrate using the low pressure CVD method to avoid uncontrollable aggregation[38] (Figure 1.6a). The branched MoS_2 has a larger edge area than that of regular nanoflakes with the same size and therefore exhibits improvement in onset potential and current density when compared to that of regular monolayer MoS_2.

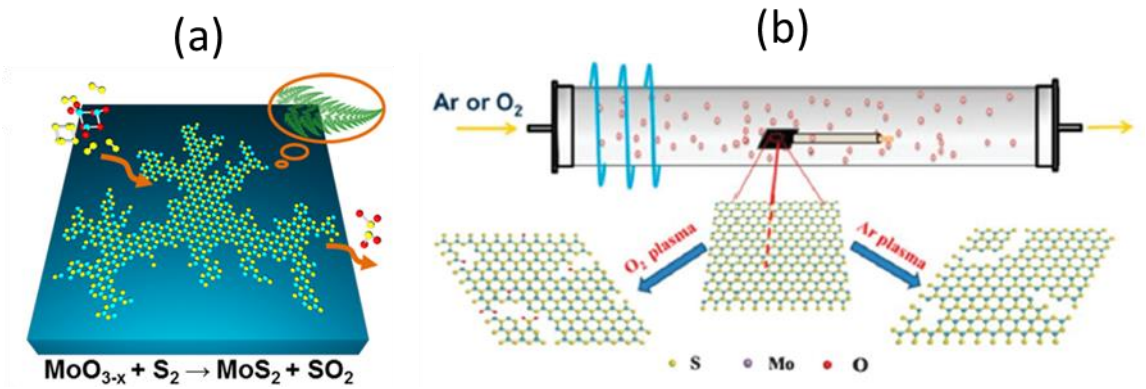


Figure 1.6 (a) The creation of dendritic $^{S}MoS_2$, Reprinted with permission from ref. [38] (b) Ar and O_2 Plasma treatment onto $^{S}MoS_2$, reprinted with permission from ref.[39]

1.2.2.2. **Creating Surface Defects**

The Mo-terminated and S-terminated edges site of unmodified 2H-MoS_2 are the predominant active sites for electrochemical reactions, while the basal surface site is catalytically inert. We have already mentioned that the generation of surface defects (S vacancy) on the basal surface of 2H-$^{S}MoS_2$ can stimulate the catalytic activity of surrounding basal sites[16] by changing their electronic properties. New valence bands are formed near the Fermi level, which allow the hydrogen atoms to be adsorbed by the exposed Mo atoms like the edge sites. Alkali metal intercalation has already been shown in the last section as a common way to prepare $^{S}MoS_2$ with S vacancies[34]. Other than chemical functionalization, surface defects can also be generated by physical methods. Mild Ar or O_2 plasma was employed to create structural defects with controllable shapes on $^{S}MoS_2$ nanosheets, which are grown onto Si substrates by CVD methods[39–41]. (Figure 1.6b) It was found that the overall charge mobility of the defected basal plane was greatly improved.

1.2.2.3. **Strain Engineering**

$^{S}MoS_2$ can withstand much higher elastic strain when compared to bulk MoS_2. Therefore, another strategy to improve the charge transfer kinetics is to introduce strain into $^{S}MoS_2$ to deform the crystal lattice. The electronic d-bands deformed by strain will be modulated accordingly by getting closer to the Fermi level. The modification of the electronic structure thus facilitates faster electron transfer in electrochemical reactions. $^{S}MoS_2$ can be grown directly on curved substrates[42] (Figure 1.7a) or nanoparticles[43] (Figure 1.7b). The external strain introduced onto the $^{S}MoS_2$ will cause a lattice distortion, which results in a localised phase transition from semiconducting 2H-MoS_2 to metallic 1T-MoS_2. This ultimately improves the surface charge transfer kinetics of $^{S}MoS_2$.

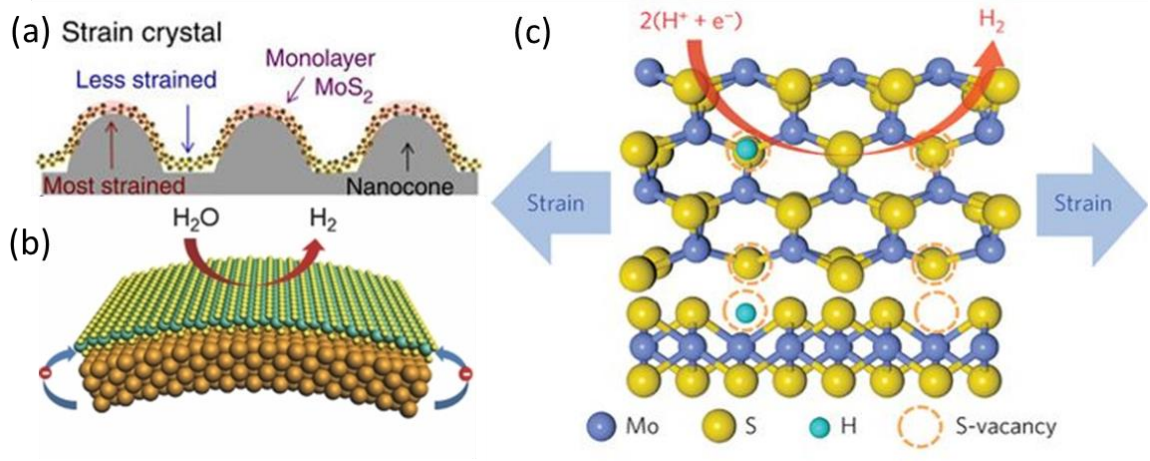


Figure 1.7 Strain Engineering (a) textured $^{S}MoS_2$ grown on a Si substrate (Reprinted with permission from ref[42]) (b) $^{S}MoS_2$ grown on a nanostructured gold. (Reprinted with permission from ref[43]) (c) Inducing mechanical strain onto $^{S}MoS_2$ with S vacancies. (Reprinted with permission from ref[24])

Zheng et al.[24] showed that capillary force induced strain can be introduced onto $^{S}MoS_2$ with basal S vacancies via ethylene glycol evaporation. Because of the tensile strain, the newly formed valence bands due to the presence of S vacancies will further shift towards the Fermi level, making the band gap narrower. The $^{S}MoS_2$ with strained basal S vacancies exhibits more efficient HER activities than its unstrained counterpart in this case.

1.2.2.4. **Doping Single Heteroatoms**

The incorporation of single heteroatoms has become the most popular approach to introduce new functionalities on 2D materials in nanoscale applications, thanks to recent advancement of synthetic techniques, analytical methods and computational simulations. The atom efficiency of the 2D materials can be maximised by downsizing nanoparticles to isolated atoms. The unique catalytic properties induced by the atomic dopants can improve the conversion efficiency in electrocatalytic reactions. It is believed that non-metal doping heteroatoms can modify the d-band electronic properties of 2D materials which enhances the charge transfer kinetic and thus facilitates faster electrochemical reactions. Single metal adatoms on the other hand can also be introduced onto different 2D materials as co-catalysts for achieving new functionalities.

We are interested to study thoroughly the effect of isolated atomic dopants on $^{S}MoS_2$ for electrocatalysis at atomic levels. Recent development of heteroatoms doped $^{S}MoS_2$ and other 2D materials such as graphene-derived monolayers for electrocatalysis will therefore be reviewed in later sections separately. Before that, the reactions of interest, electrochemical hydrogen evolution reaction (HER) and electrochemical carbon dioxide hydrogenation (CO_2RR) will be discussed in order to let the readers became familiar with the key parameters in evaluating the catalytic performance of different classes of heteroatom doped 2D electrocatalysts.

1.3. Electrochemical Hydrogen Evolution Reaction

There is an increasing demand for hydrogen to play a larger role as a renewable energy source (apart from. solar, wind and hydropower etc.) to reduce carbon emissions from various industries in the near future. Particularly, the progressive decrease in the cost of electrolysers and possible implementation of carbon taxation may justify a large scale H_2 production from electrolysis of water in centralised installations. However, noble metals are commonly used as catalysts for both anode and cathode in the electrolytic production of hydrogen from water. Their high cost is currently prohibitive in scaling up green hydrogen production. Therefore, developing inexpensive and earth-abundant catalytic materials such as $^{S}MoS_2$ for electrolytic hydrogen production reaction is of great interest. In this section, a background introduction of electrochemical hydrogen evolution reaction will be discussed. Key parameters for evaluating the HER activity of an electrocatalyst will be introduced as well.

1.3.1. Introduction to Electrochemical HER

The water-splitting reaction is the chemical reaction that breaks down water into oxygen and hydrogen.

$$H_2O \rightarrow H_2 + \frac{1}{2} O_2 \qquad \text{(Equation 1.1)}$$

It can be divided into two half equations as oxygen evolution reaction (OER) and hydrogen evolution reaction (HER). In an electrochemically driven system, the HER and OER will take place at the cathode and the anode, respectively. The equations for the reactions occurring at acidic, neutral and alkaline conditions are shown in Table 1.1.

Table 1.1 Electrochemical HER in different solutions

	Cathode (HER)	Anode (OER)
Acidic solutions	$2H^+ + 2e^- \rightarrow H_2$	$H_2O \rightarrow 2H^+ + \frac{1}{2} O_2 + 2e^-$
Neutral solutions	$2H_2O + 2e^- \rightarrow H_2 + 2OH^-$	$H_2O \rightarrow 2H^+ + \frac{1}{2} O_2 + 2e^-$
Alkaline solution	$2H_2O + 2e^- \rightarrow H_2 + 2OH^-$	$2OH^- \rightarrow H_2O + \frac{1}{2} O_2 + 2e^-$

Thermodynamically, an energy input of $\Delta G = 237.1$ kJ/mol is sufficient to drive the overall electrochemical water splitting (Equation 1.1) at standard conditions, corresponding to a potential of 1.23V. This energy input can be related to the potential (E) by the following equation:

$$\Delta G = -nFE \qquad \text{(Equation 1.2)}$$

Where n is the number of electrons per mole of products and F is the Faraday constant. However, a cell voltage of more than 1.23V is usually required in practical electrochemical systems. This is because extra energy is needed to overcome the high kinetic barriers of OER and HER at the electrode surface in rate determining steps and to

compensate for the voltage drop due to resistance in the electrochemical cell such as solution resistance.

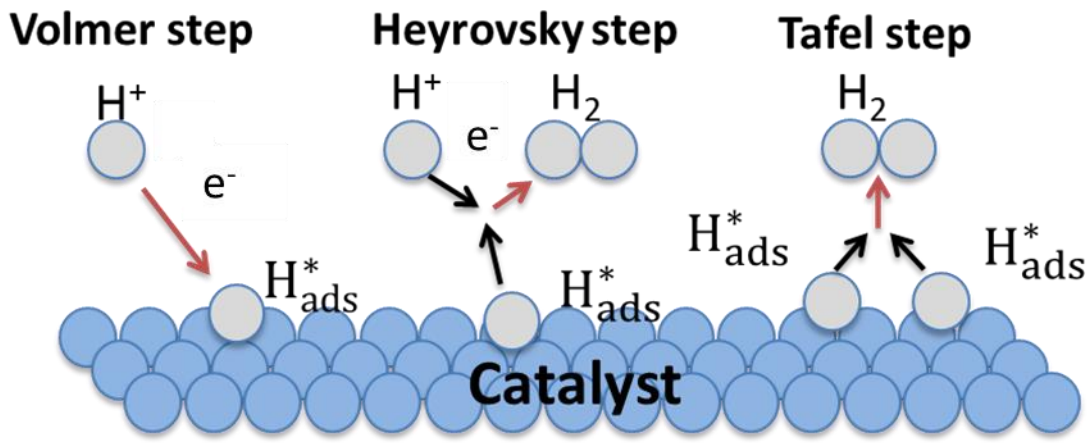


Figure 1.8 Mechanism of HER in acidic solution.

The overall voltage input can usually be reduced by lowering the resistances with a better designed electrochemical cell or choosing efficient catalysts for the half reactions at the two electrodes. Here, we would like to study how $^{S}MoS_2$ can be engineered into a better HER electrocatalyst. The mechanism of HER in an acidic environment is illustrated and described in figure 1.8. There are basically three steps involved in the overall HER. The first step is called the Volmer step which describes the generation of an adsorbed hydrogen atom (H^*_{ads}) at the catalyst surface caused by the interaction between an electron and a proton:

$$H^+ (aq) + e^- \rightarrow H^*_{ads} \qquad \text{(Equation 1.3)}$$

After the formation of H^*_{ads}, the reaction proceeds either via the Tafel step or the Heyrovsky step, which is usually dependent on the amount of H^*_{ads} available. For the Tafel step, two absorbed hydrogen atoms recombine to yield H_2 gas:

$$2H^*_{ads} \rightarrow H_2(g) \qquad \text{(Equation 1.4)}$$

Whereas for the Heyrovsky step, H^*_{ads} will interact with another electron and proton from the acidic solution to form H_2:

$$H^*_{ads} + H^+ (aq) + e^- \rightarrow H_2 (g) \qquad \text{(Equation 1.5)}$$

1.3.2. Key Parameters for HER Catalyst Evaluation

1.3.2.1. **Turnover frequency**

The intrinsic catalytic activity of a HER catalyst can be characterised by determining the catalytic turnover frequency (TOF), which describes the amount of hydrogen gas molecules produced per catalytic active site per second. While the quantity of the H_2 produced can be measured via analytical techniques such as gas chromatography, it is difficult to determine the number of active sites on electrochemical active surface area (ECSA), especially for nanoscale heterogeneous catalysts. More mechanistic and structural studies of the catalysts are usually required to understand the nature of the active sites. Therefore, TOF is usually considered to be a rough estimation rather than an accurate measurement of catalytic activity.

1.3.2.2. **Gibbs energy for hydrogen adsorption**

The Volmer step involving the surface adsorption of H atom is usually determined to be the rate determining steps in most of the catalytic HER reactions. The Gibbs free energy for hydrogen adsorption (ΔG_{H^*}) is often used as a descriptor for HER activity. Density functional theory (DFT) calculations can be applied to predict ΔG_{H^*} of the catalytic system and offer theoretical insight on the catalytic activity of the HER catalyst.[44] According to the Sabatier principle, the H adsorption process is optimal when ΔG_{H^*} is close to zero.[45] When the value of ΔG_{H^*} is too negative, the hydrogen atom will bind too strongly onto the surface, which inhibits the subsequent desorption process for the formation of H_2 gas. On the contrary, if the value of ΔG_{H^*} is too positive, the catalyst surface will not favour the adsorption process. Since H adsorption is the only determining factor for overall HER, a plot of the reaction rate of different metals (in terms of exchange current density) against their ΔG_{H^*} in HER electrocatalysis will have a volcano shape.

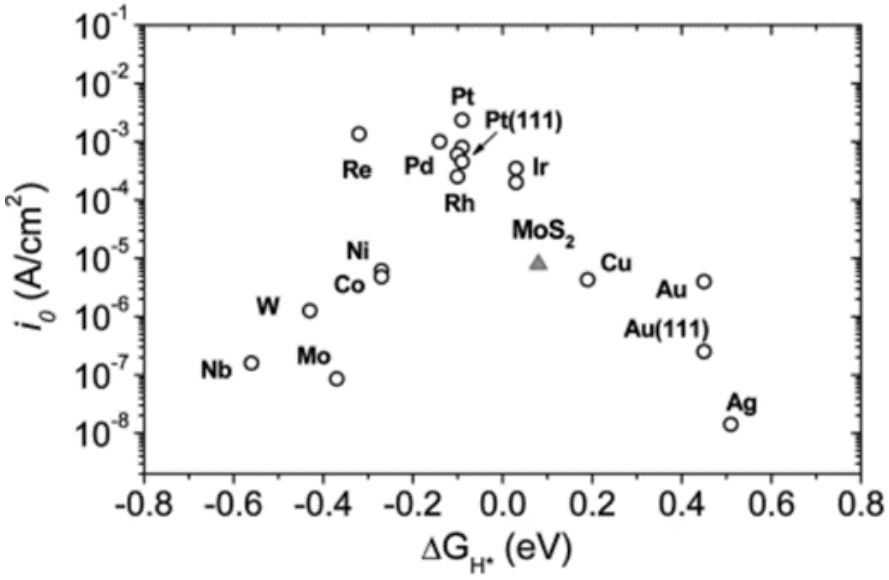


Figure 1.9 Volcano Plot for H adsorption in HER electrocatalysis. Adapted with permission from Ref.[45]

This plot is commonly known as the volcano plot or the Sabatier plot. (Figure 1.9) From the plot, it can be observed that Pt metal is at the top of the volcano curve with a ΔG_{H^*} value closed to zero which indicates that Pt is a good HER catalyst. DFT calculations were also performed on the 2H-MoS_2, which revealed that active Mo edge exhibits a ΔG_H* value of 0.08 eV at 50% adsorbed hydrogen coverage,[46] while the inert basal site only has a ΔG_H* value of 1.92 eV[47]. This verifies that the earth-abundant MoS_2 can be designed into a potential HER catalyst. It should be noted that the volcano plot is only a simple descriptor model which aims to provide insight into catalyst evaluation within the same group of catalytic materials. The reaction rate of catalysts can be affected by other additional factors such as the pH values of the electrolyte and the kinetic barriers.[48] Thus, the position of the catalyst on the volcano plot might shift either upwards or downwards compared to the literature value. More information will be required to quantitatively determine absolute reaction rates.

1.3.2.3. **Onset Potential and Overpotential**

In HER electrocatalysis, onset potential is the potential at which the reduction current for hydrogen production can be first observed. In practice, it is difficult to determine the true starting point of the reaction. The value is also heavily influenced by various factors such as the types of electrode used, the catalyst loading and the ECSA of the catalyst. Therefore, the onset potential itself is not a good indicator of the intrinsic catalytic activity. On the other hand, the overpotential (the potential between applied potential and equilibrium potential) at -10mA/cm^2 has been more commonly used as a parameter for comparing the overall performance of different classes of catalysts in HER.

1.3.2.4. **Tafel Slope**

The Tafel slope is another characteristic parameter in studying the HER activity of catalytic materials. It can be obtained via a Tafel analysis of the electrochemical voltammogram. More technical details regarding Tafel analysis will be provided in the next chapter. The Tafel equation describes the relationship between the Tafel slope, overpotential (η) and the exchange current density (J_0). For HER, the Tafel equation can be expressed as follow:

$$\log\left|\frac{J}{J_0}\right| = \frac{\beta F}{RT}\eta \qquad \text{(Equation 1.6)}$$

where J is the current density, J_0 is the exchange current density(the current flowing when the electrode reaction is at equilibrium potential). β is the transfer coefficient, R is the ideal gas constant, T is the absolute temperature, and F is the Faraday constant. From the Tafel equation, we will be able to obtain the Tafel slope for HER, $\frac{2.303RT}{\beta F}$ by plotting $\log\left|\frac{J}{J_0}\right|$ against η, with a unit of mV/decade. A small Tafel slope value and a large exchange current density indicate a fast hydrogen adsorption process on the catalyst surface.

1.4. Recent Development of Heteroatoms doped Monolayer Materials for Electrochemical HER

In this section, we focus on different classes of heteroatom doped monolayer materials as potential replacements for Pt in electrochemical HER catalysis. Due to the rapid development in this emerging area, we will only highlight recent key researches that advanced fundamental understanding for metal doped monolayer electrocatalysts.

Table 1.1 highlighted heteroatoms doped monolayer electrocatalysts for HER in 0.5M H_2SO_4 electrolyte

No.	Catalyst	Overpotential at -10mA/cm^2 (mV)	Tafel Slope (mV/decade)	TOF (s^{-1})
1	N-Graphene[49]	490	116	--
2	N,P-Graphene[49]	420	91	--
3	Mo-N-Graphene[50]	132	90	0.047 at J_0
4	Co-N-Graphene[51]	175	82	0.054 at J_0
5	Ni-Graphene[52]	~150	45	0.8 at -3V
6	Ni-defected Graphene[52]	70	--	--
7	Pt-Graphene[53]	~45	29	--
8	Ru-gC_3N_4[54]	140	57	--
9	Pt/C[53]	50	31	--
10	Se-MoS_2[55]	141	67	--
11	Se-WS_2[55]	167	107	--

1.4.1. Graphene-based materials

As the prototype of atomically monolayer materials, a vast amount of effort have recently been made to functionalise graphene for improved electrocatalytic applications. Among these graphene-based materials, N-doped graphene as a single atom catalyst has received most attention. Each nitrogen atom that substitutes carbon atom contains an extra electron which can modify the local electronic structures. The surrounding C atoms therefore become electrochemically active. However, HER performance of N-doped graphene is not comparable to that of other metal catalysts due to weak H adsorption onto the surface[49].

In view of this, there are two major approaches in improving the HER activity of N-doped graphene: (1) co-doping with other heteroatoms on a pristine graphene surface and (2) binding other isolated metal atoms onto doped N. for the co-doping approach, it was found that the P and N atoms can co-activate the surrounding C atoms in the graphene lattice, which exhibits higher HER performance than solely N-doped graphene (Table 1.1, No.1-2).[49] On the other hand, single metal atoms such as Mo[50] and Co[51] can be incorporated on the N atoms of modified graphene (Figure 1.10a), both the resulting materials show outstanding HER performance (Table 1.1, No. 4-5). Analytical results and electrochemical analyses suggested that HER active sites are associated with the metal centres coordinated to nitrogen. For Mo doped N-graphene, the calculated ΔG_{H^*} of the active sites (Mo-N-C_2) is much closer to zero when compared to that of Mo_2C, N-doped graphene, and MoN. DOS simulation of the Mo-N-C_2 site also demonstrated that embedding Mo atom onto the N-graphene can effectively improve the d-bands near the Fermi level, thus higher HER activity is resulted (Table 1.1, No.3).

Other than nitrogen, a series of studies have been conducted to chemically introduce different heteroatoms on graphene as HER electrocatalyst.[56,57] *Qiu et. al* demonstrated that single Ni atoms can substitute the C site in the graphene lattice(Figure 1.10b). [52] The resulting Ni-Graphene was shown to possess a high cycling stability, a low overpotential of 50 mV, and a small Tafel slope of 45 $mVdec^{-1}$ (Table 1.1, No. 5). Further investigation by Zhang et al. demonstrated that the HER performance can be comparable to commercial Pt/C catalyst when the Ni atoms is confined in a defective graphene[52]. (Table 1.1, No.6) There was also an attempt to replace single C atoms in the graphene lattice with Pt atoms. Thanks to the superior properties of graphene, this single atom catalyst had the mass activity of at least 37 times higher than that of commercial catalyst Pt/C[53], making it an attractive alternative in commercial applications.

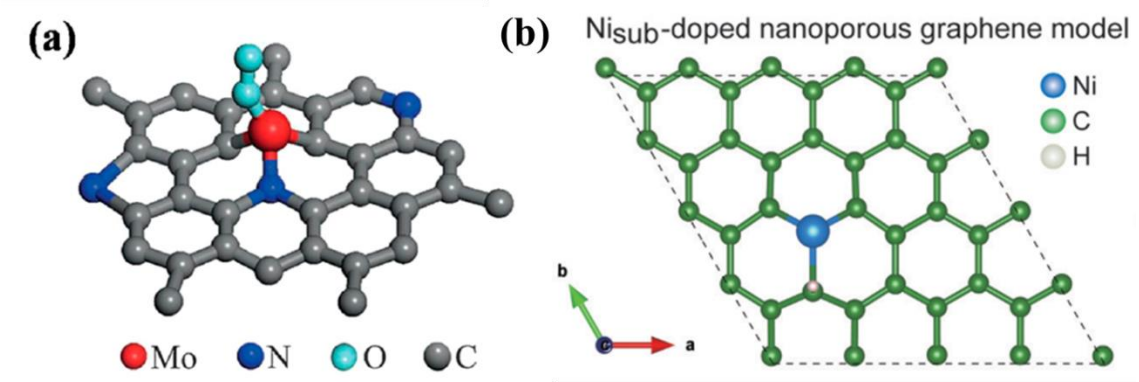


Figure 1.10 (a) Atomic structure of (a) Mo doped N-graphene (Reprinted with permission from ref[50]) and (b) Ni doped Graphene. (Reprinted with permission from ref [52])

1.4.2. Graphitic Carbon Nitride

Graphitic carbon nitride (g-C_3N_4) is another popular N-doped carbon-based catalyst. Its structure is comprised of repeated units of heptzine and poly(triazine imide). g-C_3N_4 is a semiconductor with an active basal plane, thanks to the electronegative pyridinic N in the matrix. Depending on the reaction conditions, g-C_3N_4 can have a 2D monolayer structure or 3D porous structure due to different degrees of condensation. The material is more frequently used for photocatalytic than electrocatalytic HER. Recently, Peng and co-

workers discovered that the HER activity could be significantly improved if single Ru atoms are embedded in the g-C_3N_4 matrix[54]. (Table 1.1, No. 8) DFT calculations suggested that the electronic synergism between Ru metal centres and pyridinic N can facilitate effective H adsorption, i.e. ΔG_{H^*} is closer to zero.

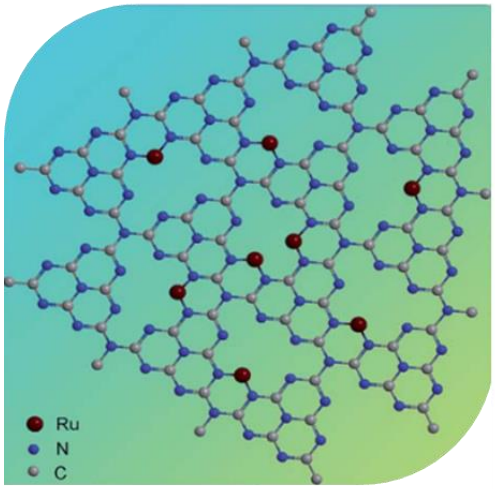


Figure 1.11 (a) Atomic structure of Ru doped g-C_3N_4.Reprinted with permission from ref[54].

1.4.3. MoS_2

Transition metal dichalcogenides are a group of layered materials that have the chemical formula of MX_2 (where M = Mo, W, V, Ta etc. and X = S, Se, or Te). MoS_2 is the most widely studied prototype in this group. As the material of interest in this thesis, we have already discussed a few important properties of $^{S}MoS_2$ in the previous sections. During the last decades, there have been many attempts to incorporate heteroatoms into two-dimensional MoS_2. However, although graphene-based monolayer materials can be synthesised by various hydrothermal or solvothermal methods, high quality monolayer MoS_2 generally can only be synthesised by CVD or atomic alkali metal intercalation as aforementioned in section 1.3. Thus, most work in this regard create single metal doped multiple-layered MoS_2 nanosheets. Pt doped multiple-layered MoS_2 synthesised by one pot synthesis exhibit improved HER performance with an overpotential of 170 mV @-10mAcm^{-2} and a Tafel slope of 96 mV/dec^{-1} when compared to pristine MoS_2[58]. DFT

calculations suggested that the Pt atoms activate the H adsorption ability of adjacent S atoms by affecting the electronic structure. However, due to the sluggish electron transfer of multiple-layered MoS_2, the HER performance is inferior to that of commercial Pt/C[53] (Table 1.1, No.9) and monolayer Pt/graphene. Nevertheless, the HER performance of single transition metal atom doped $^{S}MoS_2$ was investigated by DFT calculations. The results suggested that a volcano relationship could be observed when the Mo atoms in the 2H-MoS_2 lattice was replaced by various transition metal atoms (Figure 1.12). Pt doped MoS_2 in this case has the best HER performance among all calculated single atoms.

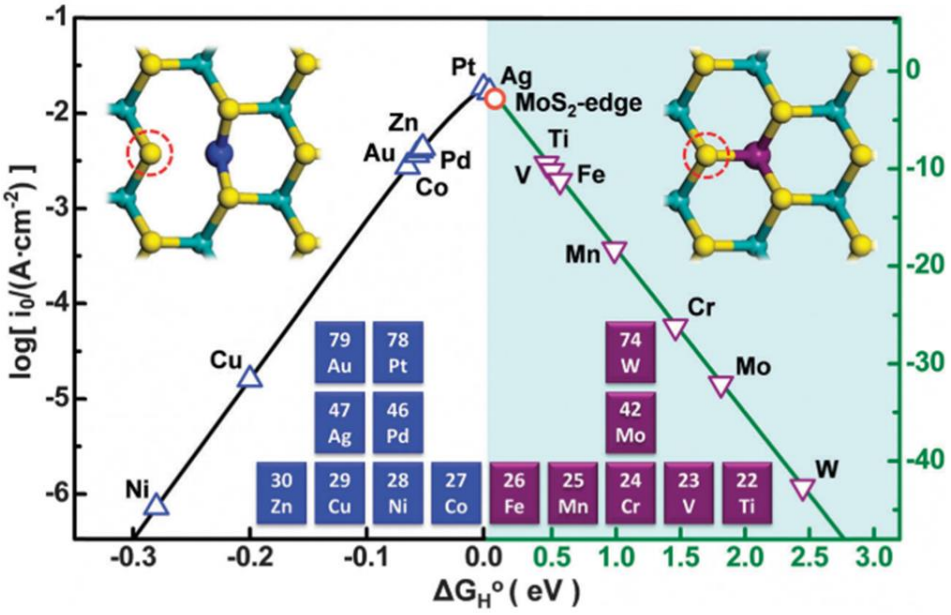


Figure 1.12 Simulated Volcano plot of transition metal doped MoS_2. Reprinted with permission from ref[58].

It should be noted that four adsorption sites at basal plane of 2H-$^{S}MoS_2$ have been identified from the DFT results[59]: (1) the hollow site at the hexagonal centre, (2) the S atop site, and (3) the bridge sites between Mo and S, and (4) the Mo atop site. (Figure 1.13) The Gibbs free energies of metal doping on these different sites should be considered during computational simulations.

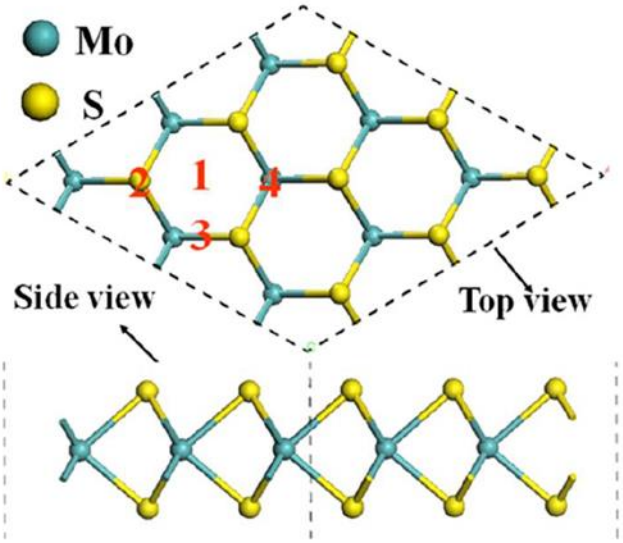


Figure 1.13 Four possible adsorption sites on $^{S}MoS_2$. : (1) the hollow site at the hexagonal centre, (2) the S atop site, and (3) the bridge sites between Mo and S, and (4) the Mo atop site. Reprinted with permission from ref[59].

For non-metal dopants, P atoms were inserted into the lattice of MoS_2 to replace Mo atoms by similar one-pot synthetic method to create P-doped multiple layered MoS_2.[60] Due to larger atomic radii of P atoms, the interlayer spacing has expanded, which facilitates faster charge transfer on the basal plane and activates H adsorption of adjacent S atoms. DOS modelling in another research work also suggests that the electronic states of $^{S}MoS_2$ are changed upon the incorporation of P atoms[61]. As a result, a much superior HER performance is resulted. From this result, it can be expected that P atoms doped on $^{S}MoS_2$ may exhibit even higher HER performance since it should not have any interlayer spacing. Unfortunately, no experimental examples have yet been reported. Apart from Mo , it is demonstrated that Se is another chalcogen atom that can substitute S atoms in the lattice of MoS_2 and WS_2 to create $MoS_{2(1-x)}Se_{2x}$ $WS_{2(1-x)}Se_{2x}$ and monolayer alloy during CVD synthesis[55]. Since Se atoms are larger than S atoms and they both cause a crystal distortion, the band gap of the MoS_2 and WS_2 will be modulated accordingly towards the Fermi level. Therefore, the conductivity of the catalyst can be tuned by changing the Se content. (Table 1.1 No. 10-11) For other group members of the doped

transitional metal dichalcogenides, there are only a handful of computational calculations reported at the moment.[62] More efforts are required to explore their electrochemical performance for catalytic applications.

In summary, graphene-based materials with heteroatoms dopants are the most studied single atom electrocatalysts recently. Due to the superior intrinsic properties of graphene itself, most of functionalised graphenes have excellent HER performance. While there are not many reports on g-C_3N_4 as electrocatalyst, it is shown that Ru dopant can enhance the over HER activity. On the other hand, direct experimental proof of high quality single transition metal atom doped monolayer MoS_2 in correlating their HER activity has not yet established. There are no clear experimental confirmation and modification of active sites at atomic levels. Most of the current works only involve replacing Mo and S atoms with the dopants of interest via bottom-up synthesis. The HER performance of other doping sites such as the Mo and S atop anchoring site has not been fully considered.

It can be concluded from this section that dopants play different roles in HER when doped on carbon-based monolayers (Graphene and g-carbon nitride) and MoS_2. With respect to carbon-based system, non-metallic dopants will activate the local C atoms while metallic dopants will act as H adsorption sites themselves. For 2H-MoS_2, all types of dopants will help trigger the electrochemical activity of S atoms at the basal plane. Nevertheless, the HER activities of most monolayer materials (except Pt-graphene) after incorporation of heteroatoms are still not comparable to the commercial Pt/C catalyst. More improvements and investigation will be still needed in this regard.

1.5. Electrocatalytic Carbon Dioxide Reduction Reactions

Although the development of renewable energies has been ongoing for a few decades, fossil fuel will likely continue to be the major source of energy in the foreseeable future. A prediction was made by energy experts that approximately 500 gigatons of anthropomorphic CO_2 will be generated due to combustion of fossil fuels.[63] In view of this, CO_2 conversion has been widely investigated to help mitigate climate change and produce more carbon feedstocks. CO_2 is basically chemically inert, which makes the CO_2 conversion process difficult. A high energy barrier of 750 kJ mol^{-1} is required due to the strong C=O bond.

Homogeneous and heterogeneous catalysts are therefore used to accelerate the sluggish kinetics of CO_2 reduction reaction. Despite having high selectivity, most homogeneous catalysts suffer from multiple critical drawbacks such as low stability and being economically unviable. More importantly, they can be easily poisoned during the CO_2 conversion and it is difficult to separate the catalysts from the reaction mixture afterwards. Major focus is therefore shifted towards the development of heterogeneous catalysts. Traditionally, noble metals such as Pt and Pd can be applied as effective heterogeneous catalyst for CO_2RR but their scarcity and high cost restrict any large-scale applications. For electrocatalytic reduction of CO_2, there are several extra challenges that needs to be addressed when developing new electrocatalysts: (1) large onset potential due to low intrinisic CO_2RR activity (2) slow electron transfer kinetics of the surface, (3) low selectivity, and (4) low durability of catalyst. Therefore, robust, cost effective and earth abundant catalysts are desired to reduce CO_2 at high rate and low applied potential.

1.5.1. Introduction to Electrochemical CO_2RR

Heterogeneous electrochemical reduction of CO_2 is a multi-electron transfer reaction that converts CO_2 into various products at the cathode-electrolyte interface. Generally, the reaction is initiated by chemical adsorption of CO_2 onto the catalyst surface. Charge transfer then occurs to break down the C-O bonds and form new C-X bonds, depending on the availability of surrounding species. After bond rearrangement, the final products will be desorbed from the cathode and diffuse back to the electrolyte.

1.5.1.1. **Electrochemical H-Cell**

H-cell is the one of most common electrochemical cells used in the laboratory for CO_2RR. It is a three-electrode system which comprises two compartments, i.e. the cathodic and anodic chambers. The two chambers are separated by an ion-exchange membrane to avoid unwanted transportation of products while keeping the two electrodes in close proximity. By connecting the cathodic chamber to a gas chromatography/mass spectrometer, the gaseous CO_2RR products generated from the cathode can be detected and analysed directly in real time.

1.5.1.2. **Electrolyte**

The type and concentration of electrolyte applied in an electrochemical cell can greatly affect the catalytic activity and selectivity. Aqueous solutions are commonly used as electrolytes in electrochemical CO_2RR since most of them are readily available and non-toxic. However, the use of aqueous solution suffers from several drawbacks. Competitive HER will reduce the overall product selectivity. CO_2 also has poor solubility in acidic or neutral aqueous solutions (~0.034 M), thus alkaline solutions containing inorganic salts such as HCO_3^-, SO_4^{2-}, or Cl^- are preferred[64]. The cations can also play a role in determining the relative concentration of charged species at the electrode-electrolyte

interface and it was found that Na^+, K^+, and Cs^+ are favourable cations for the CO_2RR reaction.[65]

Non-aqueous solvents including organic solvents and ionic liquids (ILs) can be applied for electrochemical CO_2RR to inhibit the undesirable hydrogen production and increase the solubility of CO_2. Commonly used organic solvents such as DMF, DMSO, and acetonitrile have the solubility of CO_2 4 to 20 times higher than that of water at ambient condition. These organic solvents are also found to facilitate dimerization with adsorbed CO_2 molecules to form $C_2O_4^{2-}$ intermediates which facilitates the formation of higher hydrocarbon products[65]. The yield and selectivity of product can also be tuned by controlling the ratio of water and organic solvent in the electrolyte. For ionic liquids, those with imidazolium cations such as 1-ethyl-3-methylimidazolium tetrafluoroborate (EMIM-BF4), 1-ethyl-3-methylimidazolium trifluoromethanesulfonate (EMIM-TFO) and 1-butyl-3-methylimidazolium hexafluorophosphate (BMIM-PF6), etc. are often used in CO_2RR due to their superior CO_2 solubility[66]. Other than inhibiting hydrogen production, it is generally believed that the use of ionic liquids can also facilitate the adsorption of CO_2 and formation of CO by complexation at low applied potential. However, ionic liquids are still not a preferable solvent for industrial use due to their high cost, high viscosity and low tolerance to water. To overcome these unfavourable features, ionic liquids can be dissolved in organic solvents. Further efforts will have to be made to find the optimum ratio of ILs and organic solvents for effective CO_2RR.

1.5.2. Key parameters for CO_2RR Catalyst Evaluation

Similar to electrochemical hydrogen evolution, there are several important parameters to be considered during the evaluation of the electrochemical performance of a catalyst in CO_2RR: (1) onset potential, (2) turnover frequency, (3) Tafel slope, (4) Faradic efficiency. The definition of onset potential, turnover frequency and Tafel slope has already been discussed in section 1.4 and thus will not be repeated here. While Tafel slope is a good indicator of the rate determining step (RDS) of CO_2RR, it is generally considered that the adsorption of CO_2 (formation of CO_2^-) onto the catalyst surface is the RDS. Faradaic efficiency describes the efficiency of charges transferred for facilitating the electrochemical reaction of interest. Unlike electrochemical HER, there are usually more than one product generated in CO_2RR. Faradaic efficiency (FE) is therefore used as a gauge to determine how efficient the electrochemical system is (the percentage ratio of charges transferred to the reaction pathway of interest to the total charges supplied to the system) to generate the product of interest. (Equation 1.7)

$$E_{Faradic} = \frac{\alpha n F}{Q} \qquad \text{(Equation 1.7)}$$

Where α is the number of electrons transferred, n is the number of moles for a given product (mol), F is Faraday's constant (96485 C mol^{-1}) and Q (C) is all the charge passing through during the reaction.

Table 1.2 Common C_1-C_2 products of CO_2RR in acidic and basic conditions

Number	Product	Chemical Equation	E^0_{redox}
1	Formic acid	$CO_2 + 2H^+ + 2e^- \rightarrow HCOOH$	-0.610V
2	Formate	$CO_2 + H_2O + 2e^- \rightarrow HCOO^- + OH^-$	-1.491V
3	Carbon Monoxide	$CO_2 + 2H^+ + 2e^- \rightarrow CO + H_2O$	-0.530V
4	Carbon Monoxide	$CO_2 + H_2O + 2e^- \rightarrow CO + 2OH^-$	-1.347V
5	Oxalic acid	$2CO_2 + 2H^+ + 2e^- \rightarrow H_2C_2O_4$	-0.913V
6	Oxalate	$2CO_2 + 2e^- \rightarrow C_2O_4^{2-}$	-1.003V
7	Formaldehyde	$CO_2 + 4H^+ + 4e^- \rightarrow HCHO + H_2O$	-0.480V
8	Formaldehyde	$CO_2 + 3H_2O + 4e^- \rightarrow HCHO + 4OH^-$	-1.311V
9	Carbon	$CO_2 + 4H^+ + 4e^- \rightarrow C + 2H_2O$	-0.200V
10	Carbon	$CO_2 + 2H_2O + 4e^- \rightarrow C + 4OH^-$	-1.040V
11	Methanol	$CO_2 + 6H^+ + 6e^- \rightarrow CH_3OH + H_2O$	-0.380V
12	Methanol	$CO_2 + 5H_2O + 6e^- \rightarrow CH_3OH + 6OH^-$	-1.225V
13	Methane	$CO_2 + 8H^+ + 8e^- \rightarrow CH_4 + 2H_2O$	-0.240V
14	Methane	$CO_2 + 6H_2O + 8e^- \rightarrow CH_4 + 8OH^-$	-1.072V
15	Ethylene	$2CO_2 + 12H^+ + 12e^- \rightarrow C_2H_4 + 4H_2O$	-0.349V
16	Ethylene	$2CO_2 + 8H_2O + 12e^- \rightarrow C_2H_4 + 12OH^-$	-1.177V
17	Ethanol	$2CO_2 + 12H^+ + 12e^- \rightarrow C_2H_5OH + 3H_2O$	-0.329V
18	Ethanol	$2CO_2 + 9H_2O + 12e^- \rightarrow C_2H_5OH + 12OH^-$	-1.157V
19	Ethane	$2CO_2 + 14H^+ + 14e^- \rightarrow C_2H_6 + 4H_2O$	-0.270V
20	Hydrogen	$2H^+ + 2e^- \rightarrow H_2$	-0.420V

1.5.3. The CO_2 Reduction Reaction

The direct reduction of CO_2 into CO_2^- simply involves a single electron transfer. However, it is thermodynamically unfavourable and requires a high redox potential input of ~-1.90V at standard conditions for it to occur. (Equation 1.8)

$$CO_2 + e^- \rightarrow CO_2^- \quad \text{(Equation 1.8)}$$

Proton assisted CO_2 reduction with multiple-electron transfer is more energetically favourable as it bypasses the formation of CO_2^-. Depending on the number of electrons and protons transferred, different carbon products can result. Table 1.2 lists out the common C_1 and C_2 products. The reactions with more positive redox potential are more thermodynamically favoured. However, the kinetic barrier of each reduction also needs to be considered as CO_2RR is also kinetically dependent on the amount of available protons. CO_2 and H should be readily adsorbed on active sites in closed proximity on a surface with fast charge transfer. It should be noted that the hydrogenation of adsorbed C_1 intermediate is kinetically more favourable than C-C coupling. Thus, the selectivity and rate of higher hydrocarbon products (e.g. C_2 products like ethylene, ethanol, ethane etc.) are usually lower than that of lighter C_1 products such as formic acid and methanol.

1.5.4. Possible Reaction Pathways of CO_2RR

Extensive research has been conducted into understanding the reaction mechanism of electrochemical CO_2RR computationally and experimentally. Here in this section, we will discuss the possible reaction pathways of important C_1 and C_2 products.

1.5.4.1. **Formic Acid and Formate**

To generate formic acid (HCOOH) and formate ($HCOO^-$), CO_2 is first adsorbed onto the electrode surface to create either *COOH/*OCHO (Figure 1.14a) or $*COO^-$ (Figure 1.14b) intermediates. This is then followed by proton-coupled electron transfer (PCET) to

create HCOOH or $HCOO^-$ [67]. This reaction pathway is presumed to occur on most metallic catalyst surfaces due to favourable π back-donation[68]. Other alternative routes involving the generation of $*HCOO^-$ on non-metallic tin oxide surface has also been proposed[69].

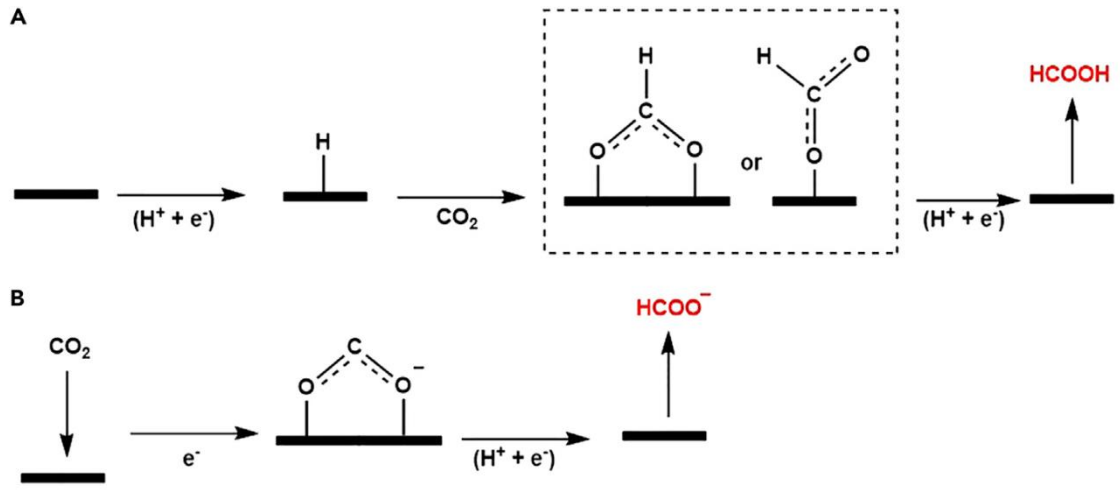


Figure 1.14 Reaction pathways of (A) Formic Acid and (B) Formate and Formation. Reprinted with permission from [70]

1.5.4.2. **Carbon Monoxide**

Another common product in electrochemical reduction of CO_2 is CO. Carboxyl *COOH intermediate is first created from a CO_2 molecule via PCET. (Figure 1.15) A second H^+/e^- pair then attacks the O atom of OH group in the intermediate to form H_2O and *CO. The absorbed carbon monoxide will then be desorbed from the surface. Depending on the pH of the reaction condition, the *COOH can also be generated by decoupled H^+ and e^- which involves the formation of $CO_2^{\cdot-}$ radicals. It is found that the formation of carboxyl *COOH intermediate and the desorption of strongly bound *CO are the rate determining steps of this reaction pathway. Catalysts that facilitate stabilisation of O in COOH while not strengthening the bonding of the C end of CO are thus desired[71].

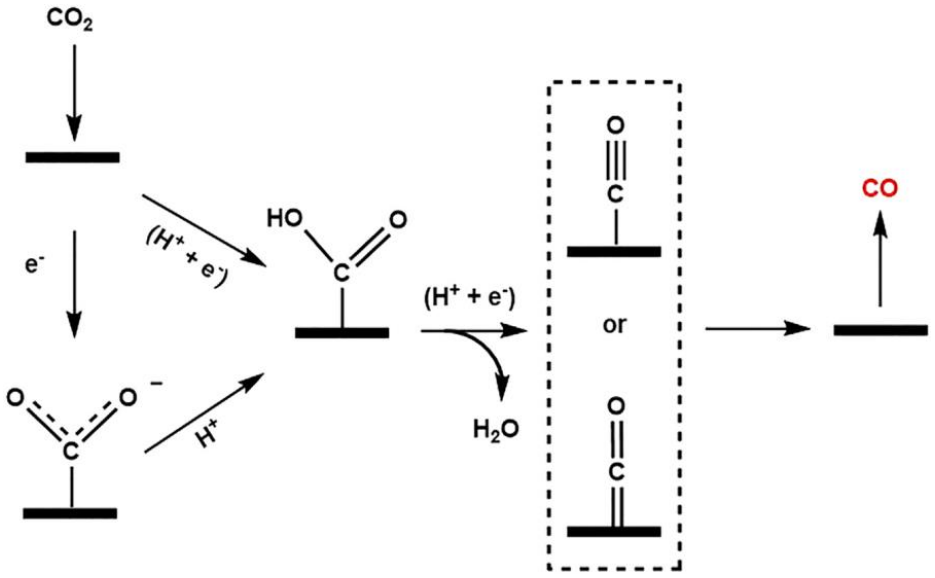


Figure 1.15 Reaction pathways of CO. Reprinted with permission from [70]

1.5.4.3. Formaldehyde, Methanol, and Methane (C_1 Products)

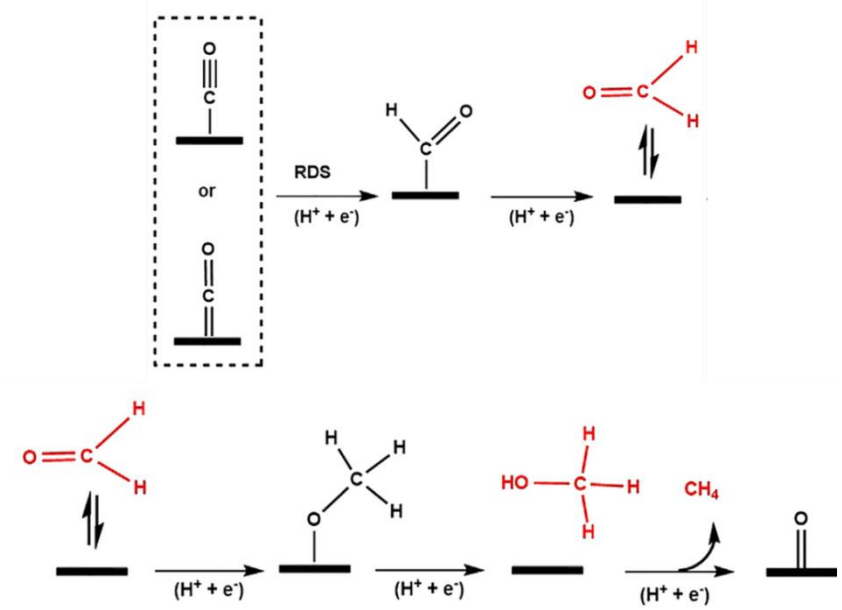


Figure 1.16 Reaction pathways of HCHO, CH_3OH, and CH_4. Adapted with permission from [70]

Adsorbed carbon monoxide (*CO) is the common intermediate for the production of C_1 formaldehyde (HCHO), methanol (CH_3OH), and CH_4 (Methane). (Figure 1.16) Computational analysis suggests that *CO can be subsequently hydrogenated into *HCO, *H_2CO, and *H_3CO intermediates via PCET[72] on Cu surface. *H_2CO can be desorbed back to the solution in the form of HCHO while *H_3CO can be reduced to yield CH_3OH.

*H_3CO can also be further hydrogenated into CH_4. However, this alternative route is kinetically unfavourable as high energy is required to dissociate the C-O in the process.[73]

1.5.4.4. **Acetaldehyde, Ethylene, and Ethanol (C_2 Products)**

Unlike C_1 product, energy intensive C-C coupling is required in producing C_2 or higher hydrocarbons. The formation of C_2 products also generally involves far more complex reaction mechanisms with many possible routes than that of C_1 products. Here, we will introduce one of the possible routes to generate acetaldehyde (CH_3CHO), ethylene (C_2H_4), and ethanol (C_2H_5OH). These three C_2 products are found to be produced under alkaline condition on Cu-based catalysts via the formation of an adsorbed carbyne intermediate[74]. (Figure 1.17) Reduction of this carbyne via PCET will produce the *CH_2 species. C_2H_4 can then be formed via C-C coupling of two *CH_2 or CO insertion. Further hydrogenation of C_2H_4 will produce CH_3CHO and C_2H_5OH.

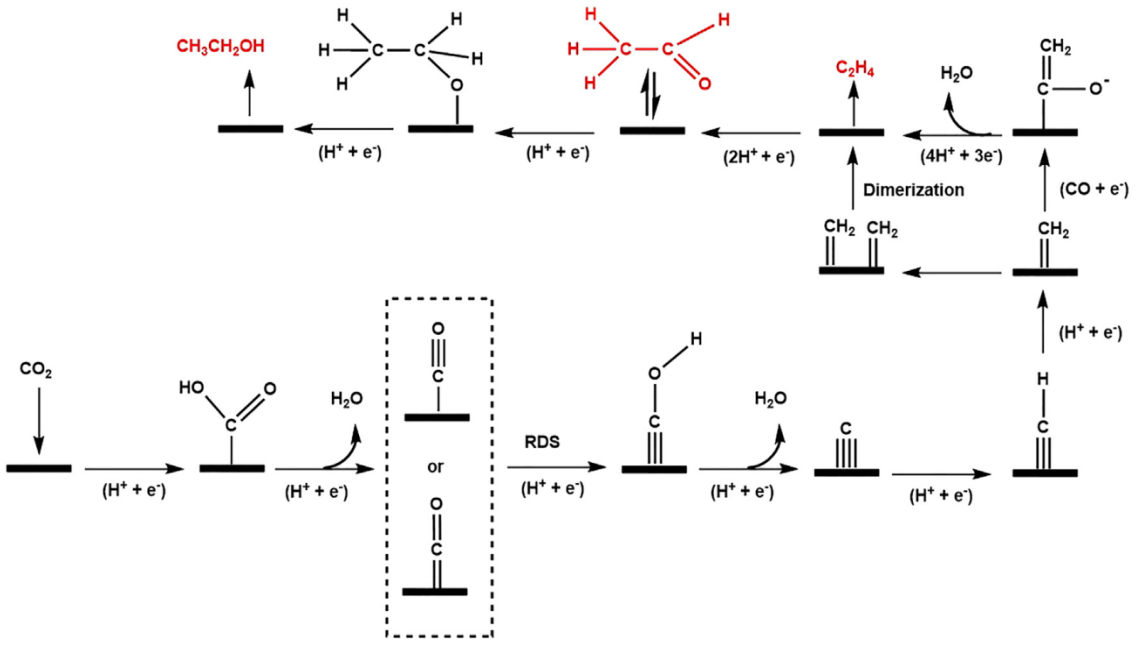


Figure 1.17 Reaction pathways of CH_3CHO, C_2H_4, and C_2H_5OH. Reprinted with permission from [70].

1.6. Recent Development of Heteroatoms doped Monolayer Materials for Electrochemical CO_2RR

Unlike HER, researches on heteroatoms doped two-dimensional materials for electrochemical CO_2RR has only started a few years ago. There are only a few experimental examples on the study of doped graphene and 2H-MoS_2 materials. Here in this subsection, we will discuss the fundamentals and challenges in designing doped 2D catalysts for CO_2RR.

Table 1.3 Summary of highlighted 2D/monolayer with heteroatoms dopants

No.	Catalyst	Onset Potential (V)	Faraday Efficiency of Major Product (FE)
1	N-doped Graphene[75]	-0.3 Vs RHE	$HCOO^-$: 73% @ -0.84 V Vs RHE
2	B-doped Graphene[76]	-1.1 Vs SCE	$HCOO^-$: 66% @1.4 V Vs SCE
3	Ni-N doped Graphene[77]	-0.61V Vs RHE	CO: 97% @-0.61 V Vs RHE
4	Nb-MoS_2 Nanosheets[78]	-0.142 Vs RHE	CO: 82% FE @ -0.8V Vs RHE
5	Se-MoS_2[79]	-0.55 Vs RHE	CO: 45.2% @ -1.15 V Vs RHE

1.6.1. Graphene Based Materials

N-doped graphene[75] and B-doped graphene[76] were found to capable of reducing the CO_2 adsorption barrier by introducing asymmetric charges to the surface. DFT calculations also reveal that the N sites and B sites are the active sites for the rate determining *COOH chemisorption. Thus, formate is the major product for the CO_2RR reaction in both cases. (Table 1.3, No.1-2) Single Ni atoms have also been embedded in N-doped graphene to form the NiN_4 unit, which helps to boost the CO_2RR activity. (Figure 1.18) The Ni-doped graphene exhibited excellent CO_2RR activity with a TOF of 14,800 h^{-1} at an overpotential of 0.61 V. The Faraday efficiency of CO also reaches 97%[77]. DFT calculations suggest that the Ni atom is the active site for the CO_2RR process. Ni atoms facilitate the adsorption of CO_2 to form the intermediate and weaken the binding of *CO for faster desorption.

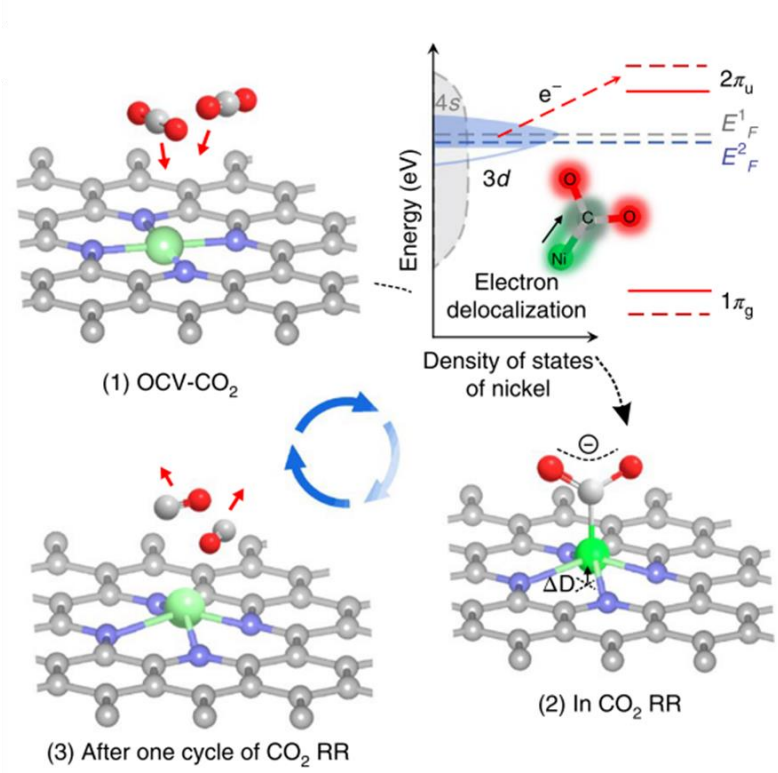


Figure 1.18 NiN4 active site on graphene for electrochemical CO_2RR. Reprinted with permission from[77].

1.6.2. MoS_2 Monolayers

There is only one example that incorporate single metal atoms onto MoS_2. Abbasi and co-workers doped single Nb atoms onto the vertically aligned ultrathin 2H-MoS_2[78]. It exhibits much higher CO_2RR activity than that of pristine multiple-layered MoS_2, with a high 82% for the FE of CO_2 at -0.8 V. DFT calculations reveal that MoS_2 itself does facilitate *CO formation. However, the rate determining step is the desorption of *CO. The introduction of Nb can alter the electronic density of surrounding edges sites which ultimately weaken the *CO binding to the active edge sites, thus a high CO FE is resulted. For non-metal dopants, Se can be introduced into the lattice of MoS_2 during CVD synthesis[79]. Due to the different atomic radii of S and Se, the Mo-S bond is shortened and the Mo-Se is lengthened. This alters the d-band electronic structure of the Mo atoms, which helps to stabilise *COOH intermediate and facilitates rate-determining *CO desorption. As a result, this Mo-S-Se monolayer alloy shows high 45.2% FE for CO formation at 1.15 V vs. RHE, which is much larger than that of MoS_2 monolayers (16.6%).

From these examples, it can be seen that dopants on graphene-based materials serve as the active sites for electrochemical CO_2RR. While for MoS_2, the Nb and Se heteroatoms will influence the electronic structure of nearby atoms or active sites, which ultimately improves the CO_2RR performance. This is in accordance with the conclusion drawn early for HER catalysts in section 1.14. More research will have to be conducted in this area to explore new possibilities to create higher hydrocarbons with high faradaic efficiency and low overpotential.

1.7. Scope of Research

In this thesis, we would like to synthesise high quality monolayer 2H-MoS_2 doped with various single transition metal atoms for electrochemical HER. The reaction mechanism and the chemical environment of the dopants will be examined thoroughly with the help of state-of-the-art analytical techniques, including synchrotronic EXAFS and HR-STEM. DFT calculations by first principle will also be conducted to support the experimental evidence. Next, we would attempt to modify metastable metallic 1T-MoS_2 monolayers with single transition metal atoms dopants. It is hoped that we will be able to study the reaction mechanism of dopants on the basal plane of 1T-MoS_2 for the first time. Last but not least, we would like to extend the scope of research by applying our single metal atoms doped 1T-MoS_2 catalyst to electrochemical CO_2RR. There are no previous studies conducted in this regard, and hopefully the project can provide insight in engineering more effectively doped MoS_2 monolayer materials for electrochemical applications.

1.8. Reference

1 W. O. Winer, *Wear*, 1967, **10**, 422–452.

2 A. N. Enyashin, L. Yadgarov, L. Houben, I. Popov, M. Weidenbach, R. Tenne, M. Bar-Sadan and G. Seifert, *J. Phys. Chem. C*, 2011, **115**, 24586–24591.

3 F. K. Perkins, A. L. Friedman, E. Cobas, P. M. Campbell, G. G. Jernigan and B. T. Jonker, *Nano Lett.*, 2013, **13**, 668–673.

4 C. Zhu, Z. Zeng, H. Li, F. Li, C. Fan and H. Zhang, *J. Am. Chem. Soc.*, 2013, **135**, 5998–6001.

5 F. M. Pesci, M. S. Sokolikova, C. Grotta, P. C. Sherrell, F. Reale, K. Sharda, N. Ni, P. Palczynski and C. Mattevi, *Acs Catal.*, 2017, **7**, 4990–4998.

6 T. Jia, A. Kolpin, C. Ma, R. C.-T. Chan, W.-M. Kwok and S. C. E. Tsang, *Chem. Commun. (Camb).*, 2014, **50**, 1185–8.

7 H. Hwang, H. Kim and J. Cho, *Nano Lett.*, 2011, **11**, 4826–4830.

8 J. Xiao, D. Choi, L. Cosimbescu, P. Koech, J. Liu and J. P. Lemmon, *Chem. Mater.*, 2010, **22**, 4522–4524.

9 R. J. Toh, Z. Sofer, J. Luxa, D. Sedmidubský and M. Pumera, *Chem. Commun.*, 2017, **53**, 3054–3057.

10 Q. H. Wang, K. Kalantar-Zadeh, A. Kis, J. N. Coleman and M. S. Strano, *Nat. Nanotechnol.*, 2012, **7**, 699–712.

11 L. Houben, A. N. Enyashin, Y. Feldman, R. Rosentsveig, D. G. Stroppa and M. Bar-Sadan, *J. Phys. Chem. C*, 2012, **116**, 24350–24357.

12 M. Acerce, D. Voiry and M. Chhowalla, *Nat. Nanotechnol.*, 2015, **10**, 313–318.

13 F. Wypych and R. Schollhorn, *J. CHEM. SOC.. C'HEM. COMMUN.*, 1992, 1386–1388.

14 W. Xu, S. Yan and W. Qiao, *RSC Adv.*, 2018, **8**, 8435–8441.

15 T. F. Jaramillo, K. P. Jørgensen, J. Bonde, J. H. Nielsen, S. Horch and I. Chorkendorff, *Science*, 2007, **317**, 100–102.

16 H. Tang and S. Roy Morrison, *Thin Solid Films*, 1993, **227**, 90–94.

17 B. Hinnemann, P. G. Moses and J. K. Nørskov, *J. Phys. Condens. Matter*, , DOI:10.1088/0953-8984/20/6/064236.

18 D. Vollath and D. V. Szabó, *Mater. Lett.*, 1998, **35**, 236–244.

19 P. A. Parilla, A. C. Dillon, B. A. Parkinson, K. M. Jones, J. Alleman, G. Riker, D. S. Ginley and M. J. Heben, *J. Phys. Chem. B*, 2004, **108**, 6197–6207.

20 I. Alexandrou, N. Sano, A. Burrows, R. R. Meyer, H. Wang, a. I. Kirkland, C. J.

Kiely and G. a. J. Amaratunga, *Nanotechnology*, 2003, **14**, 913–917.

21 X. Lu, M. I. B. Utama, J. Zhang, Y. Zhao and Q. Xiong, *Nanoscale*, 2013, **5**, 8904–8908.

22 X. Feng, Q. Tang, J. Zhou, J. Fang, P. Ding, L. Sun and L. Shi, *Cryst. Res. Technol.*, 2013, **48**, 363–368.

23 W. J. Li, E. W. Shi, J. M. Ko, Z. Z. Chen, H. Ogino and T. Fukuda, *J. Cryst. Growth*, 2003, **250**, 418–422.

24 H. Li, C. Tsai, A. L. Koh, L. Cai, A. W. Contryman, A. H. Fragapane, J. Zhao, H. S. Han, H. C. Manoharan, F. Abild-Pedersen, J. K. Nørskov and X. Zheng, *Nat. Mater.*, 2015, **15**, 48–53.

25 G. Ye, Y. Gong, J. Lin, B. Li, Y. He, S. T. Pantelides, W. Zhou, R. Vajtai and P. M. Ajayan, *Nano Lett.*, 2016, **16**, 1097–1103.

26 C. Tsai, H. Li, S. Park, J. Park, H. S. Han, J. K. Nørskov, X. Zheng and F. Abild-Pedersen, *Nat. Commun.*, 2017, **8**, 1–8.

27 G. S. Bang, K. W. Nam, J. Y. Kim, J. Shin, J. W. Choi and S. Y. Choi, *ACS Appl. Mater. Interfaces*, 2014, **6**, 7084–7089.

28 X. Ma, P. Zhang, Z. Wang, R. Wu, T. Jiang, H. Wang, Y. Zhao, S. Wu, Y. Xie, Y. Zhan and T. Nan, *Nanotechnology*, 2016, **28**, 084001.

29 T. Payam, W. Jieqiong, X. Hui, F. D. Joel, A. Mumtaz Murat, Z. Chuan, K. Kaifei, B. Brett, Z. Lijie, Z. Puqin, H. Shaoming, Y. Sen, V. B. Frank, C. John and Z. Hao, *Mater. Res. Express*, 2016, **3**, 75009.

30 Z. He and W. Que, *Appl. Mater. Today*, 2016, **3**, 23–56.

31 L. Samad, S. M. Bladow, Q. Ding, J. Zhuo, R. M. Jacobberger, M. S. Arnold and S. Jin, *ACS Nano*, 2016, **10**, 7039–7046.

32 Y. Zhan, Z. Liu, S. Najmaei, P. M. Ajayan and J. Lou, *Small*, 2012, **8**, 966–971.

33 C. A. Papageorgopoulos and W. Jaegermann, *Surf. Sci.*, 1995, **338**, 83–93.

34 Y. Wang, J. Z. Ou, S. Balendhran, A. F. Chrimes, M. Mortazavi, D. D. Yao, M. R. Field, K. Latham, V. Bansal, J. R. Friend, S. Zhuiykov, N. V. Medhekar, M. S. Strano and K. Kalantar-Zadeh, *ACS Nano*, 2013, **7**, 10083–10093.

35 X. Fan, P. Xu, D. Zhou, Y. Sun, Y. C. Li, M. A. T. Nguyen, M. Terrones and T. E. Mallouk, *Nano Lett.*, 2015, **15**, 5956–5960.

36 T. H. M. Lau, X. Lu, J. Kulhavý, S. Wu, L. Lu, T. S. Wu, R. Kato, J. S. Foord, Y. L. Soo, K. Suenaga and S. C. E. Tsang, *Chem. Sci.*, 2018, **9**, 4769–4776.

37 D. Kong, H. Wang, J. J. Cha, M. Pasta, K. J. Koski, J. Yao and Y. Cui, *Nano Lett.*,

2013, **13**, 1341–1347.

38 Y. Zhang, Q. Ji, G. F. Han, J. Ju, J. Shi, D. Ma, J. Sun, Y. Zhang, M. Li, X. Y. Lang, Y. Zhang and Z. Liu, *ACS Nano*, 2014, **8**, 8617–8624.

39 L. Tao, X. Duan, C. Wang, X. Duan and S. Wang, *Chem. Commun.*, 2015, **51**, 7470–7473.

40 H. Nan, Z. Wu, J. Jiang, A. Zafar, Y. You and Z. Ni, *J. Phys. D. Appl. Phys.*, , DOI:10.1088/1361-6463/aa5c6a.

41 M. R. Islam, N. Kang, U. Bhanu, H. P. Paudel, M. Erementchouk, L. Tetard, M. N. Leuenberger and S. I. Khondaker, *Nanoscale*, 2014, **6**, 10033–10039.

42 H. Li, A. W. Contryman, X. Qian, S. M. Ardakani, Y. Gong, X. Wang, J. M. Weisse, C. H. Lee, J. Zhao, P. M. Ajayan, J. Li, H. C. Manoharan and X. Zheng, *Nat. Commun.*, , DOI:10.1038/ncomms8381.

43 Y. Tan, P. Liu, L. Chen, W. Cong, Y. Ito, J. Han, X. Guo, Z. Tang, T. Fujita, A. Hirata and M. W. Chen, *Adv. Mater.*, 2014, **26**, 8023–8028.

44 H. Wang, C. Tsai, D. Kong, K. Chan, F. Abild-Pedersen, J. K. Nørskov and Y. Cui, *Nano Res.*, 2015, **8**, 566–575.

45 S. Trasatti, *J. Electroanal. Chem.*, 1972, **39**, 163–184.

46 B. Hinnemann, P. G. Moses, J. Bonde, K. P. Jørgensen, J. H. Nielsen, S. Horch, I. Chorkendorff and J. K. Nørskov, *J. Am. Chem. Soc.*, 2005, **127**, 5308–5309.

47 C. Tsai, K. Chan, J. K. Nørskov and F. Abild-Pedersen, *Surf. Sci.*, 2015, **640**, 133–140.

48 N. Danilovic, R. Subbaraman, D. Strmcnik, V. R. Stamenkovic and N. M. Markovic, *J. Serbian Chem. Soc.*, 2013, **78**, 2007–2015.

49 Y. Zheng, Y. Jiao, L. H. Li, T. Xing, Y. Chen, M. Jaroniec and S. Z. Qiao, *ACS Nano*, 2014, **8**, 5290–5296.

50 W. Chen, J. Pei, C. T. He, J. Wan, H. Ren, Y. Zhu, Y. Wang, J. Dong, S. Tian, W. C. Cheong, S. Lu, L. Zheng, X. Zheng, W. Yan, Z. Zhuang, C. Chen, Q. Peng, D. Wang and Y. Li, *Angew. Chemie - Int. Ed.*, 2017, **56**, 16086–16090.

51 H. Fei, J. Dong, M. J. Arellano-Jiménez, G. Ye, N. Dong Kim, E. L. G. Samuel, Z. Peng, Z. Zhu, F. Qin, J. Bao, M. J. Yacaman, P. M. Ajayan, D. Chen and J. M. Tour, *Nat. Commun.*, 2015, **6**, 8668.

52 H. J. Qiu, Y. Ito, W. Cong, Y. Tan, P. Liu, A. Hirata, T. Fujita, Z. Tang and M. Chen, *Angew. Chemie - Int. Ed.*, 2015, **54**, 14031–14035.

53 N. Cheng, S. Stambula, D. Wang, M. N. Banis, J. Liu, A. Riese, B. Xiao, R. Li, T.

K. Sham, L. M. Liu, G. A. Botton and X. Sun, *Nat. Commun.*, 2016, **7**, 1–9.

54 Y. Peng, B. Lu, L. Chen, N. Wang, J. E. Lu, Y. Ping and S. Chen, *J. Mater. Chem. A*, 2017, **5**, 18261–18269.

55 S. Hussain, K. Akbar, D. Vikraman, K. Karuppasamy, H.-S. Kim, S.-H. Chun and J. Jung, *Inorg. Chem. Front.*, 2017, **4**, 2068–2074.

56 Y. Jiao, Y. Zheng, K. Davey and S. Z. Qiao, *Nat. Energy*, , DOI:10.1038/nenergy.2016.130.

57 H. Wang, Q. Wang, Y. Cheng, K. Li, Y. Yao, Q. Zhang, C. Dong, P. Wang, U. Schwingenschlögl, W. Yang and X. X. Zhang, *Nano Lett.*, 2012, **12**, 141–144.

58 J. Deng, H. Li, J. Xiao, Y. Tu, D. Deng, H. Yang, H. Tian, J. Li, P. Ren and X. Bao, *Energy Environ. Sci.*, 2015, **8**, 20–22.

59 H. J. Chen, J. Huang, X. L. Lei, M. S. Wu, G. Liu, C. Y. Ouyang and B. Xu, *Int. J. Electrochem. Sci.*, 2013, **8**, 2196–2203.

60 P. Liu, J. Zhu, J. Zhang, P. Xi, K. Tao, D. Gao and D. Xue, *ACS Energy Lett.*, 2017, **2**, 745–752.

61 W. Shi, S. Wu and Z. Wang, *J. Nanoparticle Res.*, , DOI:10.1007/s11051-018-4379-z.

62 Y. Qu, H. Pan, C. T. Kwok and Z. Wang, *Nanoscale Res. Lett.*, 2015, **10**, 480.

63 S. J. Davis, K. Caldeira and H. D. Matthews, *Science (80-.).*, 2010, **243116**, 1330–1334.

64 Y. Hori, A. Murata and R. Takahashi, *J. Chem. Soc. Faraday Trans. 1 Phys. Chem. Condens. Phases*, 1989, **85**, 2309–2326.

65 M. R. Thorson, K. I. Siil and P. J. A. Kenis, *J. Electrochem. Soc.*, , DOI:10.1149/2.052301jes.

66 C. Cadena, J. L. Anthony, J. K. Shah, T. I. Morrow, J. F. Brennecke and E. J. Maginn, *J. Am. Chem. Soc.*, 2004, **126**, 5300–5308.

67 R. Kortlever, J. Shen, K. J. P. Schouten, F. Calle-Vallejo and M. T. M. Koper, *J. Phys. Chem. Lett.*, 2015, **6**, 4073–4082.

68 J. G. Rau, E. K. Lee and H. Kee, *Surf. Sci.*, 1987, **183**, 449–468.

69 Q. Li, Z. Wang, M. Zhang, P. Hou and P. Kang, *J. Energy Chem.*, 2017, **26**, 825–829.

70 Z. Sun, T. Ma, H. Tao, Q. Fan and B. Han, *Chem*, 2017, **3**, 560–587.

71 H. A. Hansen, J. B. Varley, A. A. Peterson and J. K. Nørskov, *J. Phys. Chem. Lett.*, 2013, **4**, 388–392.

72 A. A. Peterson, F. Abild-Pedersen, F. Studt, J. Rossmeisl and J. K. Nørskov, *Energy Environ. Sci.*, 2010, **3**, 1311–1315.

73 X. Nie, M. R. Esopi, M. J. Janik and A. Asthagiri, *Angew. Chemie - Int. Ed.*, 2013, **52**, 2459–2462.

74 H. Mistry, A. S. Varela, C. S. Bonifacio, I. Zegkinoglou, I. Sinev, Y. W. Choi, K. Kisslinger, E. A. Stach, J. C. Yang, P. Strasser and B. R. Cuenya, *Nat. Commun.*, 2016, **7**, 1–8.

75 H. Wang, Y. Chen, X. Hou, C. Ma and T. Tan, *Green Chem.*, 2016, **18**, 3250–3256.

76 N. Sreekanth, M. A. Nazrulla, T. V. Vineesh, K. Sailaja and K. L. Phani, *Chem. Commun.*, 2015, **51**, 16061–16064.

77 H. Bin Yang, S. F. Hung, S. Liu, K. Yuan, S. Miao, L. Zhang, X. Huang, H. Y. Wang, W. Cai, R. Chen, J. Gao, X. Yang, W. Chen, Y. Huang, H. M. Chen, C. M. Li, T. Zhang and B. Liu, *Nat. Energy*, 2018, **3**, 140–147.

78 P. Abbasi, M. Asadi, C. Liu, S. Sharifi-Asl, B. Sayahpour, A. Behranginia, P. Zapol, R. Shahbazian-Yassar, L. A. Curtiss and A. Salehi-Khojin, *ACS Nano*, 2017, **11**, 453–460.

79 J. Xu, X. Li, W. Liu, Y. Sun, Z. Ju, T. Yao, C. Wang, H. Ju, J. Zhu, S. Wei and Y. Xie, *Angew. Chemie - Int. Ed.*, 2017, **56**, 9121–9125.

Chapter 2

Experimental Theories and Techniques

2.1. Chapter Overview

This chapter aims to outline the analytical techniques and the experimental methods employed to conduct the research work presented in this thesis. In general, all these research works are carried out by following these four experimental procedures:

1. Synthesising the functional monolayer molybdenum disulphide (MoS_2);
2. Analysing the MoS_2 catalyst with microscopic and spectroscopic techniques;
3. Evaluating the electrochemical performance of the catalyst;
4. Supporting the experimental results with computational calculations.

Since the synthetic procedures, electrochemical system and the density functional theory (DFT) models of each project vary, some of these technical details will be included in the corresponding experimental chapters where necessary.

2.2. Microscopic Techniques

The general function of microscopes is to help examining objects that are unobservable by naked eyes. For example, a common optical microscope uses a system of magnifying lenses to produce surface images with focused visible light. In this thesis, microscopic techniques are used for determining the morphology, thickness, and the particle sizes of the nanoscale catalysts. Scanning probe microscopy and electron microscopy are used for the aforementioned purposes because they are capable of creating images of the nanoscale catalysts with much higher resolution and magnification.

2.2.1. Atomic Force Microscopy

Atomic Force Microscopy (AFM) is a type of high-resolution scanning probe microscopy. This technique involves the use of a nanoscale sharp probe to physically interact with the sample surface. The forces imposed onto the probe when scanning across the surface will be measured for three-dimensional imaging and thickness mapping[1]. The core components of an AFM include the probe, the motion controller and the laser detection system. The nanoscale sharp probe is fixed at the end of a cantilever for physically contacting the sample surface. The movement of the probe is controlled by the motion controller. A laser detector is used to calculate the force between the probe tip and the sample via measuring the deflection of the cantilever during the scan. In our experiments, NanoScope MultiMode 8 AFM model was used to evaluate the average thickness of monolayer MoS_2.

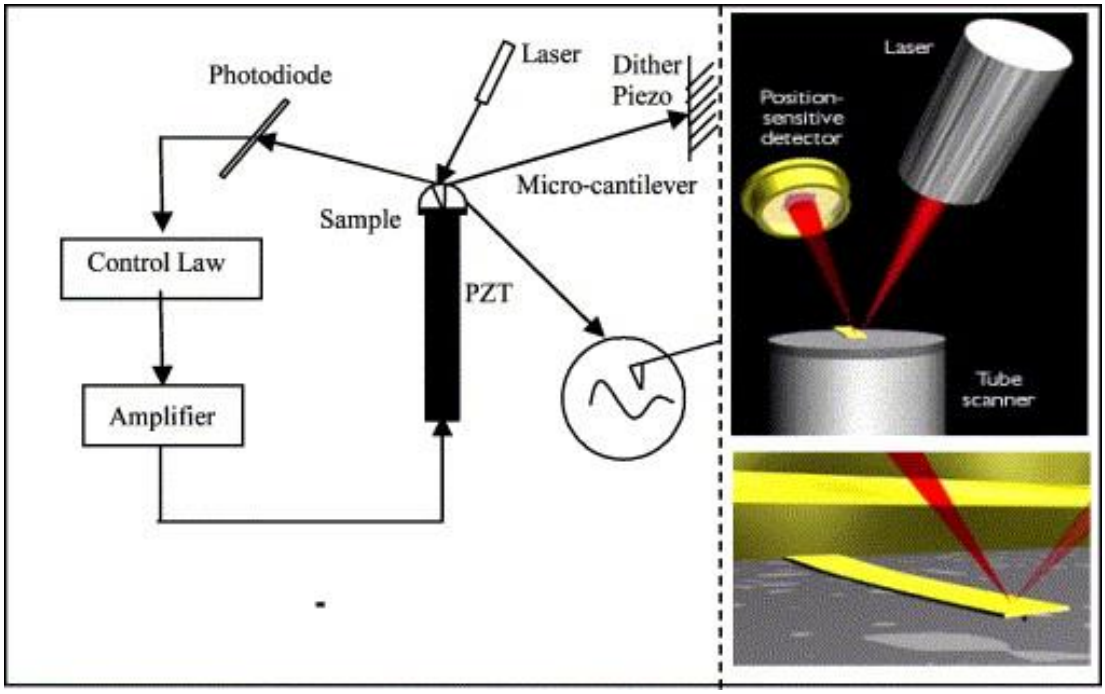


Figure 2.1 Schematic of basic AFM (left). Micro-cantilever coupled to the laser detection system (right). Reprinted with the permission from Ref[1].

2.2.2. Transmission Electronic Microscopy

Transmission Electron Microscopy (TEM) is a type of electron microscopy in which its images are created by transmitting a beam of electrons through a thin sample. The beam of electrons is first generated from a tungsten filament, LaB_6 crystal or field emission gun. It is then accelerated to a wavelength which is smaller than the interatomic spacing distance using electric and magnetic fields. TEM is usually performed under 10^{-6} mbar vacuum to avoid collision of electrons with gas molecules and ensure that the electron beam travels in a straight line. The accelerated electron beam is then aligned onto the sample surface. The electron beam interacts with the sample atoms differently based on the atomic weight. It should be noted that the sample must be thinner than 100 nm in order for the electrons to pass through. The transmitted electron beam is then refocused and projected onto a phosphorescent screen. A charge coupled device (CCD) is then used to convert the electron beam into signals for imaging. Since the resolution of TEM depends on the wavelength of the electron, it can be tuned by changing the operating voltage. Typical operating values for most TEM are around 100 to 200 keV. This will generate an electron beam with a wavelength λ from 2.5 to 3.7 pm which corresponds to a resolution of 0.3 nm.

In our experiment, TEM was used to examine the morphology of our molybdenum disulphide monolayers ($^{S}MoS_2$). TEM images were taken using a JEOL JEM-3000F FEGTEM Electron Microscope (JEOL, Tokyo, Japan) at 200kV. TEM samples were prepared by dispersing 1 mg of sample in 1 mL of ethanol by sonication. 1-2 drops of the resulting suspension were deposited on an Agar Scientific Holey carbon supported copper with 400 mesh grids, then left to dry at room temperature.

2.2.3. High-Angle Annular Dark-Field Scanning transition electron microscopy

Similar to TEM, High-Angle Annular Dark-Field Scanning transition electron microscopy (HAADF-STEM) images are obtained by transmitting a focused electron beam through the ultrathin sample. In TEM, an objective aperture is used to select the direct electron beams. The bright-field mode is used for imaging in this case. Since heavy atoms interact more strongly with the electron beam, a darker region on the image is resulted due to a larger decrease in intensity of the transmitted electron beam. In contrary, regions with no sample or lighter atoms will appear bright on the image. For HAADF-STEM, the electron beam is converged by a condenser lens and rastered across the sample by scanning coils. (Figure 2.2) The resulting electron beam is scattered. An annular detector (HAADF detector) is employed to image the scattered electrons caused by high angle scattering (>5°) (inelastic scattering) using the dark-field imaging mode. In this imaging mode, the diffracted beam appears as bright region while the directly transmitted light appears as dark region on the image. The intensity of the scattered electrons detected is proportional to the square of atomic number (Z^2). Thus, heavy atoms show a brighter contrast than lighter atoms on the image. An electron energy loss spectroscopy (EELS) detector can also be employed to detect the directly transmitted electron beam and determine the electrons loss from scattering. Due to its high dependence on Z^2, HAADF can easily identify a heavy atom in a matrix of material with lighter atoms.

In this thesis, HAADF-STEM was used to examine the catalyst structure at atomic resolution and to identify the chemical makeup of individual atomic sites. STEM was performed using a JEOL 2100F TEM with a DELTA aberration corrector operated at 60 kV and a GIF Quantum for spectroscopy. The specimen was heated to 300°C using an in-

situ high temperature sample holder to help prevent surface contamination, and was left in the microscope column overnight before data acquisition so as to ensure a stabilised signal. The ADF (Annular Dark-Field) images were acquired by using an inner acquisition semi-angle of 79 mrad and a convergence semi-angle of 35 mrad. ADF-STEM images were subjected to a 4 Gaussian smoothing filter (2px), and electron energy loss spectroscopy profiles were smoothed with a Savitsky-Golay algorithm. ADF image simulations were performed using microscope parameters corresponding to the experimental conditions (4 nm defocus, Cs 2 μm, 37 nm three-fold astigmatism, 30 nm coma, and 35 mrad half convergence angle). Low-voltage, low-current and short exposure duration were used to reduce any beam damage to the material. The high-angle scattered electrons that are captured to form the ADF image are strongly sensitive to atomic weight, allowing for Z-contrast imaging. Compositional analysis by X-ray emission detection was also conducted. For the EDX detector, Bruker 5030 SDD detector with a window area of $30mm^2$ was used. All results were then processed with Esprit 2.0 software.

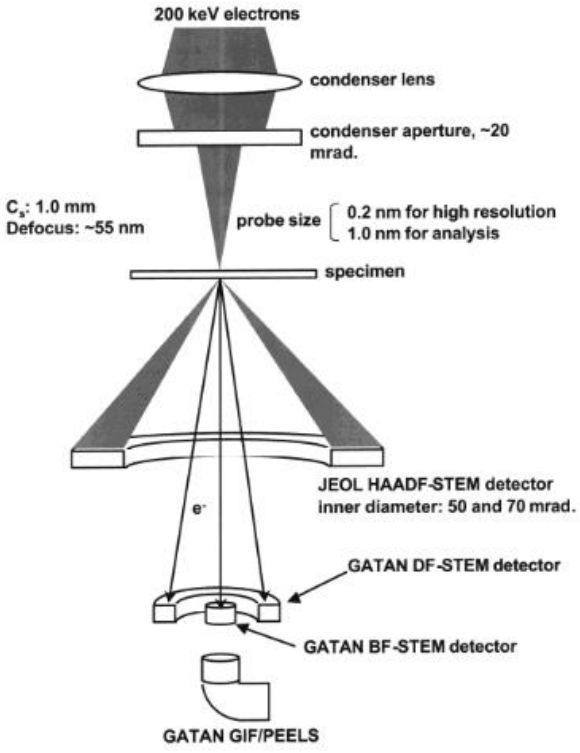


Figure 2.2 Schematic of HAADF-STEM. Reprinted with the permission from Ref[2].

2.3. Spectroscopic Techniques

Spectroscopy studies the interaction between electromagnetic radiation and the matter of interest. The changes in intensity or the frequency of the radiative energy due to this interaction are measured. In chemistry, information related to the chemical composition, crystal structure, and electronic structure of the material (atoms, molecules, crystals etc.) can be obtained via various spectroscopic techniques at the nanoscale or the microscale.

2.3.1. X-ray Photoelectron Spectroscopy

X-ray photoelectron spectroscopy (XPS) is a surface sensitive spectroscopic technique that is used to provide information of the chemical composition and oxidation state near the surface of the material. In the XPS analysis, the sample is radiated with X-ray of fixed photon energy. Ionized photoelectrons will then be emitted from atomic and molecular orbitals of the target with a kinetic energy (E_k), which can be determined by the following equation. (Equation 2.1)

$$E_b = h\upsilon - \varphi - E_k \qquad \text{(Equation 2.1)}$$

Where E_B is the binding energy of the ejected electron; h is Planck's constant; υ is the frequency of the X-ray. φ is the work function of the spectrometer; E_k is the kinetic energy of the ejected electron. The kinetic energies can be detected by the spectrometer. The characteristic E_b can be used to identify the host element and thus the elemental composition of the surface can be qualitatively and quantitively studied. Since the oxidation states can affect the core orbital energy levels which lead to slight shifts of the E_b, studying these chemical shifts provides information of the corresponding oxidation states of the target elements.

We mainly used XPS to examine the oxidation state of metal dopants on the surface of MoS_2. A Thermo Scientific K-Alpha XPS instrument equipped with a micro-focused

monochromated Al X-ray source was used for the analysis. The source was operated at 12 keV and a 400 micron spot size was used. The analyser operates at a constant analyser energy (CAE) of 200 eV for survey scans and 50 eV for detailed scans, with a dwell time of 50 ms. Charge neutralization was applied using a combined low energy/ion flood source. Thermo Scientifics Advantage software was used for data acquisition and analysis. Normalised atomic percentages were determined from the peak areas of the elemental main peaks detected on the survey scan following a background subtraction and application of Thermo sensitivity factors. All the deconvolutions were carried out using CasaXPS software.

2.3.2. X-ray Absorption Spectroscopy

X-ray absorption spectroscopy (XAS) is a spectroscopic technique for examining the local electronic structure of the sample. During the measurement, a monochromatic X-ray beam is tuned and transmitted through the sample to excite the electrons. The intensity of the transmitted X-ray beam will drop due to the excitation and the difference between the incident beam (I_0) and transmitted beam (I_t) can expressed with the following equation:

$$\mu = \frac{-ln(\frac{I_t}{I_0})}{x} \qquad \text{(Equation 2.2)}$$

Where x is the thickness of the sample and μ is the absorption coefficient. The electronic structure and the chemical environment of the sample can be found via plotting μ vs the incident energy. A typical XAS spectrum is shown in Figure 2.3. The X-ray absorption of an element will change drastically at characteristic wavelengths. This region is called the absorption edges. The edges are designated according to the principal quantum number of the absorbing atoms (n=1: K-edges; n=2: L-edges; n=3 M-edges). The measurement of this region is generally referred to as X-ray absorption near-edge structure (XANES). The XANES spectrum contains the fine structure which reveals the electronic properties,

geometry, and the oxidation state of the absorbing atoms. At higher energies, scattering occurs due to the excitation of photo-electrons from neighbouring atoms. The constructive and destructive interference between the excited and scattered electrons will produce a fine structure called extended X-ray absorption fine structure (EXAFS). EXAFS reveals the local atomic environment of the absorbing atoms, which provides information of the type and number, and distance of the neighbouring atoms.

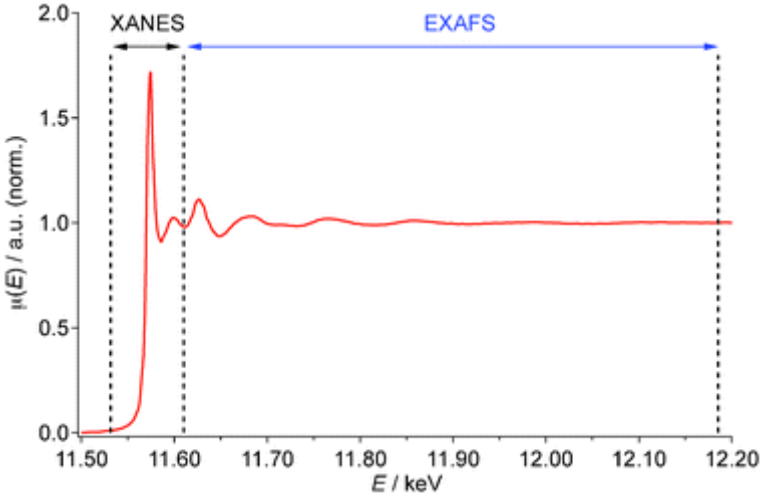


Figure 2.3 An example of a typical XAS spectrum. Reprinted with the permission from Ref[3].

Synchrotron X-ray radiation is used in our experiment to analyse the monolayer materials due to its high signal-to noise ratio. Co, Ni, Pd and Pt K-edge X-ray absorption spectrum was conducted in fluorescence mode at the BL07A XAS beamline at NSRRC, Taiwan. To examine the local chemical environment around the dopant atoms, extended x-ray absorption fine structure, EXAFS data were extracted from XAS spectra. We used the Demeter ATHENA program for XAS data analysis to perform background subtraction, normalisation and Fourier transformation. The Demeter ARTEMIS program was used to perform the least-squares curve fitting analysis of the EXAFS $\chi(k)$ data. The EXAFS Wavelet analysis was performed with the protocol developed by Harald Funke[4], where the backscatter atoms are distinguished within the same atomic shell. To confirm the

reproducibility of the experimental data, at least 2 scan sets were collected and compared for each sample. The X-ray absorption near edge, **XANE** curve for Pt doped sample was calibrated with Pt foil as reference. The amplitude reduction factor was obtained from analysis of the Pt foil, which was used as a fixed input parameter to allow refinement in the coordination number and bond distance of the absorption element. The Morlet Wavelet transform (WT) is employed in the thesis as well[4], which is an mathematical transformation method used in EXAFS analysis to obtain a two-dimensional presentation of time and frequency by resolving overlapping EXAFS paths based on the atomic numbers of the scattering atoms.

2.3.3. Electron Paramagnetic Resonance

Electron Paramagnetic Resonance (EPR) studies materials with unpaired electrons. A microwave beam was transmitted through the sample in a magnetic field. The unpaired electrons will absorb incident photons and excited from low to high energy level. The effective field (B_{eff}) experienced by the unpaired electrons is affected due to the excitation. The fundamental equation of EPR is shown as follow: Equation 2.4)

$$hv = g_e \mu_B B_{eff} \qquad \text{(Equation 2.3)}$$

where h is the Planck's constant and v is the frequency of the microwave beam, μ_B is the Bohr magneton, and g_e is the g-factor. (g_e =2.0023 for free electrons.) The change of chemical environment of the unpaired electron will give a g-factor value that is different from that of free electrons.

In this study, EPR was used as a characterization tool to evaluate the defects of MoS_2 monolayers. Continuous-wave EPR spectra were obtained by using an X-band (9.4 GHz) Bruker EMX EPR spectrometer. All measurements were carried out at 293 K. 10 mg powder of each sample was weighed and put into a glass EPR tube (0.60 i.d. and 0.84

o.d.). Then all X-Band spectra were collected over a 300 Gauss field range and 15 scans were adopted for each measurement. Signal intensity vs. electron spin numbers were calculated from the double integral of a defined peak range of the spectra.

2.3.4. Nuclear Magnetic Resonance Spectroscopy

Nuclear magnetic resonance (NMR) studies the interactions between isolated spin pairs of the target nuclei. When an external electromagnetic field is applied, an energy transfer from the base level to high energy level will take place. If the radio frequency of the oscillating magnetic field matches with the intrinsic resonant frequency (chemical shift) of the nuclei, the excited spin will return to its base level and energy with the same frequency will be emitted. This resonant frequency depends on the effective magnetic field experience by the nuclei. The effective magnetic field can be affected by electron shielding which is dependent on chemical environment. Therefore, a more electronegative nucleus will have a higher intrinsic resonant frequency. The resulting signals due to the resonation will be collected in the NMR spectrum which can be used to determine the chemical structure and dynamic information of the sample.

NMR spectroscopy can be mainly classified into two categories: liquid and solid-state NMR. Liquid NMR studies the samples dissolved in low-viscosity solvents. The main advantage of this technique is that most of the liquid NMR spectra has a high resolution. This is because there are more averaged NMR interactions due to rapid molecular movement in the solvent. As opposed to liquid NMR, broad peaks are usually resulted in solid state NMR because of slow molecular movement. Line-broadening effects can also be caused by anisotropic interactions. To counter this, a high-power radiation is usually applied to achieve saturation. A new technique called Magic Angle Spinning (MAS)

technique is employed to counter these anisotropic interactions by spinning the sample at high speeds at a certain calculated angle with respect to the applied magnetic field.

In our experiment, liquid-state ^{1}H NMR was applied to study the products of the electrochemical CO_2 reduction while solid-state NMR was used to investigate the H adsorption on the surface of MoS_2 monolayer. ^{1}H liquid state NMR samples were prepared by loading the sample into a capillary tube. DSS (4,4-dimethyl-4-silapentane-1-sulfonic acid) was used as the reference and a capillary of deuterated solvent was used for locking the spectra. The spectra were recorded using the Bruker AVIII 700 with inverse TCI 1H/13C/15N cryoprobe. ^{1}H solid state NMR samples were prepared in the argon filled glovebox by loading the powered samples into 4 mm rotors. The ^{1}H -SSNMR spectra were recorded by a Bruker Avance III HD spectrometer equipped with a 9.4 Tesla magnet at room temperature at 400 MHz. The Topspin software was used for all the data acquisition and processing.

2.3.5. Fourier-Transform Infrared Spectroscopy

Fourier transform infrared spectroscopy (FTIR) is the most common spectroscopic technique that studies the interaction of infrared radiation with the sample. When IR radiation is passed through a sample, radiation is either absorbed or transmitted. The resulting signal received by the detector generates an infrared spectrum in a graph of absorbance (or transmittance) against the wavelength (or frequency) that represents the fingerprint of the sample. Information related to the chemical structure can be revealed from the IR spectra. In this thesis, a Cary 6600 Series FTIR Spectrometer was coupled with a potentiostat to examine the adsorbed intermediate species on $^{S}MoS_2$ during CO_2 reduction. Each measurement was repeated 512 times to produce a reliable average spectrum. Resolutions Pro FTIR software was used for data processing and analysing.

2.4. Electrochemical Theories and Methods

In all of our experiments, the electrochemical activities of the MoS_2 based catalysts are determined through various electrochemical methods. This section therefore aims to explain fundamental principles of electrochemical theory and discuss the electrochemical techniques employed in the thesis.

2.4.1. Electrochemical Equilibrium

Electrochemistry is a branch of chemistry that studies the relations between electrical and chemical phenomena associated with charge transport across the interface between electrode and the electrolyte. Consider the following case of one electron transfer process between two species A and B,

$$A_{(aq)} + e^- \rightleftharpoons B_{(aq)} \qquad \text{(Equation 2.4)}$$

When the electrode is immersed into this electrolyte solution, electron transfer will take place across these two chemical phases. There will be charge separation and thus a potential difference is built up. The gradient of electrical potential will continue to grow in magnitude due to charge separation until it is balanced out by the gradient of chemical potential. At this condition, electrochemical equilibrium is achieved. Under equilibrium, the potential difference across this electrode-electrolyte interface can be characterised by the Nernst equation:

$$(\phi_M - \phi_S) = \frac{\Delta\mu^0}{F} + \frac{RT}{F} ln \frac{\alpha_A}{\alpha_B} \qquad \text{(Equation 2.5)}$$

where ϕ_M and ϕ_S is the electrical potential (V) of the electrode material and the electrolyte solution, respectively, $\Delta\mu^0$ refers to the difference between the standard chemical potentials of species A and species B ($Jmol^{-1}$), F is the Faraday constant (96485 $Cmol^{-1}$), R is the gas constant (8.314 JK-1 mol-1), T is the temperature (K) and α_A and α_B are the activities of the species A and B at the electrode interface (mol kg^{-1}).

The potential difference (ϕ_M - ϕ_S) cannot be measured here as it is an absolute value. A second electrode-electrode interface is thus required to act as the reference electrode against the electrode of interest, i.e. the working electrode[5]. The potential drop can thus be measured by the following Nernst equation.

$$E = (\phi_M - \phi_S)_{working} - (\phi_M - \phi_S)_{reference} = E^0 + \frac{RT}{F} ln \frac{\alpha_A}{\alpha_B} \quad \text{(Equation 2.6)}$$

where E^0 refers to the standard electrode potential (V). Since the activity of each species are often unknown, the activity of species *i* can be expressed with respect to their concentration by the following equation:

$$\alpha_i = \gamma_i C_i \quad \text{(Equation 2.7)}$$

where γ_i is the activity coefficients and C_i is the concentration of the species *i*. The Nernst equation can ultimately be expressed as follow:

$$E = E_f^{\ominus} + \frac{RT}{F} ln \frac{C_A}{C_B} \quad \text{(Equation 2.8)}$$

where $E_f^{\ominus}$ is the formal potential (V). This equation establishes the relationship between potential and the concentration of the species in the electrode reaction.

2.4.2. Electrode Kinetics

In most electrochemical experiments, the equilibrium is usually disrupted due to the application of a potential to the working electrode. This results in a potential difference and thus a flow of electric current around the electric circuit. Electrode kinetics is therefore studied to provide quantitative information of the electrochemical reactions. Consider a non-equilibrium single electron transfer process between species A and B:

$$A_{(aq)} + e^- \leftrightarrows B_{(aq)} \quad \text{(Equation 2.9)}$$

The Butler-Volmer equation can be used to describe the relationship between electrical current and the electrode potential.[6,7]

$$I = FAk^0 (exp\left[\frac{+\beta F}{RT}\eta\right][B_0] - exp\left[\frac{-\alpha F}{RT}\eta\right][A_0]) \quad \text{(Equation 2.10)}$$

where I is the current (A), A is the surface area (m^2), α and β are the transfer coefficients (α + β =1), η is the onset potential (V) applied to the working electrode, and [A_0] and [B_0] indicates the reaction concentration of A and B at the interface (mol cm^{-3}).

The Tafel law can be derived from the Butler-Volmer equation under extreme potential. For example, when the reductive process is much more dominant and faster than its counterpart at the electrode, the oxidative process will be negligible. The equation 2.10 will become the following:

$$I = -FAk^0 exp\left[\frac{-\alpha F}{RT}\eta\right][A_0] \qquad \text{(Equation 2.11)}$$

Taking the absolute value and then the logarithm of both sides of the equation:

$$\ln|I| = -\frac{\alpha F}{RT}\eta + constant \qquad \text{(Equation 2.12)}$$

Similar equation can be obtained when the oxidation process is the dominant one.

$$\ln|I| = \frac{\beta F}{RT}\eta + constant \qquad \text{(Equation 2.13)}$$

From the Tafel equation, we will be able to obtain the Tafel slope $-\frac{\alpha F}{RT}$ or $-\frac{\beta F}{RT}$ by plotting ln|I| against η.

In our experiments involving hydrogen evolution reaction (HER) in acidic aqueous electrolyte (Chapter 3 and 4), we use the Tafel equation to study the mechanism of the reduction reaction. We determine the rate-determining step of HER by comparing the value of the Tafel slope (which depends on value of transfer coefficient α) with other known references.

2.4.3. Modes of Mass Transport

In an electrochemical reaction, the reactant species needs to be transported from the bulk solution to the electrode surface. There are three modes of mass transport: diffusion, convection, and migration[7]. Nernst-Planck equation[5] provides a quantitative description of all these movements at point x:

$$j_i(x) = -D_i \frac{\partial C_i(x)}{\partial(\mathrm{x})} + C_i v(x) + \frac{z_i F}{RT} D_i C_i \frac{\partial \phi(x)}{\partial x} \qquad \text{(Equation 2.14)}$$

where j_i is the flux (mol cm^{-2} s^{-1}) , D_i is the diffusion coefficient (cm^2 s^{-1}), C_i is the analyte concentration (mol cm^{-3}), $v(x)$ is the velocity of the solution in the x direction (cms^{-1}), z_i is the charge of the species of interest (C). All other terms are defined previously. Electrochemical experiments can be designed to optimise the contributions from these three modes of mass transport.

2.4.3.1.Diffusion

Diffusion is the most common type of mass transport. It describes the natural movement of species from bulk solution to the electrode surface which takes place down the concentration gradient. The mass transport of diffusion can be described by Fick's law. At point x, the diffusive flux can be quantified by the Fick's first law:

$$J_{D,i} = -D_i \frac{\partial C_i(x)}{\partial(\mathrm{x})} \qquad \text{(Equation 2.15)}$$

where $J_{D,i}$ is the diffusive flux (flux/mol $cm^{-2}s^{-1}$), $\frac{\partial C_i(x)}{\partial(\mathrm{x})}$ is the concentration gradient at point x. The negative sign indicates that particles diffuse down the concentration gradient. The Fick's second law can be derived from the first law by considering the conservation of mass. It describes how the concentration of the mass changes with respect to time (t) under diffusion in one dimension:

$$\frac{\partial \mathrm{C}}{\partial \mathrm{t}} = D_i \frac{\partial^2 \mathrm{C}}{\partial x^2} \qquad \text{(Equation 2.16)}$$

In three dimensions, the equation becomes:

$$\frac{\partial \mathrm{C}}{\partial \mathrm{t}} = D_i \left(\frac{\partial^2 \mathrm{C}}{\partial x^2} + \frac{\partial^2 \mathrm{C}}{\partial y^2} + \frac{\partial^2 \mathrm{C}}{\partial z^2}\right) \quad \text{(Equation 2.17)}$$

All the electrochemical experiments in this thesis are conducted on glassy carbon macroelectrodes. The radii of the macroelectrodes are on the scale of millimetre which is much larger than the thickness of the diffusion layer. The diffusion is considered to follow a linear behaviour at the electrode surface.

2.4.3.2. Convection

Convection is caused by the movement of the solution, which can either be a natural or forced process. A natural convection process depends on the thermal gradient while mechanical stirring, bubbling, and pumping are some of the external driving forces for forced convection in electrochemical reaction. The flux caused by convection is given by the following equations:

$$j_i(x) = C_i v(x) \quad \text{(Equation 2.18)}$$

where all the terms have been defined previously. Forced convection can be controlled by using rotating disc electrode which can eliminate the unwanted effect of natural convection and at the same time boost the electrode signal by providing more fresh species to the reaction interface.

2.4.3.3. Migration

Migration describes the movement of charged species in response to an electric field. The flux due to migration can be quantified by the following equation:

$$j_i(x) = \frac{z_i F}{RT} D_i C_i \frac{\partial \phi_i(x)}{\partial x} \quad \text{(Equation 2.19)}$$

where all the terms are defined as above. In electrochemical experiments, an inert supporting electrolyte such as KCl with a much higher concentration than that of the electroactive analytes are usually added to eliminate unwanted migration.

2.4.4. Faradaic and Nonfaradaic Processes

Two types of processes take place at the electrode: faradaic and nonfaradaic processes. It is determined by whether electrons will move across the electrode-electrolyte interface or not when an external potential is applied. Further details of the two processes are discussed in this section.

2.4.4.1.Faradaic Processes

Faradaic process is defined as a charges transfer process across the solution-electrode interface which results in an electrochemical redox reaction. This process is governed by the Faraday's Law which states that chemical deposition due to the flow of current is directly proportional to the amount of electricity passed through.

$$Q = nFN \qquad \text{(Equation 2.20)}$$

where Q is total electric charge passed through the mass (C), *n* is the number of electrons involved in the process, F is the Faraday constant (96485 C mol^{-1}) and N is the mole of the mass transferred (mol).

2.4.4.2.Non Faradaic processes

A Nonfaradaic process involves as a charging process when electron transfer does not occur at the electrode-electrolyte interface when the external potential is applied. The interface will become charged due to built-up of these electrons. Ions of opposite charge will accumulate at the electrode surface due to electrostatic attraction. This results in the development of an opposite charge layers called electrical double layer (EDL). The Helmholtz double layer model, which mainly consists of the Inner Helmholtz layer (IHL) and outer Helmholtz layer (OHL), is developed to describe the charge distribution at the interface[8]. IHL is comprised of adsorbed ions at the electrode surface while OHL consists of solvated ions at the diffuse layer. The electrostatic potential drops linearly as a

functional of distance from the electrode surface to the bulk solution. The charging current due to the existence of EDL can be expressed by the following equation:

$$I = \frac{dQ}{dt} = C_d A \frac{dE}{dt} = C_d A v \qquad \text{(Equation 2.21)}$$

where C_{dl} is the double layer capacitance (Farad cm^{-2}), A is the electrode surface area (cm^2), and *v* is the scan rate (Vs^{-1}).

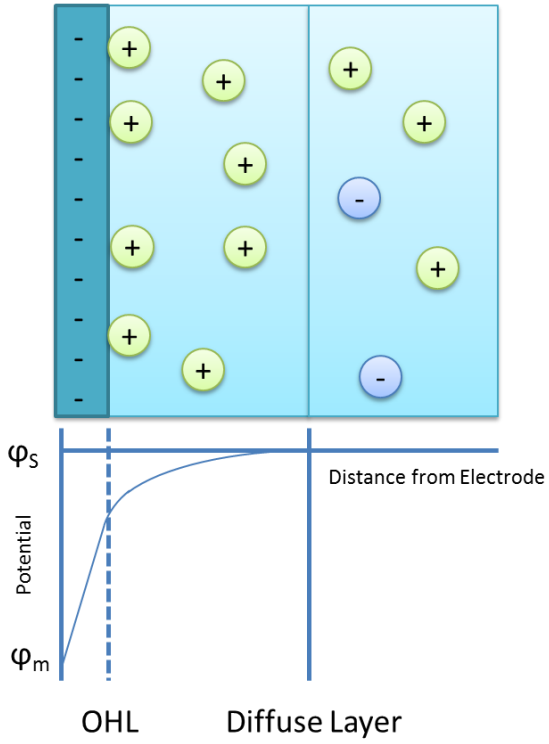


Figure 2.4 A schematic of Helmholtz double layer model.

2.4.5. Electrochemical Cell

To study the electrocatalytic reactions presented in this thesis, an electrochemical cell with three-electrode setup was used for all the experimentals. It consists of a working electrode, a counter electrode (auxiliary electrode), and the reference electrode. The reaction of interest will take place at the surface of the working electrode. The reference electrode itself has a well-defined and constant potential. This allows the potential applied to the electrochemical system to be measured and controlled, with respect to the reference potential. The counter electrode completes the electrical circuit and allows all the current

to flow through. It also prevents unwanted Faradaic processess to occur at the reaction interface of the reference electrode, which consquently affects the reference potential.

The potentiostat connected to the electrochemical cell applies a fixed potential, E, between the working electrode and the reference electrode,

$$E = (\phi_M - \phi_S)_{Working} - (\phi_M - \phi_S)_{Refernce} \quad \text{(Equation 2.22)}$$

where all units have already been defined previously. As the reference electrode has a constant value of $(\phi_M - \phi_S)_{Refernce}$, any changes in applied potential E will alter directly the $(\phi_M - \phi_S)_{Working}$ value. Such potential change will ultimately allow the device to measure the current flowing through the reaction interface between the working electrode and the solution. Further experimental details of the electrochemical cell will be included in latter chapters.

2.4.6. Electrochemical Techniques

2.4.6.1. Linear Sweep Voltammetry

Voltammetry is an electrochemical method used to measure the current (I) as a function of electrode potential (E). Quantitative and qualitative information of the analytes can be obtained from the resulting plot of I=f(E), called a voltammogram. Here in this thesis, we mainly use linear sweep voltammetry (LSV) to examine the electrochemical responses of the MoS_2 catalyst of interest in electrochemical hydrogen evolution reaction (HER) (Chapter 3). In LSV, the current at the working electrode is measured while the applied potential is scanned across a fixed range linearly with time. The LSV scan for HER begins at a positive potential where no faradaic current flows. When the potential of the working electrode reaches the vicinity of the onset potential (overpotential), the reduction of proton starts to occur. As the potential becomes more negative, the current will also grow more negative. More electrons are provided to the reaction interface for the proton reduction. The LSV scans in all experiment are chosen to stop before the generation of

gas bubbles as it will affect the current efficiency (current/mass of catalyst) of the adhering catalyst layer on the working electrode.

2.4.6.2. Chronoamperometry

Cottrell equation describes the change in electric current with respect to time in a controlled potential experiment.,

$$I(t) = \frac{nFACD^{\frac{1}{2}}}{\sqrt{\pi t}} = kt^{-\frac{1}{2}} \qquad \text{(Equation 2.23)}$$

where all units have already been defined previously. Chronoamperometry is the electrochemical technique that follows the Cottrell equations and monitors the resulting current from faradaic processes as a function of time when a potential is applied to the working electrode. The potential applied can be in the form of steps, pulses, or waves. During chronoamperometry, the only mode of mass transport will be controlled by diffusion if the solution is not constantly stirred. In this case, the diffusion layer will be built up and the surface species will be depleted over time. This will thus cause the concentration to decrease with time. In our chronoamperometry experiments, a predetermined constant potential is applied to ensure the reaction of interest takes place constantly during the selected time frame. The stability and electrochemical activity of the electrocatalysts are thus examined.

2.5. Computational Chemistry

Theoretical calculations were computed in this thesis to support the experimental evidence. The information about the structure and adsorption energy of MoS_2 based materials in electrocatalytic reactions was determined from the calculated results. This section highlights the most basic ideas and principles of computational chemistry.

2.5.1. Schrödinger Equation

Schrödinger equation is the foundation of theoretical chemistry, which describes the wave function of a molecular system. The time-independent Schrödinger equation can be expressed as follow:

$$\hat{H}\psi = E\psi \qquad \text{(Equation 2.24)}$$

Where $\hat{H}$ is the Hamiltonian operator, ψ is the molecular wave function, and E is the energy of the system. The Hamiltonian considers the following interactions in the system:

$$\hat{H} = T_e + T_n + V_{ne} + V_{ee} + V_{nn} \qquad \text{(Equation 2.25)}$$

Where T_e and T_n is the kinetic energies of electrons and nuclei respectively, V_{ne} is the attractive potentials between electrons and nuclei, V_{ee} and V_{nn} is the inter-electronic and internuclear repulsion potentials. Since the movements of relatively heavy nuclei are negligible when compared to that of electrons, the Born-Oppenheimer approximation assumes that nuclei are frozen and only the kinetics of electrons will be considered. (T_n is assumed to be zero and V_{nn} is a constant.) The Hamiltonian thus becomes:

$$\hat{H} = -\frac{1}{2}\sum_{i=1}^{N}\nabla_i^2 - \sum_{i=1}^{N}\sum_{A=1}^{M}\frac{ZA}{r_{iA}} + \sum_{i=1}^{N}\sum_{j>1}^{n}\frac{1}{r_{iA}} \qquad \text{(Equation 2.26)}$$

Where the first, second, and third term are T_e, V_{ne}, and V_{ee} respectively. The wave function now depends only on the electronic coordinates. Unfortunately, it is impossible to solve this equation for an N-body system and further assumption is required to render the problem soluble. There are two major methods to solve this problem: Hartree-Fock

theory and density functional theory. Here, we will only be describing density functional as it is the method applied for the computational simulations throughout this thesis.

2.5.2. Density Functional Theory

Density functional theory (DFT) considers the electron density as the fundamental property[8]. The Hohenberg-Kohn theorem states that the exact ground state energy of the molecular system is a functional of electron density and the fixed nuclei coordination. The energy and properties of the molecular system at ground state can therefore be determined uniquely by electron density if the position of the nuclei is known[9]. The Rayleigh-Ritz variational method states that the calculated value for the total energy of a system can only be greater than or equal to the ground-state energy. Therefore, the energy of that exact electron density function is minimalised when given the functional. Using Kohn-Sham formulation[10], a full interacting molecular system with real potential can be formulated into a non-interacting system with restricted electron movement. The total energy of the molecular system can then be expressed as the following equation:

$$E = T + E_{ne} + J + E_{xc} \qquad \text{(Equation 2.27)}$$

Where E is the total energy, T is the kinetic energy of non-interacting electrons, E_{ne} is the attraction energy between electrons and nuclei, J is the Coulomb repulsion due to interactions between electrons, and E_{xc} is the difference in kinetic energy between real and non-interacting system (XC: Exchange-correlation functional). All of the above terms except E_{xc} can be calculated. E_{xc} is the only unknown term of the equation and needs to be approximated by various functional. Two common types of DFT functional, local density approximation (LDA) and generalised gradient approximation (GGA) are developed for this purpose. LDA method only evaluates the E_{xc} by the electron density at a local coordinate while the GGA method also considers the gradient of the density at the same local coordinate.

Although DFT cannot properly simulate intermolecular interactions such as van der Waals forces and ferromagnetism etc, the latter GGA approximation method still manages to give reasonable results for molecular geometries and energies at ground state.

2.6. Reference

(1) Jalili, N.; Laxminarayana, K. A Review of Atomic Force Microscopy Imaging Systems: Application to Molecular Metrology and Biological Sciences. *Mechatronics* **2004**, *14*, 907–945.

(2) Utsunomiya, S.; Ewing, R. C. Application of High-Angle Annular Dark Field Scanning Transmission Electron Microscopy, Scanning Transmission Electron Microscopy-Energy Dispersive X-Ray Spectrometry, and Energy-Filtered Transmission Electron Microscopy to the Characterization of Nanopar. *Environ. Sci. Technol.* **2003**, *37*, 786–791.

(3) Rehr, J. J.; Kas, J. J.; Vila, F. D.; Prange, M. P.; Jorissen, K. Parameter-Free Calculations of X-Ray Spectra with FEFF9. *Phys. Chem. Chem. Phys.* **2010**, *12*, 5503–5513.

(4) Funke, H.; Scheinost, A. C.; Chukalina, M. Wavelet Analysis of Extended X-Ray Absorption Fine Structure Data. **2005**, 1–7.

(5) Bard, A. J.; Faulkner, L. R.; Leddy, J.; Zoski, C. G. *Electrochemical Methods: Fundamentals and Applications*; wiley New York, 1980; Vol. 2.

(6) Compton, R. G.; Banks, C. E. *Understanding Voltammetry*; World Scientific, 2011.

(7) Fisher, A. C. *Electrode Dynamics*; Oxford chemistry primers; Oxford University Press, 1996.

(8) Rieger, P. H. *Electrochemistry*; Schaum's Outlines; Springer Netherlands, 1993.

(9) Hohenberg, P.; Kohn, W. Inhomogeneous Electron Gas. *Phys. Rev.* **1964**, *136*, B864.

(10) Kohn, W.; Sham, L. J. Self-Consistent Equations Including Exchange and Correlation Effects. *Phys. Rev.* **1965**, *140*, A1133--A1138.

Chapter 3

Hydrothermal Deposition of Single Transition Metal Atoms on 2H Molybdenum Disulphide Monolayers for Electrochemical Hydrogen Evolution Reaction

3.1 Introduction

Predominantly, commercially available catalysts for electrochemical hydrogen evolution reaction (HER) are Pt-based materials due to their superior intrinsic activity[1,2]. Unfortunately, the scarcity and high cost of Pt has inevitably inhibited the large-scale industrial production of hydrogen through HER. In order to find more cost-effective alternatives, significant effort has been exerted to minimise the amount of noble metals contained in HER catalysts. It is hoped that the next generation of HER catalysts will consist primarily of cheaper, earth-abundant materials yet will not sacrifice the overall performance[3–5]. One such candidate material is the naturally occurring layered semiconductor, molybdenum disulphide (MoS_2).

The most stable and only naturally occurring polymorph of molybdenum disulphide is the semiconducting 2H phase (2H-MoS_2), consisting of trigonal prismatic coordinated Mo atoms[6]. With regards to hydrogen evolution reaction (HER) catalysis, it is widely accepted that the activity of 2H-MoS_2 is dominated by edge sites that are exposed to the reaction interface when the thickness of MoS_2 is reduced to nanoscale.[7,8] A commonly used descriptor for the activity of HER catalysts is the Gibbs energy of hydrogen

adsorption (ΔG_{H^*}), which suggests that optimal activity will be achieved when each step in the HER process is thermo-neutral (i.e. ΔG_{H^*} = 0 eV)[9]. Notably, 2H-MoS_2 edge sites exhibit ΔG_{H^*} of +0.08 eV[10] compared to 2.00 eV on the inert basal plane [11] and are therefore more active for HER. Thus, many different strategies have been employed to increase the ratio of active edge sites as compared to inert basal sites, with the hope of improving the overall HER activity. For instance, the general strategies are to increase the density of these active edge sites by tuning and exposing more edge planes to surface[12–15] or using nanoparticles as promoters[16] to improve conductivity and binding energy to hydrogen of the active sites.

However, the number of basal sites is far larger than edge sites, especially for a thinner slab of MoS_2. More recently, it has been shown that the 2H-MoS_2 basal plane can be activated by generating sulphur defects on the surface.[17–19] Indeed the generation of S vacancies on the 2H-MoS_2 basal plane significantly lowers ΔG_{H^*} compared with the pristine surface, from 2.00 eV to approximately 0.14 eV[20], thereby enhancing the HER activity.[21] To further enhance the exposure of basal planes, exfoliation of bulk MoS_2 is performed to decrease the stacking thickness of the planar layers by solvent exfoliation[17,18] and Li intercalation, [19,20] so that the interlayer van der Waals forces are partially or totally overcome, respectively.

Further surface functionalization at the basal plane of ultrathin 2H MoS_2 is desired to enhance electrochemical hydrogen production. In general, doping metals on a MoS_2-based nanosheet increases the HER activity[27,28]. For example, Ni nanoparticle doped on MoS_2 films was found to perform better than the pristine one[29]. However, the metal dopants are in the form of clusters or nanoparticles. While they can give excellent

electrocatalytic activity on their own, MoS_2 only serves as a supporting substrate. Recently, single atoms catalysis of MoS_2 for thermal organic conversion studied by Liu *et al.*[30] demonstrated enhanced conversion efficiency due to unique interaction between the doped metal atoms and the MoS_2 surface. The electrocatalytic performance of semiconducting 2H-MoS_2 is expected to be benefited via single metal atoms doping modification. This chapter is therefore devoted to study the structure-activity relationships of two-dimensional single transition metal (TM) atoms (Ag, Co, Ni, and Fe) doped 2H-MoS_2 (TM-$^{S}MoS_2$) for electrochemical hydrogen production with systematic experimental and modelling approaches.

Particularly, the bonding sites of isolated Co and Ni atoms on the basal planes of MoS_2 nanosheets (Co-$^{S}MoS_2$ and Ni-$^{S}MoS_2$) are directly imaged by High-Resolution Scanning Transmission Electron Microscopy with High-Angle Annular Dark-Field (HAADF-STEM) and probed by X-ray Absorption Spectroscopy (XAS). It is evident that the use of different transition metal atoms as promotors can greatly influence the electronic properties and HER catalytic activities of the metal doped MoS_2 nanosheets due to the characteristic binding affinities and geometric characteristics of the transition metals to the surface sites. Typically, it is found that Co displays a high affinity to bind on exposed surface S sites but is unable to bind on Mo sites (no Co-Mo interaction), whereas Ni can give rise to Ni-Mo interaction due to stereo-specificity in metal-metal bond formation. Density functional theory calculations were also employed for assessing the thermodynamic favourability of the doping processes. It is believed that through this investigation, more insights can be provided into elucidating the effect of single atomic dopants on 2D layered materials to enable new catalytic or electrocatalytic reactions.

3.2 Experimental Details

3.2.1. Synthesis of $^{S}MoS_2$

To exfoliate the bulk MoS_2 into nanosheets by a wet chemistry method, 0.5 g of bulk MoS_2 powder was soaked in 4 mL of 1.6 M n-butyllithium/hexane under nitrogen atmosphere for 48 hours. Solid lithiated MoS_2 (Li_xMoS_2) was then isolated by vacuum filtration, followed by washing with hexane to remove excess n-butyllithium. It was then dried under vacuum for 24 hours. The dried product was then immersed into 250 mL of water. The solution was placed into the sonication bath for 12 hours and then centrifuged at 5000 rpm for 15 minutes. Li_xMoS_2 will react with water and expand the interlayer spacing to produce the black colloid solution which contains the nanosheets (Figure 3.1). The supernatant collected was filtered using vacuum filtration, followed by washing with water. The exfoliated product was then dried in the 100^{o}C vacuum oven for storage.

3.2.2. Synthesis of TM-$^{S}MoS_2$

Four different transition-metals (Ag, Co, Ni, and Fe) were chosen for hydrothermal doping. Each of their precursor solution ($Ag(NO_3)_3$, $Co(CH_3CO_2)_2$, $Ni(CH_3CO_2)_2$ and ,$Fe(NO_3)_3$) was prepared by dissolving 0.2 mM metal ions into 1 mL of 0.5 mM thiourea solution to form a metal complex. The metal complex solution was mixed with 30mL of colloid solution, which is made by dispersing 30mg of $^{S}MoS_2$ in 30mL of Water/Isopropanol (1:1, v/v). The solution mixture was transferred into an autoclave and then placed into the oven at 160^{o}C for 24 hours for the hydrothermal reaction to occur. (Figure 3.2) Afterwards, the precipitate was washed with deionized water and dried under vacuum for 12 hours to obtain the solid product.

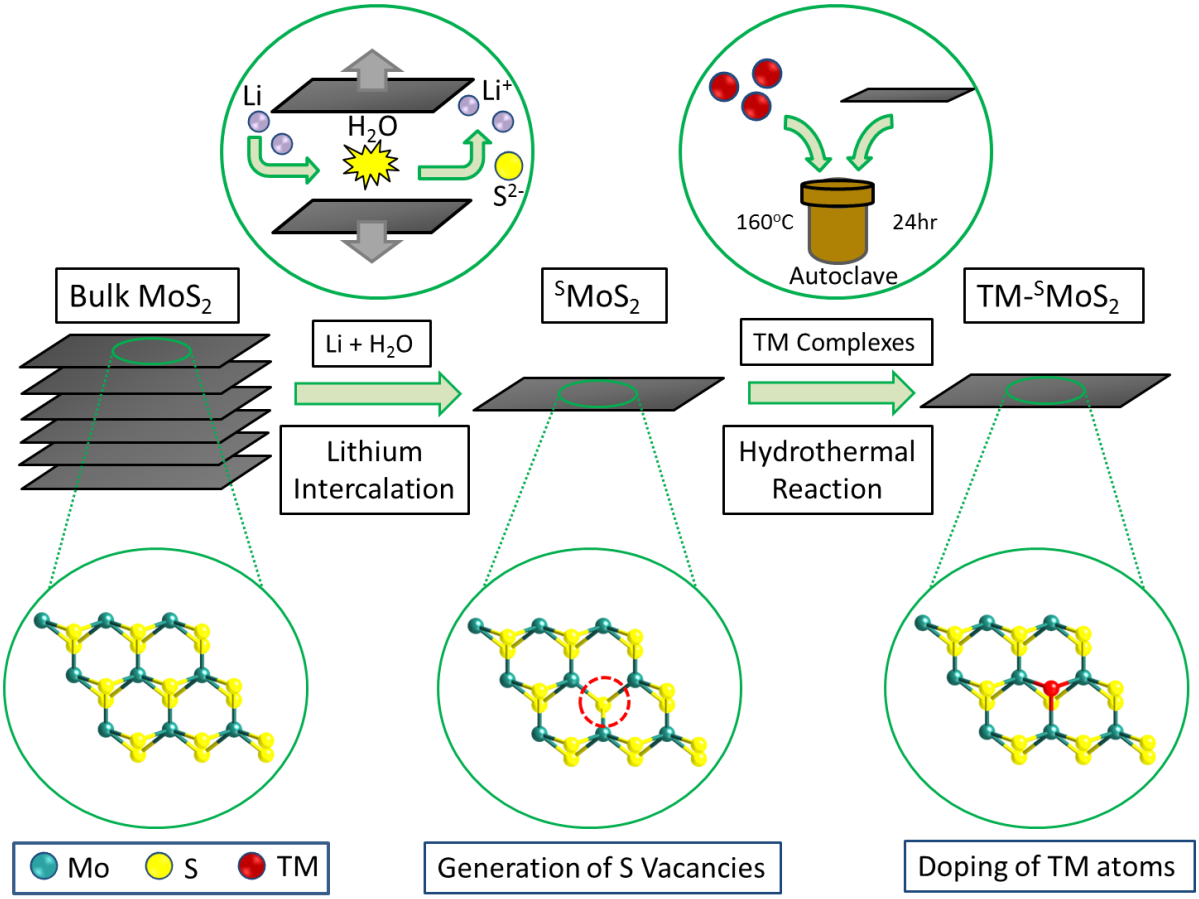


Figure 3.1 Schematic procedures of $^{S}MoS_2$ and TM-$^{S}MoS_2$ synthesis. The structures of MoS_2 on this figure has been simplified for the purpose of conveying important information to the reader. There are possible structural transformations during the synthetic process and isolated transition metal atoms can be doped on other possible positions. These will be further elucidated in later sections.

3.2.3. Electrochemical Cell

A three-electrode system controlled by μ-AUTOLAB III potentiostat (Eco-Chemie, Netherlands) was applied to carry out all electrochemical measurements. A platinum coil counter electrode and an Ag|AgCl (1molL^{-1}KCl) reference electrode were used. To prepare the working electrode, 4 mg of the MoS_2-based catalyst and 80 μL of 5 wt% Nafion®117 solution will be dispersed in 1 ml of water/ethanol (4:1 v/v) and then followed by 30 min sonication to create a homogeneous ink. The ink was then drop-coated onto the surface of a glassy carbon electrode with a surface diameter of 3 mm. All measurements were calibrated with respect to the reversible hydrogen electrode (RHE).

Several precautions for minimising the IR drop effect were taken. The electrolyte (0.5M H_2SO_4) was used as it provided sufficient ions to keep the solution resistance low and the glassy carbon working microelectrode was fairly conductive and small in surface area. While it was difficult to obtain perfect cell geometry, a standard three-electrode electrochemical cell was used to keep the distance between three electrodes fixed. The IR compensation circuit fitted with a digital-to-analog converter was connected to the potentiostat, which helped the partially compensation for the IR drop during the electrochemical scans. It should be noted that the thickness of the deposited catalyst film may affect the overall HER activity as amount of nanosheets available at the surface can vary. Serious restacking of nanosheets is also possible when such catalyst film is too thick. Repeated electrochemical testing was conducted to minimise the uncertainty of the result.

3.2.4. Density Functional Theory

Electronic structure calculations and geometrical optimizations were performed using density-functional theory as implemented in Vienna ab initio simulation packages (VASP) [31] , the exchange-correlation energy was calculated using Perdew-Burke-Ernzerhof (PBE) functional[32] , and the ion-electron interaction was treated using the projector-augmented wave (PAW) method[33], the cutoff of plane wave basis was set to 400 eV for solving the Kohn-Sham equations[34]. A (3×3) supercell of 2H-MoS_2 was selected to simulate the monolayer molybdenum disulfide ($^{S}MoS_2$) basal plane, periodic boundary conditions were used and 15Å of vacuum in the *z*-direction was used to separate neighbouring MoS_2 basal planes. The Brillouin zone has been sampled using an 2×2×1 and a 8×8×4 Monkhorst-Pack[35] grid of k-points for geometry optimizations and density of states (DOS) calculations, respectively. Both lattice constants and atomic positions were relaxed until the forces on atoms were less than 0.02eV $Å^{-1}$ and the total energy change was less than 1.0×10^{5} eV.

3.3 Structural Analyses of $^{S}MoS_2$ and TM-$^{S}MoS_2$

3.3.1. Morphology of $^{S}MoS_2$

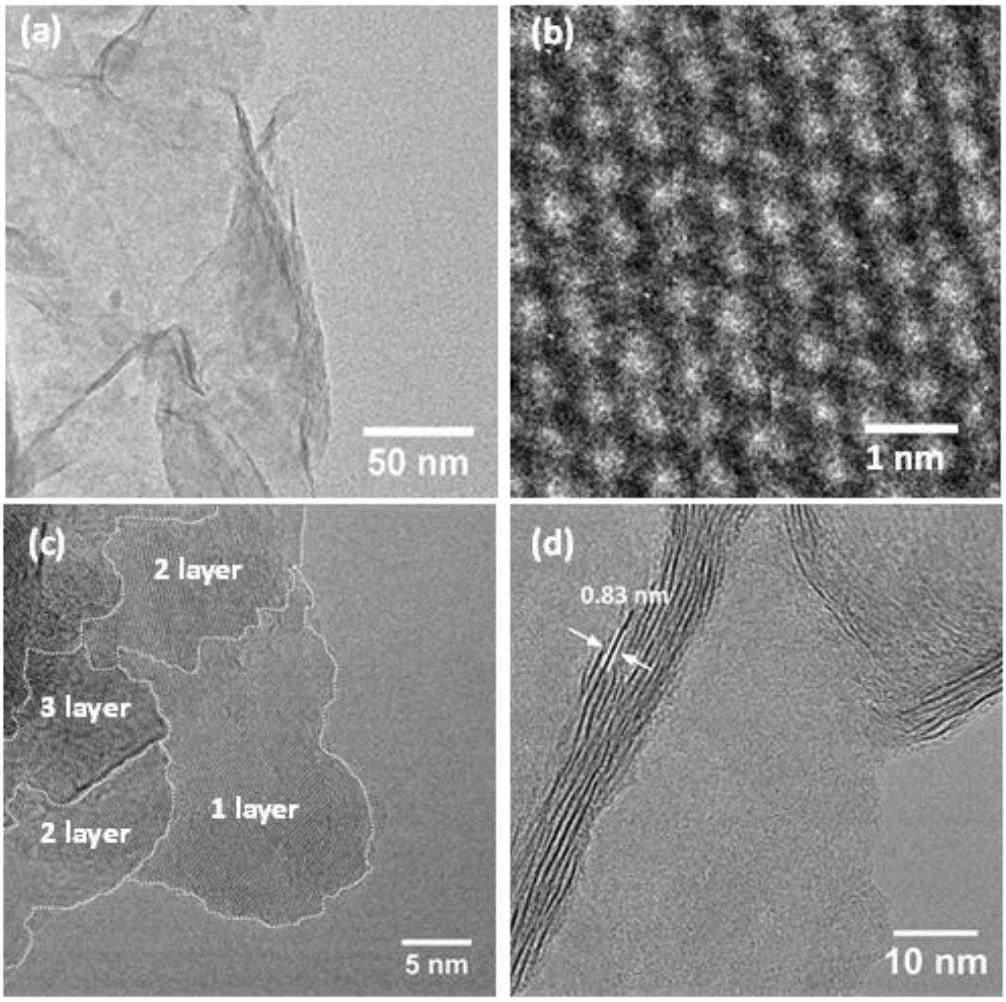


Figure 3.2 HRTEM of $^{S}MoS_2$. (a**)** Sheet-like morphology exfoliated $^{S}MoS_2$. (b) Honeycomb structure of the 2H-MoS_2. (c)Top view and (d) side view of restacked $^{S}MoS_2$.

Before evaluating the electrocatalytic performance of the synthesised $^{S}MoS_2$-based nanosheets, a wide set of experimental analyses had been conducted to verify their quality. High Resolution Transmission Electron Microscopy (HRTEM) was used to examine the morphology of exfoliated $^{S}MoS_2$. It is clearly shown from figure 3.2a that unlike the bulk crystalline MoS_2, the exfoliated $^{S}MoS_2$ has a sheet-like morphology. This confirms that the lithium intercalation method can indeed help exfoliate the bulk precusor into

nanosheets as intended. Figure 3.2b shows the signature honeycomb hexagonal structure of 2H-MoS_2. As expected, not all the nanosheets shown in the TEM images are monolayers. Since all TEM samples are prepared by dropcasting dispersed $^{S}MoS_2$ solution onto TEM copper grids, quick evaporation will hasten the aggregation process. However, it is also possible that the nanosheets are either not completely exfoliated during the synthesis or restacked to each other over time. (Figure 3.2 c and d)

3.3.2. Thickness Determination of Exfoliated $^{S}MoS_2$

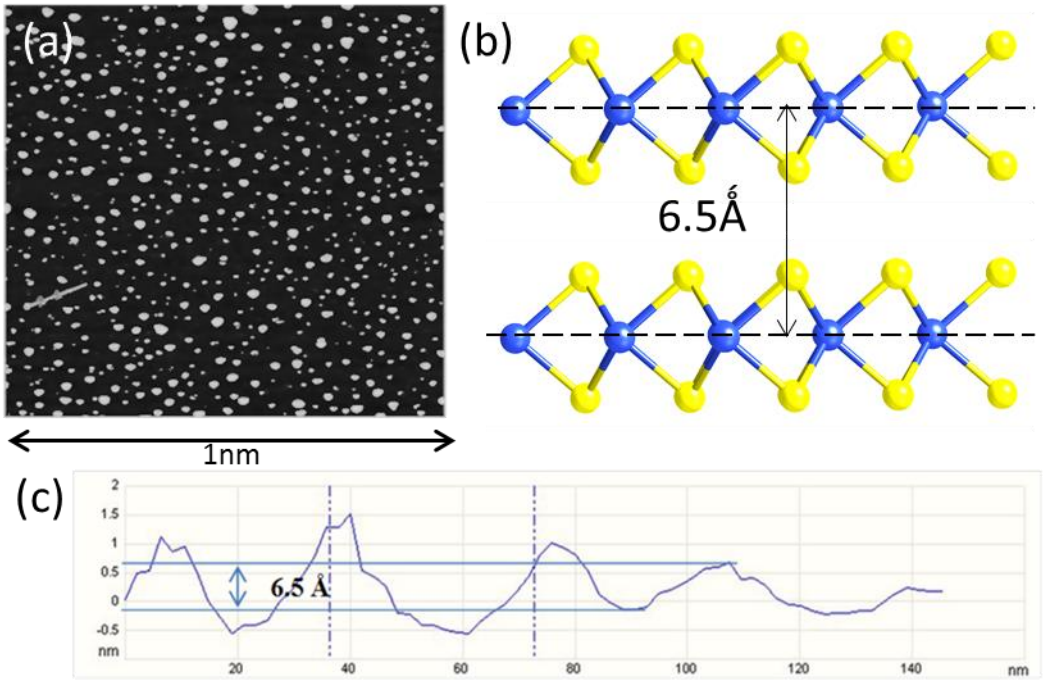


Figure 3.3 AFM image analyses of exfoliated $^{S}MoS_2$. (a) AFM image of spin-coated $^{S}MoS_2$ (b) a model of 2H-MoS_2 (c) step heights of individual MoS_2 layers

Atomic force microscopy was performed to examine the general thickness of exfoliated $^{S}MoS_2$ nanosheets. $^{S}MoS_2$ nanosheets are spin-coated onto the surface of Si/SiO_2 substrate. (Figure 3.3a) The lateral dimension of the $^{S}MoS_2$ flakes are around 20 to 40 nm and the step heights of individual layers are between 0.6 and 0.7 nm. The average step height matches with the structural distance of the S-Mo-S triatomic building block. (Figure 3.3b and c). Statistical analysis of 100 flakes produced by the lithium exfoliation

method revealed that 56% of the flakes are monolayer, 28% are bilayers, and 13% are trilayers. Only 3% of the flakes are more than three layers. Since the majority of MoS_2 flakes are still monolayers even after possible restacking, this proves that MoS_2 nanosheets synthesised by the lithium intercalation method will still be regarded as $^{S}MoS_2$ for the rest of this thesis.

3.3.3. Sulphur Defects on $^{S}MoS_2$

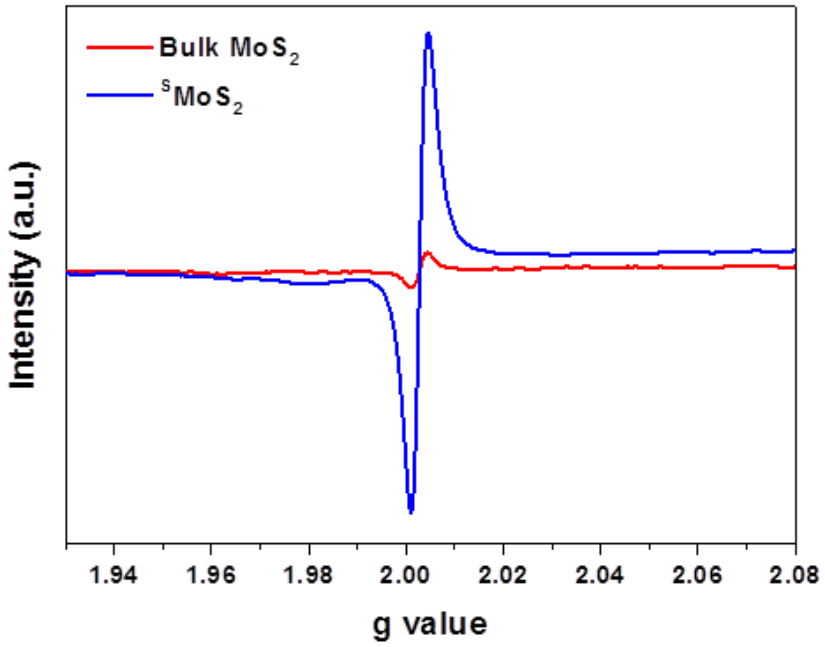


Figure 3.4 EPR spectra of Bulk MoS2 and exfoliated $^{S}MoS_2$. The Sulphur Defect (Arbitrary unit, 10^{14} counts/g): Bulk MoS_2: 1.31 (0.1%), ^{S}MoS2: 1340 (100%). (g = 2.05)

The sulphur defect sites have been proven by previous researches to help activate the basal plane of MoS_2. Electron paramagnetic resonance (EPR) was employed for this purpose to detect the exposed paramagnetic molybdenum species at the defect sites. The EPR spectra in Figure 3.4 shows a peak at around g=2.05 due to trapped unpaired electron by O_2 at sulphur vacancy (VS) sites. The arbitrary amount of sulphur defects ($1340x10^{14}$counts/g) on exfoliated $^{S}MoS_2$ is at least around 1000 times higher than that of

bulk crystalline MoS_2 (1.31x 10^{14} counts/g), which suggests that sulphur defects are readily created from the basal site upon the lithium exfoliation process.

3.3.4. Doping Concentration of Transition Metals

Inductively coupled plasma mass spectrometry (ICP-MS) was employed to analyse the concentration of transition metal on the $^{S}MoS_2$ surface (Table 3.1). A typical result shows that around 3.0 wt% of Co metal content (mg/mg) and a corresponding calculated [Co/Mo] ratio of 11 can thus be deduced for Co-$^{S}MoS_2$. Thus, hydrothermal doping process using transition metal precursors is proved to be successful to immobilize metal dopants onto the $^{S}MoS_2$ surface. Further in-depth analysis will be provided in later sections to examine whether the doped transition metals are in the desired form of isolated atoms or simply nanoparticles.

Table 3.1 Inductive coupled plasma mass spectrometry (ICP-MS) of 5.043mg Co-$^{S}MoS_2$

Mo				Co			
Wavelength (nm)	Intensity	Concentration[b] （mg/L）	Content[c] (mg/mg)	Wavelength (nm)	Intensity	Concentration （mg/L）	Content (mg/mg)
202.03	1176703	51.75	0.256543724	228.615	466868	5.69	0.028207416
277.54	1884379	52.41	0.259815586	236.379	393049	5.89	0.02919889
202.03	1196678	52.63	0.260906207	228.615	473938	5.77	0.033408208
277.54	1921969	53.46	0.265020821	236.379	397359	5.95	0.029496332

3.4 Electrochemical Testing for Hydrogen Production

3.4.1. Linear Sweep Voltammetry

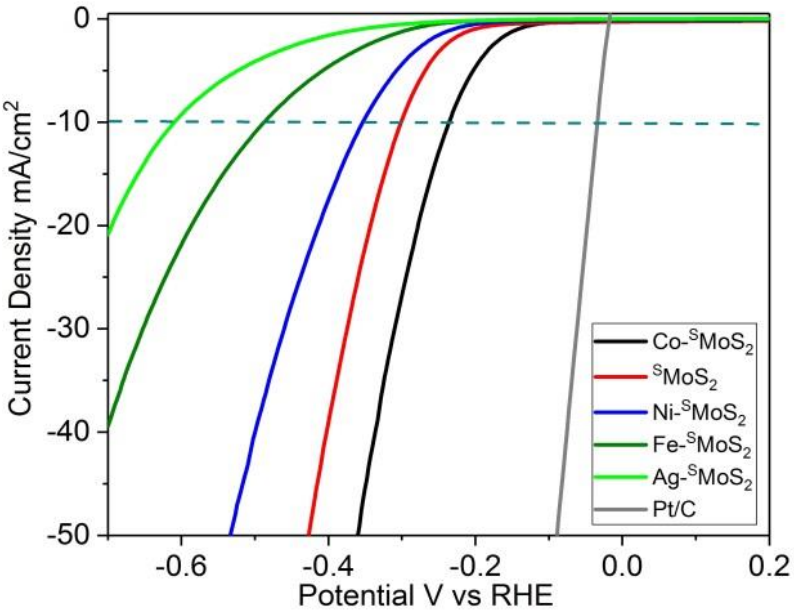


Figure 3.5 HER activity of TM-$^{S}MoS_2$ measured by LSV. TM-$^{S}MoS_2$ nanosheets and the reference 20% Pt/C were scanned in 0.5M H_2SO_4 at a scan rate of 2 mVs^{-1}.

The electrochemical HER activities of the TM-$^{S}MoS_2$ nanosheets measured with pre-calibration and IR-correction are shown in Figure 3.5. From the linear sweep voltammogram (LSV), $^{S}MoS_2$ nanosheets exhibits a distinctive HER catalytic activity when decorated with different single metal atoms. Among the tested samples, Co-$^{S}MoS_2$ appears to significantly promote the activity of $^{S}MoS_2$ nanosheets with the lowest onset potential of 220 mV at 10mA/cm^2. Interestingly, other transition metal doped nanosheets follow the order of Ag < Fe < Ni, which show worse onset potential than the pristine $^{S}MoS_2$ (300mV at 10mA/cm^2). Typically, Ni-$^{S}MoS_2$ shows the onset potential of 353mV at 10mA/cm^2. The data clearly suggest that the choice of the transition metal dopant greatly influences the HER catalytic performance of the basal $^{S}MoS_2$ materials. It has been attributed that the effect of metal dopant is to modify the H adsorption enthalpy of surface edge S sites and Mo sites in HER.[28] It would be interesting to see whether the

basal sites can be modified by the metal dopants and their effects on the HER. In addition, Ni and Co are the two neighbour transition metal elements in the periodic table. One would expect their electronic effects should be very similar to each other.[38,39] Clearly, our HER measurements cannot be simply accounted by volcano plot in hydrogen electrocatalysis[40], indicating that the HER activity may also be affected by other factors.

3.4.2. Tafel Analysis of Co-$^{S}MoS_2$ and Ni-$^{S}MoS_2$

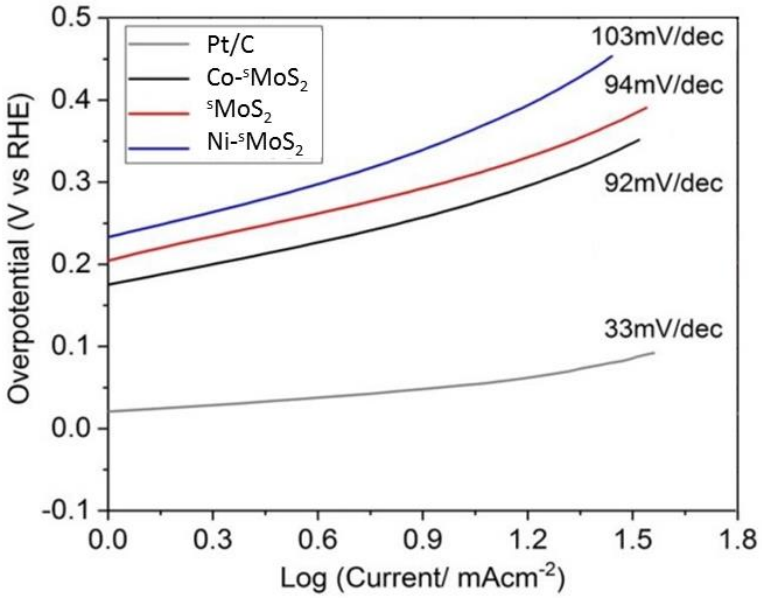


Figure 3.6 Tafel analysis of Co-$^{S}MoS_2$ and Ni-$^{S}MoS_2$ (a) Tafel plot of Co-$^{S}MoS_2$, $^{S}MoS_2$ and, Ni-$^{S}MoS_2$ and 20%Pt/C.

To elucidate this relationship, Ni-$^{S}MoS_2$ and Co-$^{S}MoS_2$ were particularly selected for comparison. Tafel analysis was performed on both materials to understand the inherent electrochemical HER reaction mechanism, as shown in Figure 3.6a. The reference 20% Pt/C catalyst gives a Tafel slope of 33 mV/dec, which is similar to previous results obtained elsewhere.[41,42] The Tafel slopes of Ni-$^{S}MoS_2$ and Co-$^{S}MoS_2$ have close values of 103mV/dec and 92mV/dec, respectively. Both values are similar to that of pristine $^{S}MoS_2$ (94mV/dec); this suggests that all three MoS_2 nanosheets follow the Volmer-Heyrovsky mechanism, as reported in the literature[27]. Since hydrogen adsorption is the rate

determining step for Volmer-Heyrovsky mechanism, the HER activity of the doped $^{S}MoS_2$ catalyst depends on the H adsorption enthalpy of MoS_2 at the basal plane, which is expected to be affected by choice of metal dopants.

3.4.3. Stability Test of Co-$^{S}MoS_2$ and Ni-$^{S}MoS_2$

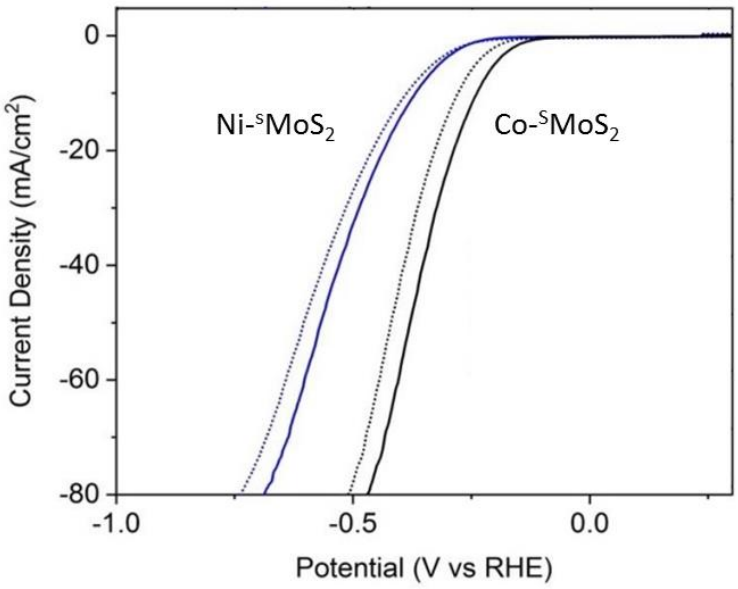


Figure 3.7 Stability tests of Co-$^{S}MoS_2$ and Ni-$^{S}MoS_2$. Co-$^{S}MoS_2$ (black line) and Ni-$^{S}MoS_2$ (blue line) before (Solid line) and after (dotted line) 1000 repeat scans at a scan rate of 50mVs^{-1}.

After the catalyst ink are dropcasted onto the surface of working electrode, possible restacking of nanosheets are likely to occur after a long period of electrochemical reactions and some of the surface metal dopants may be leached out as well. The electrochemical stability test was carried out to analyse the doping stability of the two doped $^{S}MoS_2$ samples. Figure 3.7 shows the comparisons of the catalytic performances of Co-$^{S}MoS_2$ and Ni-$^{S}MoS_2$ before and after 1000 LSV scans. Despite a small increase in onset potential, the results show that both catalysts retain most of their HER activities. This suggests that most of the metal dopants were firmly attached onto the surface of $^{S}MoS_2$ during the hydrogen production.

3.5 Doping Environment of isolated TM atoms

3.5.1. HR-STEM images

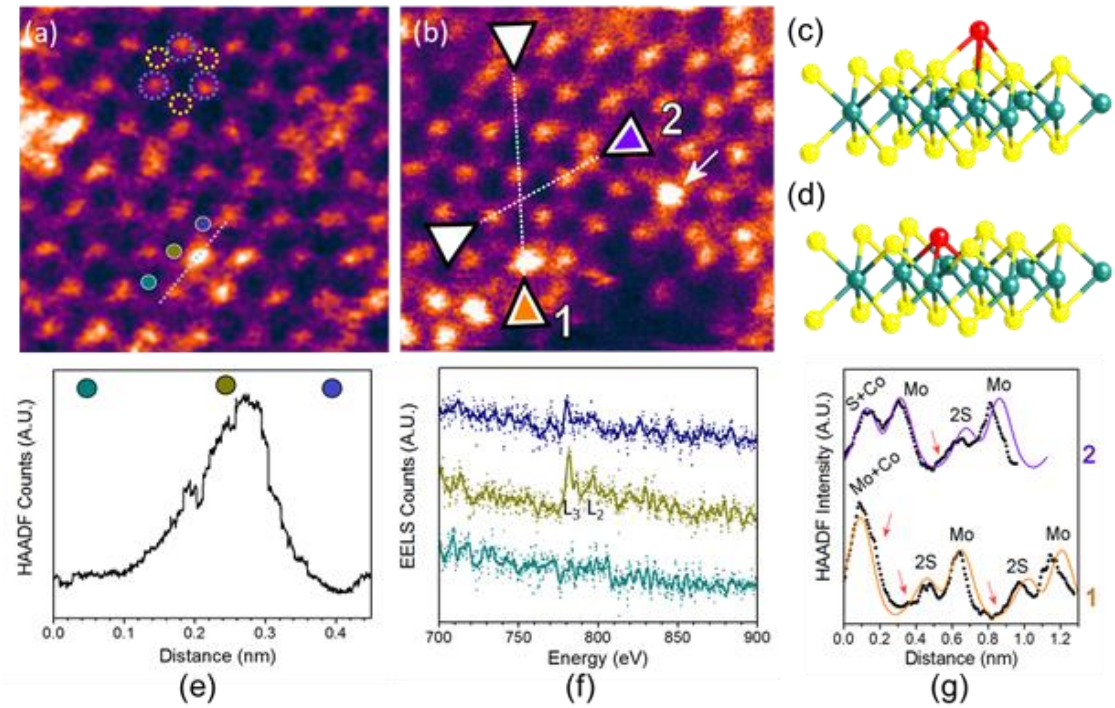


Figure 3.8 HAADF-STEM image of Co-SMoS_2. (a) and (b) HAADF-STEM image of Co-$^{S}MoS_2$. Simultaneous acquisition (c) Co at Mo-atop site model (d) Co at S Vacancy site model (e) ADF and (f) EELS acquired along the line in a. (g) ADF intensity line profiles taken along the numbered line 1 and 2 in b (<110> direction). Red arrows in the plot indicate sample drift during image acquisition.

To analyse the specific locations of the two transition metal Co and Ni dopants which show contrasting electro-catalytic properties on the basal plane of $^{S}MoS_2$, High-Angle Annular Dark-Field (HAADF) imaging and Electron Energy Loss Spectroscopy (EELS) mapping of Co-$^{S}MoS_2$ (Figure 3.8) and Ni-$^{S}MoS_2$ (Figure 3.9) were performed by High-Resolution Scanning Transmission Electron Microscopy (HR-STEM) and simulation (Figure 3.10). Both STEM analyses of the two samples show a characteristic and well-ordered hexagonal pattern of honey-comb like structure which corresponds to monolayer 2H-$^{S}MoS_2$. Due to the Z contrast nature of ADF imaging, Mo atoms (blue, Figure 3.8a) would appear to be brighter than S atoms (yellow, Figure 3.8a). In Figure 3.8b, at least

two major types of Co dwelling sites are clearly observed. First, a very bright image feature appears on top of Mo position and sandwiched by S atoms (white arrow). This is attributed to the single Co atom sitting on top of the trigonal prismatic Mo atom (Mo atop site). (Figure 3.8d) The similar features can also be observed on S positions (yellow arrow) (Figure 3.8c), which can be attributed to a Co atom incorporated into the S vacant position (Co substituted S vacant site).

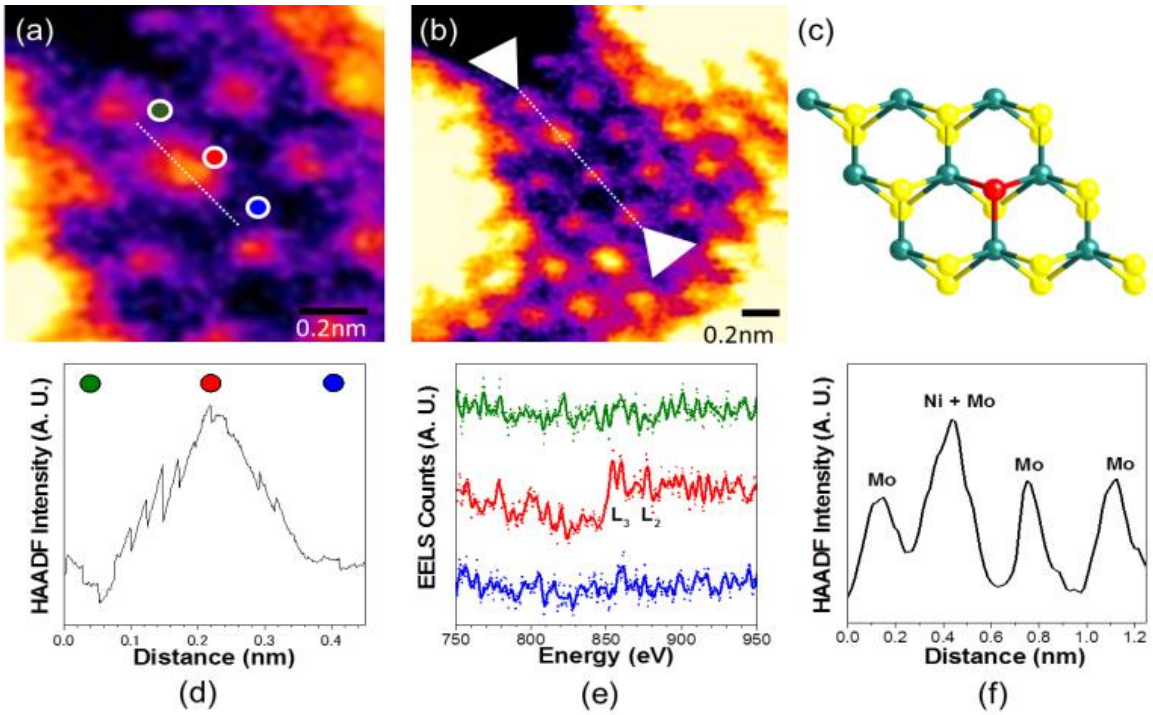


Figure 3.9. HAADF-STEM image of Ni-SMoS2. (a) and (b) HAADF-STEM image of Ni-SMoS2. (c) ADF and (d) EELS acquired along the line in b. (f) ADF intensity line profile acquired along the line in b of the Mo sites in <100> direction.

For both samples, intensity profiles of the ADF image were taken across the doped sites in <110> direction and the corresponding atomic compositions of the peaks were assigned (Figure 3.8e and Figure 3.8f). ADF-EELS simultaneous acquisition line-scans were taken across a line containing the either the single Co or Ni metal dopants (Co: Figure 3.8e, f and Ni: Figure 3.9d, e). For Co-$^{S}MoS_2$, the EELS extracted from before (green), on (dark blue), and after (khaki) the Co atom on Mo top site are shown in Figure

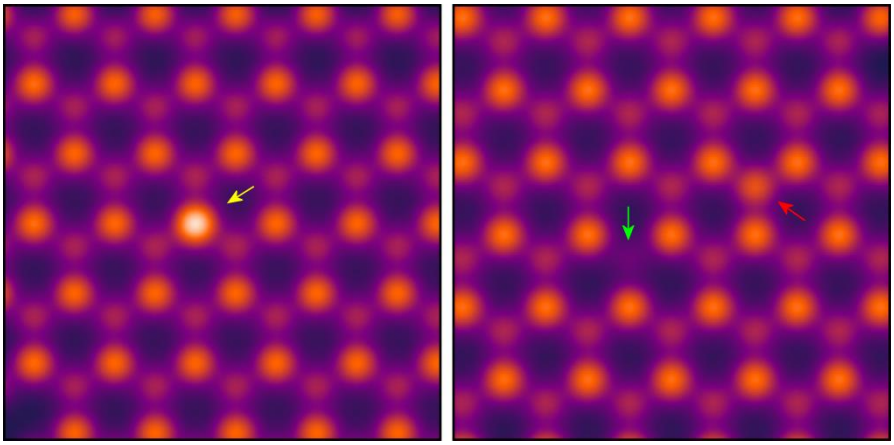


Figure 3.10 STEM image simulations. Yellow arrow shows a single TM atom on Mo, green arrow shows a single S vacancy, and red arrow shows a TM substituted for S.

3.8f. The characteristic $L_{3,2}$ edges occur at the expected energy in the EELS extracted from Co on top of Mo site, and are absent in the two other EELS. Both atop (Figure 3.9e, f) and substituted S vacant sites (Figure3.11) can also be observed for Ni-$^{S}MoS_2$. The appearance of corresponding characteristic $L_{3,2}$ edges at the original Mo position (Red circle), comparing to before (green) and after (blue), confirms the presence of Ni atom (Figure 3.9e and 3.9f). This is further supported by the ADF analysis along the Mo sites in <100> direction, which the larger peak (red) is contributed by Ni doping on top of Mo atom (Mo atop site).

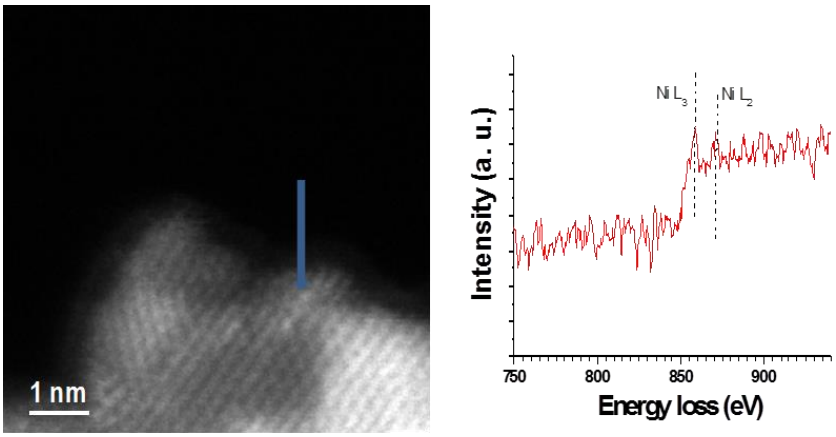


Figure 3.11 Ni substituted S vacant site in exfoliated Ni-$^{S}MoS_2$ (left) and EELS acquired along the S vacant site in <100> direction. (right)

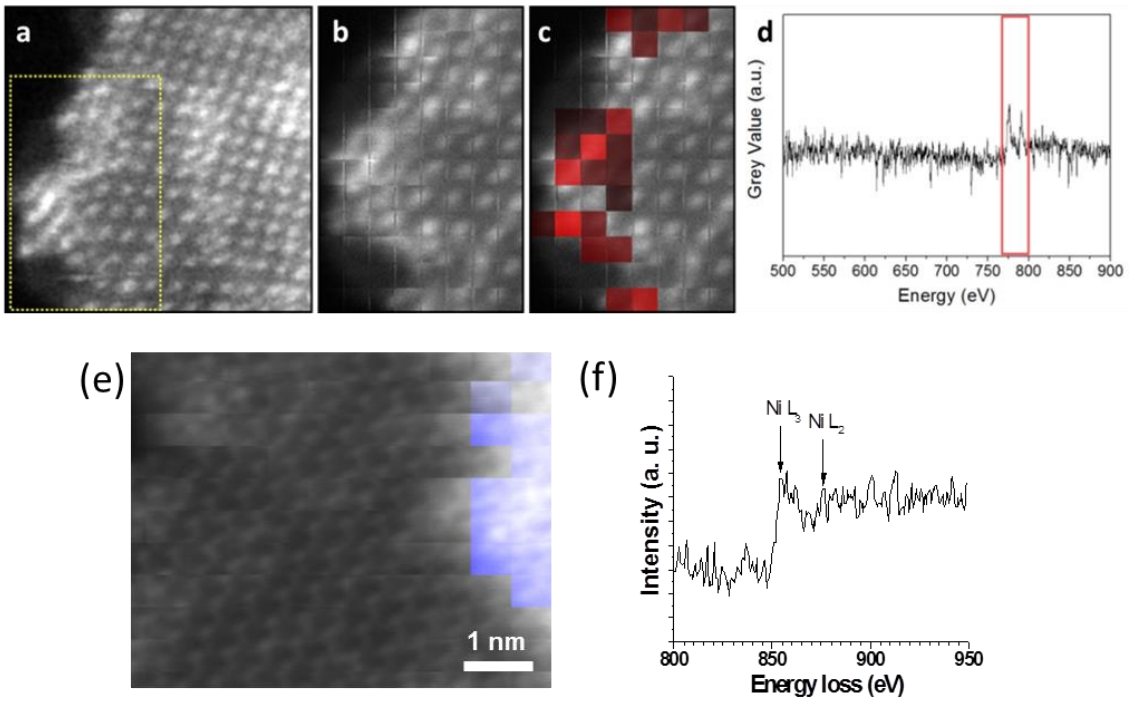


Figure 3.12 ADF image and EELS intensity mapping from the edge region of Co-$^{S}MoS_2$ and Ni-$^{S}MoS_2$. (a) STEM images of Co-$^{S}MoS_2$ at edge sites. (b) and (c): The simultaneous acquisition ADF-STEM and EELS intensity mapping from the boxed region in (a). (d) EELS extracted from a 3 × 3 bin from (c) showing the $L_{2,3}$ Co peaks. The red box confirms the presence of Co atoms from the EELS integrated intensity in the energy window 770–800 eV (Co $L_{3,2}$ edge). (e) ADF image and EELS intensity mapping from the edge region. (f) EELS extracted from a 3 × 3 bin from (e) showing the $L_{2,3}$ Ni peaks. The Ni is located at edge of multilayer MoS_2.

Although we detected occasionally the presence of the two metals by EELS on the edges of layers (Figure 3.12), the large quantity and increasing number of basal sites with a significant increase in surface area compared to peripheral edge sites of reducing MoS_2 slab size due to exfoliation make the metal doped basal sites a more dominant feature. Thus, the imaging results provide the direct experimental evidence of the successful doping of Co atom and Ni atom onto these basal planes of $^{S}MoS_2$ of our exfoliated samples. Particularly, the chemisorption of Co or Ni precursor directly on the abundant atop sites of the intact basal plane of $^{S}MoS_2$ is envisaged to offer the accommodation of these transition metal atoms/ions in a significant quantity. It is also logical to assume that

the Co or Ni precursor can occupy some surface S vacancies of $^{S}MoS_2$ generated via the nBuLi exfoliation to establish Co-Mo or Ni-Mo interactions with the exposed Mo sites on the ruptured tri-atomic MoS_2 layer. However, our STEM-EELS characterization so far was not able to offer any quantitative assessment of their main rooting sites for the two transition metals. According to our molecular model of single tri-atomic MoS_2 layer, metal M on Mo atop site of the basal plane of $^{S}MoS_2$ (Figure 3.13a) exerts somewhat similar geometric characteristics to form M-S interactions to that of M doped S edge (Figure 3.13d), as described in the S edge model (Figure 3.13c). Similarly, when M substitutes S vacant site of the partial damaged basal plane of $^{S}MoS_2$ (Figure 3.13b), M-Mo interactions can be formed. This is akin to that of M-doped Mo edge structure (Figure 3.13e). Thus, the S vacancies on the monolayer MoS_2 structure allow free access to the interior Mo sites modified by the chemisorbed M sulphide complex (akin to Mo edge sites), which functions very similarly to the edge structure modification.

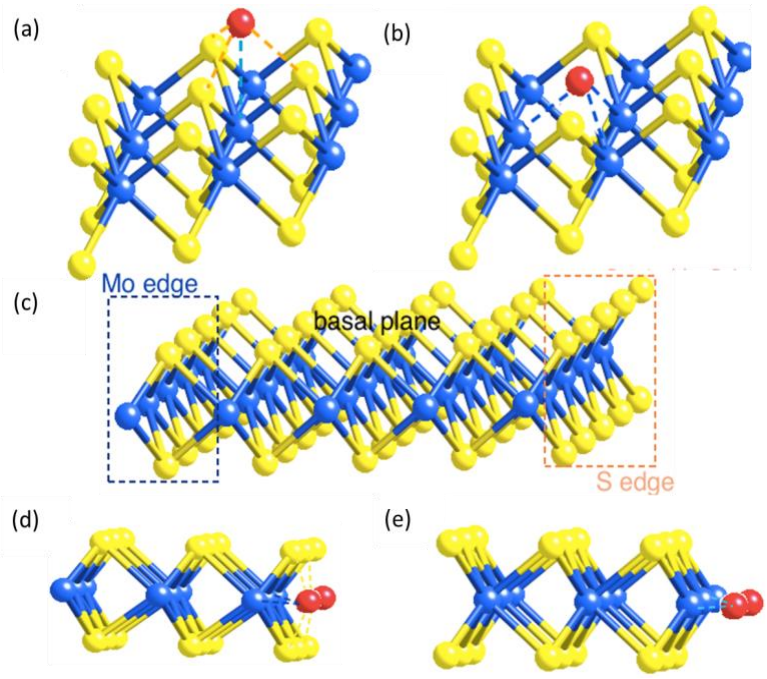


Figure 3.13 molecular model of $^{S}MoS_2$ and TM-$^{S}MoS_2$ (a) a metal atom on Mo top site of TM-$^{S}MoS_2$ (b) metal on S vacancy site of TM-$^{S}MoS_2$ (c) monolayer of a perfect triatomic $^{S}MoS_2$ (d) Metal doped S edge of MMoS2 (e) Metal-doped Mo edge of TM-$^{S}MoS_2$

3.5.2. EXAFS

The chemical environments of Co and Ni were then examined by Extended X-ray Absorption Fine Structure Spectroscopy (EXAFS). Figure 3.14(a) and 3.14(b) show the results of Fourier transforms of Co and Ni K-edge of Co-$^{S}MoS_2$ and Ni-$^{S}MoS_2$. All the parameters are fitted with acceptable Debye-Waller factors as listed in Table 3.2(a) and 3.2(b), respectively. Both EXAFS results show that there is no first-shell Co-Co or Ni-Ni contribution, suggesting that the major species of Co and Ni on the basal plane of nanosheets are indeed not in the form of metal clusters nor nanoparticles but single metal atoms/ions, as suggested from the HAADF-STEM images (see Figures 3.8 and 3.9). It is interesting to note that there is only a first shell Co-S contribution with a coordination number of about 4 (tetrahedron) at 2.27 ± 0.01 Å for Co-$^{S}MoS_2$ and a first shell Ni-S contribution with a coordination number of about 6 (octahedron) at 2.29 ± 0.01 Å for Ni-$^{S}MoS_2$. (Table 3.2). There is no first shell Co-Mo or Ni-Mo contribution, suggesting that the majority of Co and Ni species are indeed mainly on the atop sites (chemisorbed sites) of $^{S}MoS_2$, since if M (Co or Ni) on S vacancies or Mo edge sites occur at significant extent would generate the corresponding first shell of M-Mo interaction. Part of first shell sulphide ligands of these two immobilized metal sulphides must be derived from the surface sulphide groups, presumably from the higher degree of exposure of the basal MoS_2 plane during the synthesis.

The higher affinity for octahedral coordinated $3d^8$ Ni^{2+} over tetrahedral coordinated $3d^7$ Co^{2+} with sulphide ligands due to greater ligand field stabilization energy accounts for the fundamental difference in coordination environment.[35] However, it is very interesting to find that the best fit data for Ni-$^{S}MoS_2$ depicts the presence of Ni-Mo interaction at second shell of 2.56 ± 0.04 Å with CN of 1.2 ± 0.3 whereas absolutely no Co-Mo

interaction is detected in Co-$^{S}MoS_2$. Considering the larger size of Co (152 pm) and its tetrahedral coordination the 'Co-Mo' distance between the shared triangular face with prismatic Mo (octahedron) is shorter than typical Co-Mo bond from a simple geometric model. It therefore destabilizes the closed face sharing for the Co-Mo formation. On the other hand, the smaller size of Ni (149 pm) and its octahedral coordination can accommodate well the stereospecific Ni-Mo interaction with the surface Mo site. The rigid close packed face-sharing model of chemisorbed transition metal sulphide can account for the absence of Co-Mo interaction but facilitates the Ni-Mo interaction for the same atop Mo site.

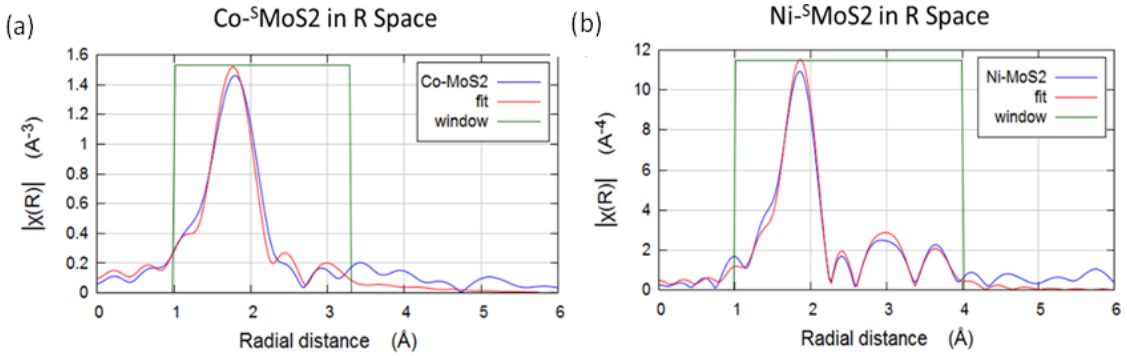


Figure 3.14. Fourier transforms of k3-weighted Co and Ni K-edge of Extended X-ray absorption fine structure spectroscopy (EXAFS) spectra of (a) Co-$^{S}MoS_2$ and (b) Ni-$^{S}MoS_2$.

Table 3.2 EXAFS scattering path analysis of Co-$^{S}MoS_2$ and Ni-$^{S}MoS_2$

Scattering path	Bond length (Å)	Coordination number	σ^2
Co-S	2.27 ± 0.01	3.9 ± 0.3	0.007

R=0.9%, Kwt=1,2,3; k range 3-12; R range 1-3; Enot 0.23

Scattering path	Bond length (Å)	Coordination number	σ^2
Ni-S	2.29 ± 0.01	6.5 ± 0.3	0.008
Ni-Mo	2.56 ± 0.04	1.2 ± 0.3	0.011

R=1.8% Kwt=1,2,3; k range 3-12; R range 1-3; Enot 0.1

(*Enot is the energy difference of absorption energy in experimental value and calculated value.)

3.6 The role of single TM atoms for H adsorption

The favourability to incorporate single metal atom M onto $^{S}MoS_2$ is believed to cause the distinctive HER activity for electrochemical hydrogen production. There have also been previous attempts to model activity by doping single transition metal atoms onto the edge sites.[44–46] Gibbs free energy of hydrogen adsorption (ΔG_H) is generally used as a descriptor for HER activity. It is believed ΔG_H plays an important role in electrochemical production of hydrogen gas; too weak H adsorption on surface will not favour the electrochemical reaction but too strong H adsorption would not facilitate H_2 recombination and desorption. Thus, this theoretical value should be as close as to 0 to maximise the overall thermodynamic enthalpy value for H surface adsorption, surface recombination and desorption processes in HER, as previous discussed[46].

Since our electrochemical HER measurements in section 4.3 cannot be simply explained by volcano plot (Sabatier plot) in hydrogen electrocatalysis, we expected that the doping of single transition metal will alter the electronic properties of surrounding Mo and S atoms. Thus, the relationship between the rate of HER and the doping effect of the metal atoms at the Mo atop site on the basal plane are rationalised with the help of the calculated density of states (DoS) spectra of the three MoS_2 samples ($^{S}MoS_2$, Co-$^{S}MoS_2$, Ni-$^{S}MoS_2$) analysis (with the Fermi energy level is arbitrary set as 0) (Figure 3.15). In general, the filled valance bands (VB) and empty conduction bands (CB) in the DoS of MoS_2 are composed of both S-3p and Mo-4d states. From Tafel analysis in Section 3.4.2, we understand that hydrogen generation for all three MoS_2 samples will progress through the Volmer-Heyrovsky mechanism. H^+ reduction, as its rate determining step, is taking place by promoting electrons from VB to the empty CB by electrical means.

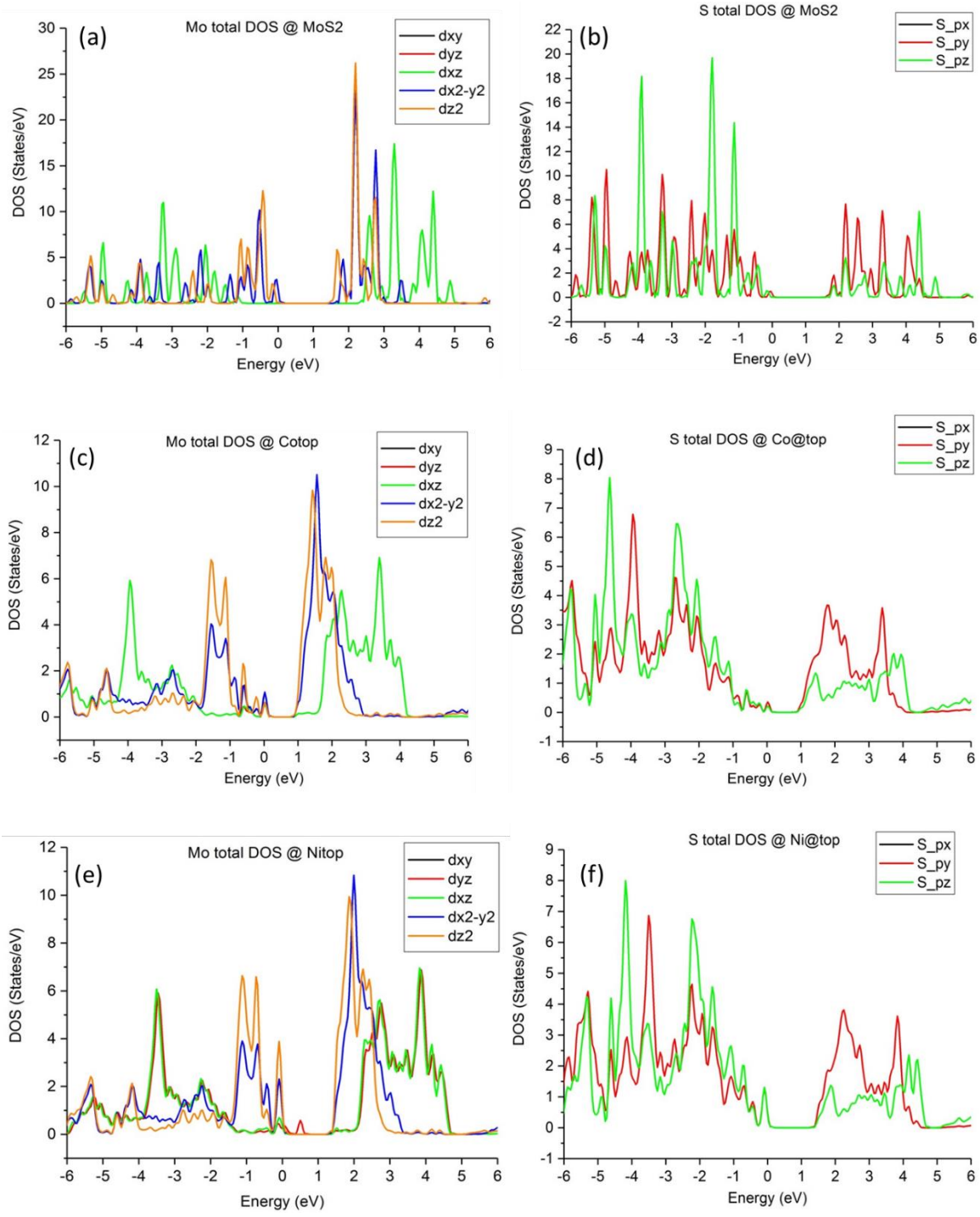


Figure 3.15 Calculated density of states (DoS) spectra. (a) Mo4d state and (b) S3p state of $^{S}MoS_2$. (c) Mo4d state and (d) S3p state of Co-$^{S}MoS_2$, (e) Mo4d state and (f) S3p state of Ni-$^{S}MoS_2$

According to previous computational results from the literature[46,47], the H^+ reduction energy level (H^+/H_2) for unmodified MoS_2 is close to the lower part of CB, which is predominantly occupied by empty Mo-4dx^2-y^2 and Mo-4dz^2 bands. Therefore, hydrogen will be mainly generated from Mo sites with a small contribution from S sites in pristine MoS_2, as is also described by the edge model[36]. The value of Gibbs free energy of hydrogen adsorption by Mo component ($\Delta G_{H\text{-}Mo}$) in this case will be small and close to zero. It is expected that the addition of 3d transition metal atom (Co and Ni) onto the Mo atop site will cause a downshift on both empty S-3p and Mo-4d CB bands. From our calculated DoS spectra, Co doping will induce a more remarkable downshift of empty CB than that of Ni doping (Figure 3.17). Due to the absence of Co-Mo interaction from our EXAFS results, it can be predicted that the H^+ reduction energy level in Co-^{S}MoS_2 will now be very close to the upper level of the empty CB occupied by S-3p, thus the value of Gibbs free energy of hydrogen adsorption by S component ($\Delta G_{H\text{-}S}$) is close to zero. H^+ reduction therefore mainly takes place over S sites. For Ni-^{S}MoS_2, due to the smaller downshift of the CB as seen from our calculated bands, the H^+ reduction level this time should rest near the centre of the CB. While the contributions by both Mo and S to the overall H_2 production are similar but not close to their individual S or Mo component centres, they give smaller hydrogen contributions from both sites. This model is consistent with the computational analysis on the change of ΔG_H due to edge sites modification by Wang et al.[46] Overall, due to different degree of downshifting on both S-3p and Mo-4d components in the CB as compared to ^{S}MoS_2, Co atom selectively sitting at Mo atop sites will enhance the HER activity while Ni located on the same sites with the stereospecific allowed Ni-Mo interaction will show a much lower HER performance compared to undoped MoS_2.

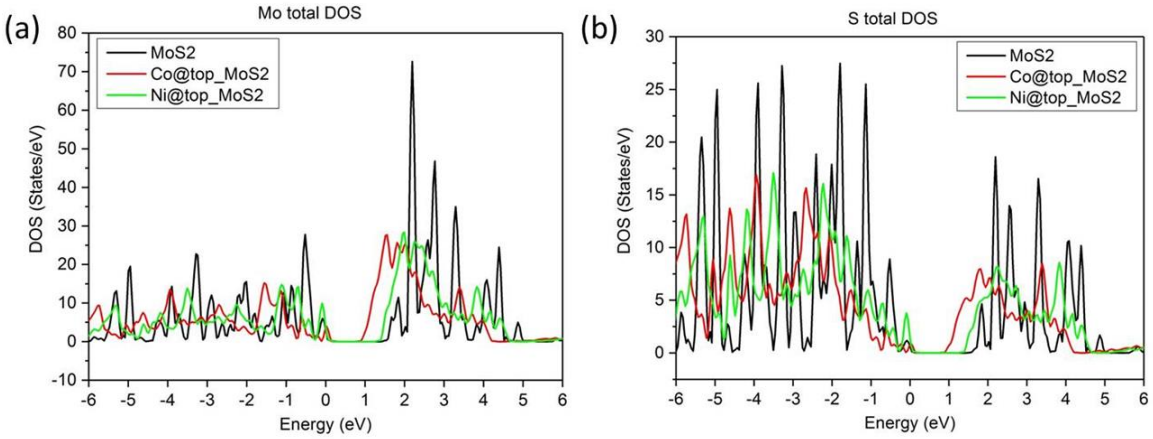


Figure 3.16 Overlap plot of (a) Mo-4d state and (b) S3p of the three DOS spectra

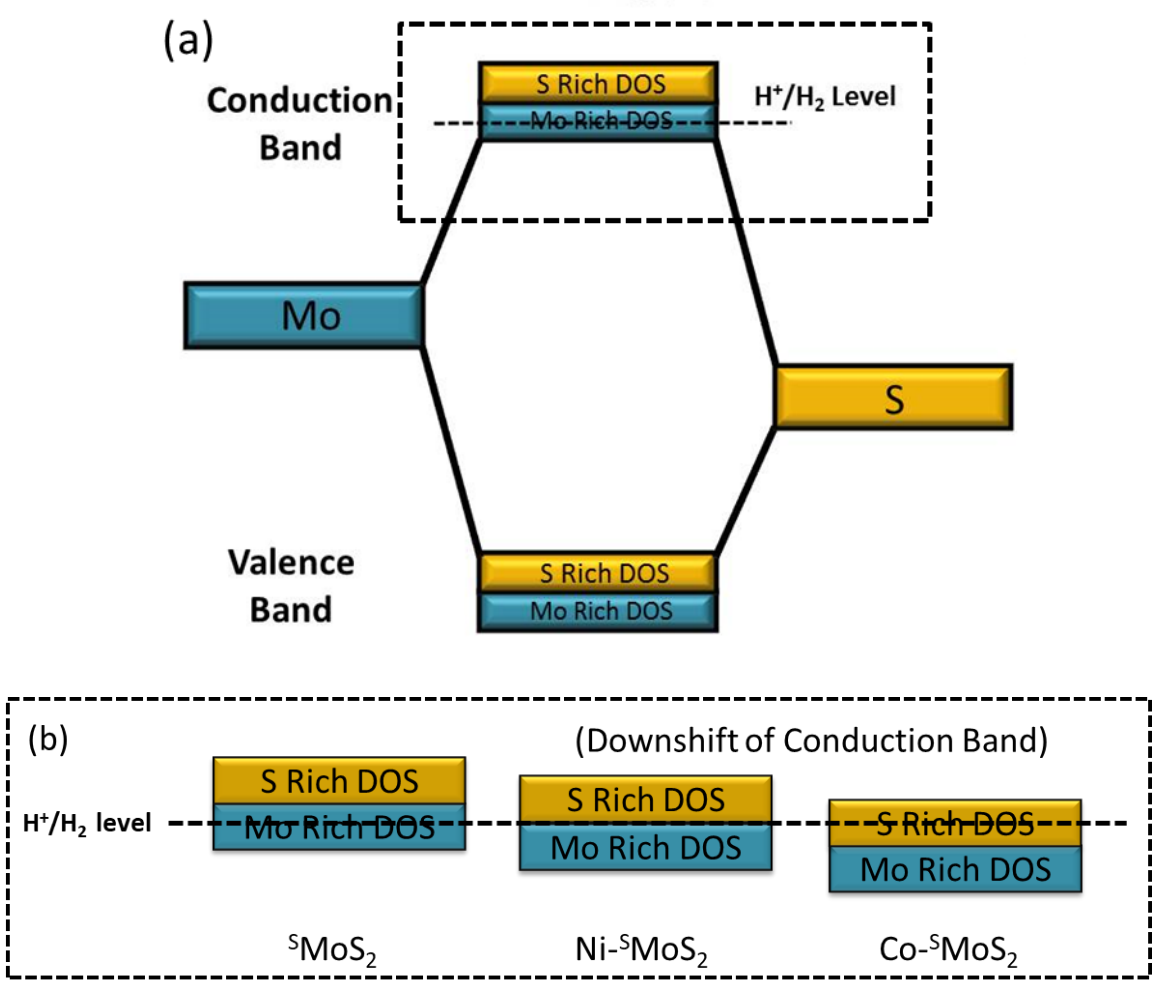


Figure 3.17 (a) Schematic of energy alignment of MoS_2 (b) Hypothesised CB position of three MoS_2 materials with respect to the proton reduction energy level after downshift of conduction band

3.7 Conclusions

In conclusion, we have provided direct experimental evidence that transition metal atoms can be chemically attached to the multiple surface sites of basal plane of the exfoliated 2H $^{S}MoS_2$. From the HADDF-STEM image and EXAFS analysis the data suggest that the majority of metal dopants are attached to the Mo atop sites on the basal $^{S}MoS_2$ plane as chemisorbed sulphide complexes. Thus, the anchored tetrahedral coordinated Co can affect the surface neighbour S active sites through Co-S interaction on the basal plane in attenuating the ΔG_H towards zero value at high hydrogen coverage, hence enhancing the HER activity. On the other hand, the geometric constraints of the large size Co atom in tetrahedral arrangement deny the direct influence of Mo site on $^{S}MoS_2$ with no Co-Mo interaction. In contrast, the chemisorbed octahedral Ni sulphide on the same atop site allows the direct electronic modification of Mo site by establishing Ni-Mo interaction, which deviates the ΔG_H from zero of the surface exposed Mo sites at high hydrogen coverage, hence greatly attenuating the HER activity. It is believed that both the geometric and electronic factors exerted by transition metal dopants are therefore important parameters in further tuning the 2D MoS_2 structure for rational design of the composite materials for more efficient electrochemical hydrogen production from water.

3.8 References

(1) Rausch, B.; Symes, M. D.; Chisholm, G.; Cronin, L. Decoupled Catalytic Hydrogen Evolution from a Molecular Metal Oxide Redox Mediator in Water Splitting. **2014**, *345*, 2–7.

(2) Fokas, A.; Kibble, T. W. B.; Grigoriou, A.; Zegarlinski, B. Enhancing Hydrogen Evolution Activity in Water Splitting by Tailoring Li+-Ni(OH)2-Pt Interfaces. **2011**, No. December, 1256–1261.

(3) McKone, J. R.; Marinescu, S. C.; Brunschwig, B. S.; Winkler, J. R.; Gray, H. B. Earth-Abundant Hydrogen Evolution Electrocatalysts. *Chem. Sci.* **2014**, *5*, 865–878.

(4) Thoi, V. S.; Sun, Y.; Long, J. R.; Chang, C. J. Complexes of Earth-Abundant Metals for Catalytic Electrochemical Hydrogen Generation under Aqueous Conditions. *Chem. Soc. Rev.* **2013**, *42*, 2388–2400.

(5) Robertson, I. H.; O'Connell, R. Earth-Abundant Catalysts for Electrochemical and Photoelectrochemical Water Splitting. *Atten. Time* **2012**.

(6) Liang, K. S.; Chianelli, R. R.; Chien, F. Z.; Moss, S. C. The Term " Poorly Crystalline ," Used Here to Describe Our Samples , Is Not. *J. Non-Crystallin Solids* **1986**, *79*, 251–273.

(7) Hinnemann, B.; Moses, P. G.; Bonde, J.; Jørgensen, K. P.; Nielsen, J. H.; Horch, S.; Chorkendorff, I.; Nørskov, J. K. Biomimetic Hydrogen Evolution: MoS2nanoparticles as Catalyst for Hydrogen Evolution. *J. Am. Chem. Soc.* **2005**, *127*, 5308–5309.

(8) Jaramillo, T. F.; Jørgensen, K. P.; Bonde, J.; Nielsen, J. H.; Horch, S.; Chorkendorff, I. Identification of Active Edge Sites for Electrochemical H_2 Evolution from MoS_2

Nanocatalysts</Div>. *Science (80-.).* **2007**, *317*, 100 LP-102.

(9) Nørskov, J. K.; Bligaard, T.; Logadottir, A.; Kitchin, J. R.; Chen, J. G.; Pandelov, S.; Stimming, U. Trends in the Exchange Current for Hydrogen Evolution. *J. Electrochem. Soc.* **2005**, *152*, J23.

(10) Nanocatalysts, M.; Jaramillo, T. F.; Jørgensen, K. P.; Bonde, J.; Nielsen, J. H.; Horch, S.; Chorkendorff, I. Identification of Active Edge Sites for Electrochemical H2 Evolution from MoS2 Nanocatalysts. *Science (80-.).* **2007**, *317*, 100–102.

(11) Tsai, C.; Chan, K.; Nørskov, J. K.; Abild-Pedersen, F. Theoretical Insights into the Hydrogen Evolution Activity of Layered Transition Metal Dichalcogenides. *Surf. Sci.* **2015**, *640*, 133–140.

(12) Kibsgaard, J.; Chen, Z.; Reinecke, B. N.; Jaramillo, T. F. Engineering the Surface Structure of MoS2 to Preferentially Expose Active Edge Sites for Electrocatalysis. *Nat. Mater.* **2012**, *11*, 963–969.

(13) Li, S.; Wang, S.; Salamone, M. M.; Robertson, A. W.; Nayak, S.; Kim, H.; Tsang, S. C. E.; Pasta, M.; Warner, J. H. Edge Enriched 2D MoS2 Thin Films Grown by Chemical Vapor Deposition for Enhanced Catalytic Performance. *Acs Catal.* **2016**, *7*, 877–886.

(14) Ye, G.; Gong, Y.; Lin, J.; Li, B.; He, Y.; Pantelides, S. T.; Zhou, W.; Vajtai, R.; Ajayan, P. M. Defects Engineered Monolayer MoS2 for Improved Hydrogen Evolution Reaction. *Nano Lett.* **2016**, *16*, 1097–1103.

(15) Tsai, C.; Abild-Pedersen, F.; Nørskov, J. K. Tuning the MoS_2 Edge-Site Activity for Hydrogen Evolution via Support Interactions. *Nano Lett.* **2014**, *14*, 1381–1387.

(16) Hou, D.; Zhou, W.; Liu, X.; Zhou, K.; Xie, J.; Li, G.; Chen, S. Electrochimica Acta Pt Nanoparticles / MoS 2 Nanosheets / Carbon Fi Bers as Ef Fi Cient Catalyst for the Hydrogen Evolution Reaction. **2015**, *166*, 26–31.

(17) Li, H.; Tsai, C.; Koh, A. L.; Cai, L.; Contryman, A. W.; Fragapane, A. H.; Zhao, J.; Han, H. S.; Manoharan, H. C.; Abild-Pedersen, F.; Nørskov, J. K.; Zheng, X. Activating and Optimizing MoS2 Basal Planes for Hydrogen Evolution through the Formation of Strained Sulphur Vacancies. *Nat. Mater.* **2015**, *15*, 48–53.

(18) Ye, G.; Gong, Y.; Lin, J.; Li, B.; He, Y.; Pantelides, S. T.; Zhou, W.; Vajtai, R.; Ajayan, P. M. Defects Engineered Monolayer MoS2for Improved Hydrogen Evolution Reaction. *Nano Lett.* **2016**, *16*, 1097–1103.

(19) Tsai, C.; Li, H.; Park, S.; Park, J.; Han, H. S.; Nørskov, J. K.; Zheng, X.; Abild-Pedersen, F. Electrochemical Generation of Sulfur Vacancies in the Basal Plane of MoS2 for Hydrogen Evolution. *Nat. Commun.* **2017**, *8*, 1–8.

(20) Wu, W.; Niu, C.; Wei, C.; Jia, Y.; Li, C.; Xu, Q. Activation of MoS2 Basal Planes for Hydrogen Evolution through Zinc. *Angew. Chemie Int. Ed.* **2019**, 1–6.

(21) Xu, Y.; Wang, L.; Liu, X.; Zhang, S.; Liu, C.; Yan, D.; Zeng, Y.; Pei, Y.; Liu, Y.; Luo, S. Monolayer MoS_2 with S Vacancies from Interlayer Spacing Expanded Counterparts for Highly Efficient Electrochemical Hydrogen Production. *J. Mater. Chem. A* **2016**, *4*, 16524–16530.

(22) Chhowalla, M.; Shin, H. S.; Eda, G.; Li, L.-J.; Loh, K. P.; Zhang, H. The Chemistry of Two-Dimensional Layered Transition Metal Dichalcogenide Nanosheets. *Nat. Chem.* **2013**, *5*, 263–275.

(23) Cunningham, G.; Lotya, M.; Cucinotta, C. S.; Sanvito, S.; Bergin, S. D.; Menzel, R.; Shaffer, M. S. P.; Coleman, J. N. Solvent Exfoliation of Transition Metal Dichalcogenides : Dispersability of Exfoliated Nanosheets Varies Only Weakly Between Compounds Solvent Exfoliation of Transition Metal Dichalcogenides : Dispersability of Exfoliated Nanosheets Varies Only Weakly Bet. *ACS Nano* **2012**, *6*, 3468–3480.

(24) Wang, Q. H.; Kalantar-Zadeh, K.; Kis, A.; Coleman, J. N.; Strano, M. S. Electronics and Optoelectronics of Two-Dimensional Transition Metal Dichalcogenides. *Nat. Nanotechnol.* **2012**, *7*, 699–712.

(25) Bhandavat, R.; David, L.; Singh, G. Synthesis of Surface-Functionalized WS2 Nanosheets and Performance as Li-Ion Battery Anodes. *J. Phys. Chem. Lett.* **2012**, *3*, 1523–1530.

(26) Eda, G.; Yamaguchi, H.; Voiry, D.; Fujita, T.; Chen, M.; Chhowalla, M. Photoluminescence from Chemically Exfoliated MoS 2. *Nano Lett.* **2011**, *11*, 5111–5116.

(27) Shi, Y.; Huang, J.-K.; Jin, L.; Hsu, Y.-T.; Yu, S. F.; Li, L.-J.; Yang, H. Y. Selective Decoration of Au Nanoparticles on Monolayer MoS2 Single Crystals. *Sci. Rep.* **2013**, *3*, 1839.

(28) Merki, D.; Vrubel, H.; Rovelli, L.; Fierro, S.; Hu, X. Fe, Co, and Ni Ions Promote the Catalytic Activity of Amorphous Molybdenum Sulfide Films for Hydrogen Evolution. *Chem. Sci.* **2012**, *3*, 2515.

(29) Wang, D.; Zhang, X.; Shen, Y.; Wu, Z. Ni-Doped MoS_2 Nanoparticles as Highly Active Hydrogen Evolution Electrocatalysts. *RSC Adv.* **2016**, *6*, 16656–16661.

(30) Liu, G.; Robertson, A. W.; Li, M. M.-J. J.; Kuo, W. C. H. H.; Darby, M. T.; Muhieddine, M. H.; Lin, Y.-C. C.; Suenaga, K.; Stamatakis, M.; Warner, J. H.; Tsang, S. C. E. MoS2 Monolayer Catalyst Doped with Isolated Co Atoms for the Hydrodeoxygenation Reaction. *Nat. Chem.* **2017**, *9*, 810–816.

(31) Kresse, G.; Furthmüller, J. Self-Interaction Correction to Density Functional Approximation for Many Electron Systems. *Phys. Rev. B* **1996**, *54*, 11169.

(32) Perdew, J. P.; Burke, K.; Ernzerhof, M. D. of Physics and NOL 70118 J. Quantum Theory Group Tulane University. *Phys. Rev. Lett* **1996**, *77*, 3865–3868.

(33) Blöchl, P. E. Projector Augmented-Wave Method. *Phys. Rev. B* **1994**, *50*.

(34) Kohn, W.; Sham, L. J. Self-Consistent Equations Including Exchange and Correlation Effects. *Phys. Rev.* **1965**, *140*, A1133--A1138.

(35) Acerce, M.; Voiry, D.; Chhowalla, M. Metallic 1T Phase MoS2nanosheets as Supercapacitor Electrode Materials. *Nat. Nanotechnol.* **2015**, *10*, 313–318.

(36) Coulier, L.; de Beer, V. H. J.; van Veen, J. A. R.; Niemantsverdriet, J. W. On the Formation of Cobalt-Molybdenum Sulfides in Silica-Supported Hydrotreating Model Catalysts. *Top. Catal.* **2000**, *13*, 99–108.

(37) Kibsgaard, J.; Tuxen, A.; Knudsen, K. G.; Brorson, M.; Topsøe, H.; Lægsgaard, E.; Lauritsen, J. V.; Besenbacher, F. Comparative Atomic-Scale Analysis of Promotional Effects by Late 3d-Transition Metals in MoS2 Hydrotreating Catalysts. *J. Catal.* **2010**, *272*, 195–203.

(38) Armentrout, P. B.; Halle, L. F.; Beauchamp, J. L. Periodic Trends in Transition Metal-Hydrogen, Metal-Carbon, and Metal-Oxygen Bond Dissociation Energies. Correlation with Reactivity and Electronic Structure. *J. Am. Chem. Soc.* **1981**, *103*, 6501–6502.

(39) Simões, J. A. M.; Beauchamp, J. L. Transition Metal–Hydrogen and Metal–Carbon Bond Strengths: The Keys to Catalysis. *Chem. Rev.* **1990**, *90*, 629–688.

(40) Trasatti, S. Work Function, Electronegativity, and Electrochemical Behaviour of Metals. III. Electrolytic Hydrogen Evolution in Acid Solutions. *J. Electroanal. Chem.* **1972**, *39*, 163–184.

(41) Tavares, M. C.; Machado, S. A. S.; Mazo, L. H. Study of Hydrogen Evolution Reaction in Acid Medium on Pt Microelectrodes. *Electrochim. Acta* **2001**, *46*, 4359–4369.

(42) Ding, Q.; Song, B.; Xu, P.; Jin, S. Efficient Electrocatalytic and

Photoelectrochemical Hydrogen Generation Using MoS 2 and Related Compounds. *CHEMPR* **2016**, *1*, 699–726.

(43) Müller, U. Molecular Structures II: Compounds of Transition Metals. In *Inorganic Structural Chemistry*; John Wiley & Sons, Ltd, 2007; pp 73–84.

(44) Lauritsen, J. V.; Kibsgaard, J.; Olesen, G. H.; Moses, P. G.; Hinnemann, B.; Helveg, S.; Nørskov, J. K.; Clausen, B. S.; Topsøe, H.; Lægsgaard, E.; Besenbacher, F. Location and Coordination of Promoter Atoms in Co- and Ni-Promoted MoS2-Based Hydrotreating Catalysts. *J. Catal.* **2007**, *249*, 220–233.

(45) Schweiger, H.; Raybaud, P.; Toulhoat, H. Promoter Sensitive Shapes of Co(Ni)MoS Nanocatalysts in Sulfo-Reductive Conditions. *J. Catal.* **2002**, *212*, 33–38.

(46) Wang, H.; Tsai, C.; Kong, D.; Chan, K.; Abild-Pedersen, F.; Nørskov, J. K.; Cui, Y. Transition-Metal Doped Edge Sites in Vertically Aligned MoS2 Catalysts for Enhanced Hydrogen Evolution. *Nano Res.* **2015**, *8*, 566–575.

(47) Li, Y.; Li, Y.-L.; Araujo, C. M.; Luo, W.; Ahuja, R. Single-Layer MoS2 as an Efficient Photocatalyst. *Catal. Sci. Technol.* **2013**, *3*, 2214–2220.

Chapter 4

Sonochemical Doping of Single Transition Metal Atoms on 1T Metallic Molybdenum Disulphide Monolayers for Electrochemical Hydrogen Evolution Reaction

4.1 Introduction

In the last chapter, we have demonstrated that a number of single transition metal atom dopants (TM) can be successfully chemisorbed on the basal plane of monolayer 2H-$^{S}MoS_2$, which further lower the hydrogen adsorption free energy of the surrounding S sites and in turn enhance the HER activity.[1] Although both the density and the intrinsic activity of the active sites have vastly increased after the introduction of basal S defects, the overall HER activity of 2H-MoS_2 is still limited by sluggish charge transfer kinetics due to the semiconducting nature of the phase[2]. Thus with an intrinsic bandgap of 1.9eV[3], 2H-MoS_2 nanosheets struggle to compete with other zero band gap materials such as graphene and 2D carbide in terms of electrocatalytic activities.[4,5]

Unlike 2H-MoS_2 nanosheets, the octahedral 1T phase is found to be metallic.[6,7] However, since the 1T phase is thermally metastable, it does not occur in any natural forms of MoS_2, although 1T-MoS_2 can be synthesised through chemical exfoliation of bulk 2H-MoS_2 using Li or K intercalation.[8] The electronic properties are modified due to the structural change during phase conversion, which is evidenced by an enhanced electrical conductivity of around 10^7 times for 1T-MoS_2 as compared to 2H-MoS_2.[9] In conjunction with dramatically improved electrical conductivity, 1T-MoS_2 exhibits significantly

enhanced catalytic activity towards HER.[10,11] Indeed ΔG_{H^*} on the 1T phase is reported to be approximately 0.12 eV[12], which is comparable to that of 2H-MoS_2 with extensive S vacancies, though 1T-MoS_2 exhibits superior HER activity due to a greater number of active basal sites. Interestingly, under HER conditions the 1T phase undergoes a slight distortion to a lower energy 1T' structure that is stabilised by hydrogen adsorption during catalysis (notably in the remainder of the manuscript we refer to both phases as "1T" and do not distinguish between the two)[12–15]. *Ab initio* calculations elucidating the mechanism of HER on 1T-MoS_2 nanosheets reveal a low kinetic barrier of 0.16 eV for the Volmer step ($H^+_{(aq)} + e^- \rightarrow H^*$), indicating facile charge transfer through the catalyst. Higher barriers of 0.95 eV and between 1.19 to 1.41 eV are also reported for the Heyrovsky ($H^+_{(aq)} + H^* + e^- \rightarrow H_{2\,(g)}$) and Tafel ($2H^* \rightarrow H_{2\,(g)}$) steps, respectively.[12,15] Thus, HER on 1T-MoS_2 is not rate limited by the Volmer step but by the formation of $H_{2\,(g)}$.

Despite an array of positive results from recent advances in MoS_2 based HER materials, the catalytic activity of pure 1T-MoS_2 is still not comparable to those of TM-N-doped graphene, one of the recent most promising alternative material to 20% Pt/C[4,5]. Based on the current understanding of the HER mechanism[15], modifying 1T-MoS_2 based catalysts to enhance the HER activity must aim to further reduce the activation barrier for the Heyrovsky and/or Tafel steps in order to overcome the rate limiting H_2 formation kinetics. Unfortunately, as stated, 1T-MoS_2 is thermally metastable and can easily be reverted back to the thermodynamically stable 2H phase at around 92 ^oC[16]. This impedes structural modifications making this task somewhat difficult. While it is logical to assume that the same strategies for surface manipulation used on 2H-MoS_2 can be applied to 1T-MoS_2, most methods involve relatively vigorous reaction conditions, for example hydrothermal reactions inside an autoclave, that will compromise the integrity of the 1T

phase.[17] Herein, we report a very simple yet effective ambient condition sonochemical-assisted reductive doping method to synthesise monolayer 1T-$^{S}MoS_2$ with single transition metal adatoms that are chemisorbed at the basal plane (TM-1T-$^{S}MoS_2$, TM = Fe, Ni, Co, Pt, Pd) in a wet chemistry setup. An ambient condition synthesis prevents reconstruction of the 1T monolayer to the 2H phase, yet allows us to still gently modify the catalytic surface with interfacial dopant atoms by sonication in water/alcohol at room temperature. Using advanced analytical techniques including High-Resolution Scanning Transmission Electron Microscopy (HR-STEM) with High-Angle Annular Dark-Field (HAADF) imaging, X-ray Photoelectron Spectroscopy (XPS), X-ray Absorption Near Edge Structure (XANES), and Extended X-ray Absorption Fine Structure Spectroscopy (EXAFS), we provide direct evidence for a stable incorporation of single transition metal adatoms onto the basal plane of 1T-$^{S}MoS_2$.

We report that the resulting TM-1T-$^{S}MoS_2$ samples give an excellent performance as electrochemical HER catalysts, with Pd-1T-^{S}MoS exhibiting activity that is comparable to the best reported alternative materials to Pt/C. [5,18] Solid-State Proton Nuclear Magnetic Resonance spectroscopy (^{1}H-NMR) indicates that 1T-$^{S}MoS_2$ surface is extensively covered with hydrogen species after the HER catalysis. The kinetic Tafel and rate analyses suggest that TM-1T-$^{S}MoS_2$ clearly operate as bi-functional catalysts whereby proton reduction to adsorbed H readily occurs on the pristine 1T-$^{S}MoS_2$ before transferred to the isolated TM dopant atoms on basal sites where Tafel recombination occurs. For the most promising dopants (TM = Pt and Pd), we have elucidated the structure-activity relationship of TM-1T-$^{S}MoS_2$ catalysts using Density Functional Theory (DFT). Our calculations confer to the bifunctional catalysis and also reveal that isolated Pt and Pd atoms on the 1T-$^{S}MoS_2$ basal plane significantly lower the activation barrier for the HER

compared to the undoped analogue. This chapter will demonstrate that with proper treatment at ambient conditions, single nanosheets of $^{S}MoS_2$ can retain the metastable 1T structure upon anchoring single TM species to the basal plane and the resulting catalysts exhibit dramatically improved HER activity over other MoS_2 based materials.

4.2 Computational and Experimental Details

4.2.1. Synthesis of single transition metal atoms doped 1T crystal phase monolayer MoS_2

Monolayer MoS_2 with 1T crystal phase (1T-MoS_2) can be prepared using the standard lithium intercalation method. Similar to the last chapter, 0.5 g of bulk MoS_2 powder was soaked in 4 mL of 1.6 M n-butyllithium/hexane under nitrogen atmosphere and gently mixed for 48 hours. Solid lithiated MoS_2 (Li_xMoS_2) was then isolated from vacuum filtration, followed by washing with hexane to remove excess n-butyllithium. It was then dried under vacuum for 24 hours. The dried product was then carefully immersed into 250 mL of water. The solution was placed into the sonication bath for 12 hours and then centrifuged at 5000 rpm for 15 minutes after. The supernatant collected was filtered using vacuum filtration, followed by washing with water. The exfoliated product was dried under vacuum for 24 hours. 3% TM (Co, Ni, Fe, Pd, Pt) solution was prepared using the following precursor solutions: $Co(CH_3CO_2)_2$, $Ni(CH_3CO_2)_2$, $Fe(NO_3)_3$, $PdCl_2$ and $HPtCl_4$ respectively. 0.9ml of the 3% TM solution was then mixed with 30 mL of colloid solution, which is made by dispersing 30 mg of $^{S}MoS_2$ and 0.5 mM thoiurea in 30 mL of Water/Isopropanol (1:3, v/v). The mixed solution was placed into the sonication tank (with a power output of 35W and an operating frequency at 37kHz) at room temperature for 24 hours to allow sonochemical reductive uptake of the metal precursors by radicals during high energetic sonication[19,20]. Afterwards, the precipitate was rinsed with deionized water and dried under vacuum to obtain the solid product.

4.2.2. Electrochemical Measurement

A three-electrode system controlled by μ-AUTOLAB III potentiostat (Eco-Chemie, Netherlands) was applied to carry out all electrochemical measurements. A platinum coil counter electrode and an Ag|AgCl ($1molL^{-1}KCl$) reference electrode were used in this

study. To prepare the working electrode, 4 mg of the electrocatalyst and 80μL of 5 wt% Nafion®117 solution will be dispersed in 1 mL of water/ethanol (4:1 v/v) and then followed by 30 min sonication to create a homogeneous ink. The ink was then drop-coated onto the surface of a glassy carbon electrode with a surface diameter of 3mm. All measurements were calibrated with respect to the reversible hydrogen electrode (RHE).

4.2.3. Density Functional Theory

We performed periodic, spin-polarized, planewave DFT total energy minimization calculations using the Vienna Ab Initio Simulation Package (VASP) version 5.4.1 [21,22] with the projector augmented wave (PAW) method [23,24] to model core ionic potentials and the functional of Perdew-Burke-Ernzerhof (PBE) for the exchange-correlation.[25] Our calculations used a 4 × 2 single nanosheet slab of 1T'-MoS_2 where a layer of 16 Mo atoms is sandwiched by two 16 S atom layers and all atoms were free to move. The lattice parameters of the 1T'-MoS_2 unit cell are optimized using an anisotropic volume expansion giving a = 3.18 Å and b = 6.56 Å, in good agreement with previous work.[26] Note a 4 × 4 unit cell is used for undistorted 1T-MoS_2 calculations where a = b = 3.18 Å. A vacuum region of approximately 17 Å was used to minimize periodic interactions in the z-direction. We used 5 × 5 × 1 and 4 × 4 × 1 Monkhorst-Pack k-point meshes to sample the Brillouin zone for 1T' and 1T, respectively. The planewave kinetic energy cutoff was set to 400 eV in all cases. To aid with convergence, we employed Gaussian smearing with a smearing width set to 0.05 eV. We ensured electronic self-consistency up to a tolerance of 10^{-6} eV and during ionic relaxation, we performed conjugate gradient minimization of the Hellmann-Feynman forces to within a tolerance of 10^{-2} eV·Å^{-1}. To locate transition states we utilized the dimer and climbing image NEB methods as implemented in VASP Transition State Tools version 3.1.[27–29] We confirmed that the transition states correspond to 1st order saddle points on the potential energy surface

through vibrational frequency analysis using finite displacements of 0.02 Å. The free energy change upon the adsorption of n hydrogen adatoms (ΔG_{nH*}) is computed from the adsorption energy of hydrogen (ΔE_{nH*}^{ads}) according to the following equations:

$$\Delta E_{nH*}^{ads} = E_{Tot}(slab + nH) - E_{Tot}(slab) - \frac{n}{2} E_{Tot}(H_2)$$

where $E_{Tot}(slab + nH)$, $E_{Tot}(slab)$ and $E_{Tot}(H_2)$ are the DFT total energies of H adsorbed on the 1T'-MoS_2 slab, the clean 1T'-MoS_2 slab and gas phase H_2;

$$\Delta G_{nH*} = \Delta E_{nH*}^{ads} + \Delta E_{ZPE} - T \cdot \Delta S_{nH*}$$

where ΔE_{ZPE} is the difference in the zero point energy of hydrogen in the adsorbed state and the gas phase, T is the temperature and ΔS_{nH*} is the entropy difference between adsorbed and gas phase hydrogen. The latter can be approximated as $\Delta S_{H*} \approx -\frac{1}{2} S_{H_2}^0$, where $S_{H_2}^0$ is the entropy of gaseous molecular hydrogen at standard conditions (298 K, 1 bar). Note that more negative values of ΔG_{nH*} correspond to more stable binding.

4.3 Structural Characterisation of 1T-TM-$^{S}MoS_2$

4.3.1. HR-STEM images with HAADF

Analysing the structure from HR-STEM with HAADF imaging the catalytic surface, we note the presence of a main octahedral structure (stacking in the 1T layer produces the ABC structure) which can be attributed to a monolayer 1T-$^{S}MoS_2$ (Figure 4.1 and 4.2). Occasionally, we can see a number of S vacancies on the surface presumably due to its creation by the butyl-lithium treatment. Notably, our "1T" MoS_2 nanosheets do not appear to be in pure polymorph as it is not currently possible to synthesise pure and stable 1T-$^{S}MoS_2$ using wet chemistry methods; 1T accounts for approximately *ca.* 76 % by surface area with the remainder of 2H polymorph (Figure 4.3).

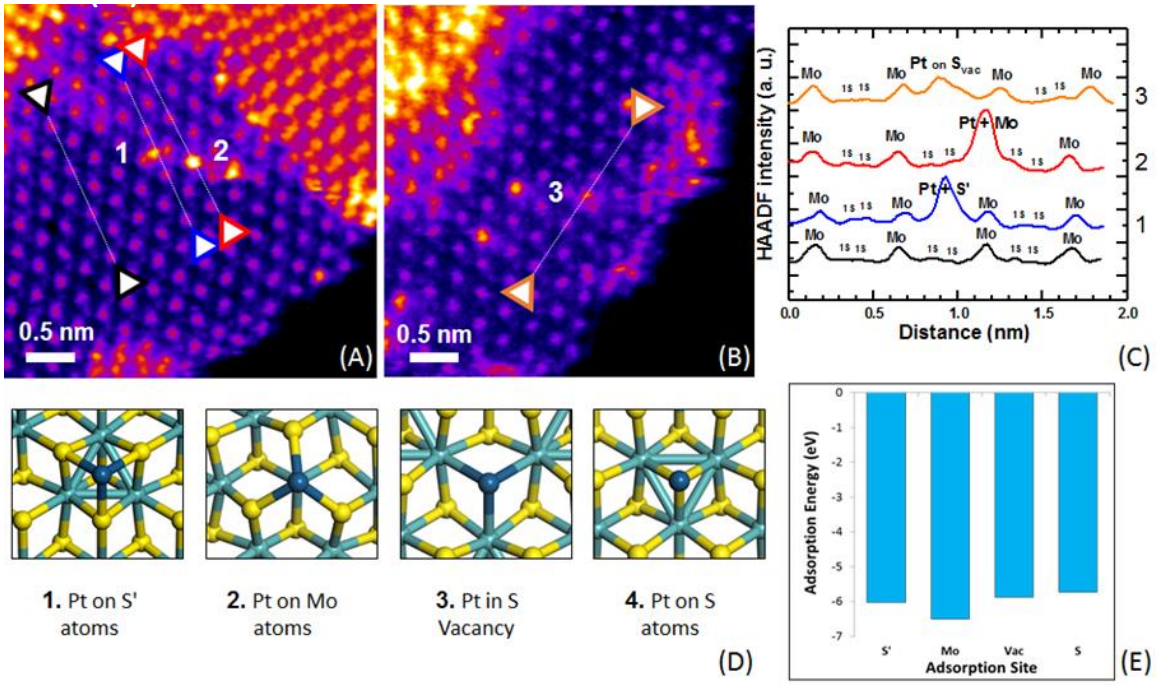


Figure 4.1. (a) and (b) HAADF-STEM of Pt-1T-$^{S}MoS_2$. (c) ADF intensity line profiles taken along the corresponding coloured line (Black, Blue, Red, and Orange) (<110> direction). (d) The simple representations of the Pt atom doping at position 1, 2 and 3 experimental observed on (A) and (B) and possibly at position 4. (e) Adsorption Energy for Pt on each adsorption site.

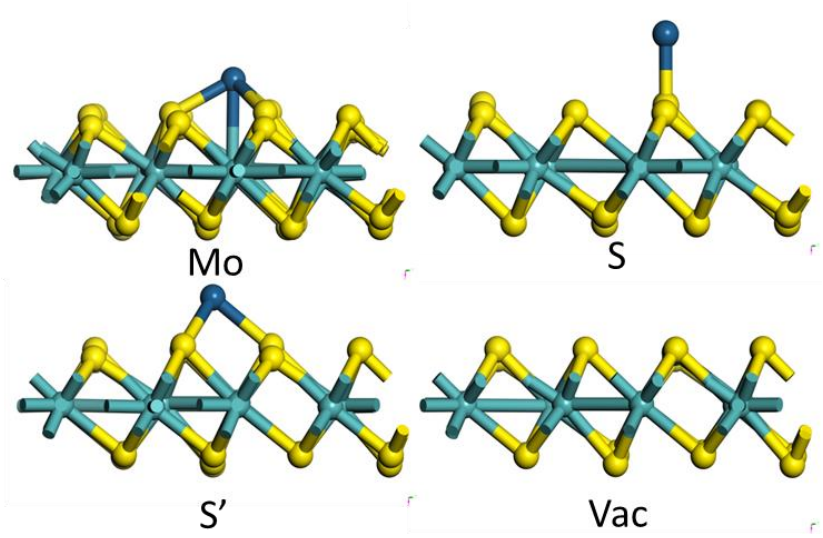


Figure 4.2. Side on views of DFT optimized structures of undistorted 1T-MoS_2 doped with a single atom of Pt in Mo top, S top, S' hollow and S vacancy sites.

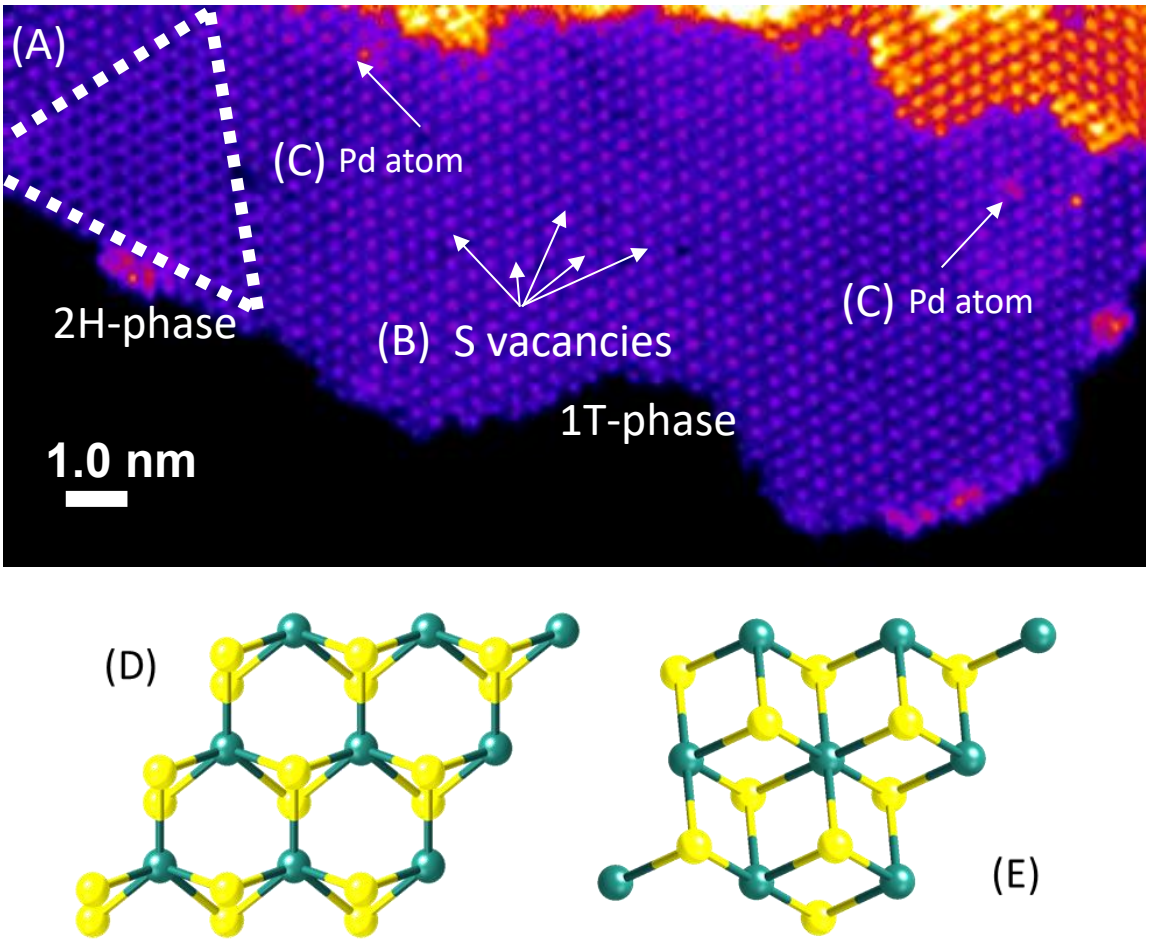


Figure 4.3. HAADF-STEM of Pd-1T-$^{S}MoS_2$ with feature (A) Area of MoS_2 with the 2H-phase (B) surface defect (S vacancies) (C) Pd atom dopant (D) 2H-MoS_2 model (E) 1T-MoS_2 model

This is consistent with the reported value in the literature[36]. The bright spots that can be seen on the 1T-$^{S}MoS_2$ surface correspond to Pt dopant atoms from the EELS. Notably these high intensity features are isolated, indicating the successful dispersion of single TM dopant atoms on the 1T basal plane. To further analyse the doping position of the transition metal atoms, intensity profiles of the ADF(Annular Dark-Field) image (Figure 4.1c) were taken in the <110> direction across the doped 1T'-$^{S}MoS_2$ surfaces (Figure 4.1a and b), where paths connecting coloured triangles correspond to the equivalently coloured lines in the intensity profile. We provide peak assignments in Figure 1c with the black line being a control path where only Mo and S atoms are present. Along this line we detect four mid-intensity peaks corresponding to Mo atoms with each being separated by two low-intensity S peaks.

Considering paths 1, 2 and 3 (blue, red and orange, respectively) (Figure 1a and Figure 1b), we note a bright feature in each image which corresponds to a single atom of Pt. The appearance of the bright features give rise to three unique intensity profiles (Figure 1c) indicating that there are three different and stable doping sites for Pt on 1T-$^{S}MoS_2$. Considering path 1 (blue), the HAADF intensity profile shows that the Pt atom is located in the middle of two Mo atoms and two S atoms. Indeed, relaxation of such a structure using DFT gives the structure in panel 1 of Figure 1d which has an adsorption energy of Pt relative to a gas phase isolated atom of -6.02 eV, with the Pt atom positioned slightly offset from above the S atom in the lower S layer, which we label as S'. HAADF intensity path 2 (red) has a high-intensity peak coincident with a Mo atom and can therefore be attributed to the presence of a Pt atom on top of a Mo site. This configuration is the most frequently observed dopant position in our imaging samples and also has the most stable Pt adsorption energy calculated by DFT of -6.51eV. According to the DFT

calculated structure of this configuration, the Pt atom is bonded closely to three S atoms (2.22 Å) and is slightly further from the underlying Mo atom (2.89 Å), which is in good agreement with our EXAFS results. Finally intensity profile 3 (orange) has a semi-bright feature and corresponding mid-intensity peak off-centred between two Mo atoms (Figure 1c). The peak is not as intense as we find on profiles 1 or 2, though more intense than Mo or S atom. Thus, we attribute this to a Pt atom doped at an S Vacancy site (surface defect site). We calculated the DFT adsorption energy of Pt in an S vacancy to be -5.88 eV, showing the strength of binding on this site is comparable to Pt on the S' site. Our calculations also suggested that one final doping site is possible where Pt resides on the S top site, though a notably less stable heat of adsorption (-5.73eV) precludes us from observing this experimentally (Figure 1d). A similar set of structural characterisations for Pd-1T-$^{S}MoS_2$ are presented in the Figures 4.3 and 4.4 which gives similar conclusions for Pd doping, though DFT calculations indicate a stronger preference for Pd adsorption at the Mo top site and S' site. (All detailed adsorption energies and distances to closest Mo atoms of Pd and Pt on 1T'-MoS_2 are listed in Table 4.1.) Overall, our STEM imaging results verified that we successfully dope isolated single metal atoms onto the 1T-$^{S}MoS_2$ basal plane without jeopardising the integrity of the 1T phase such that it may reconstruct to the more stable 2H phase.

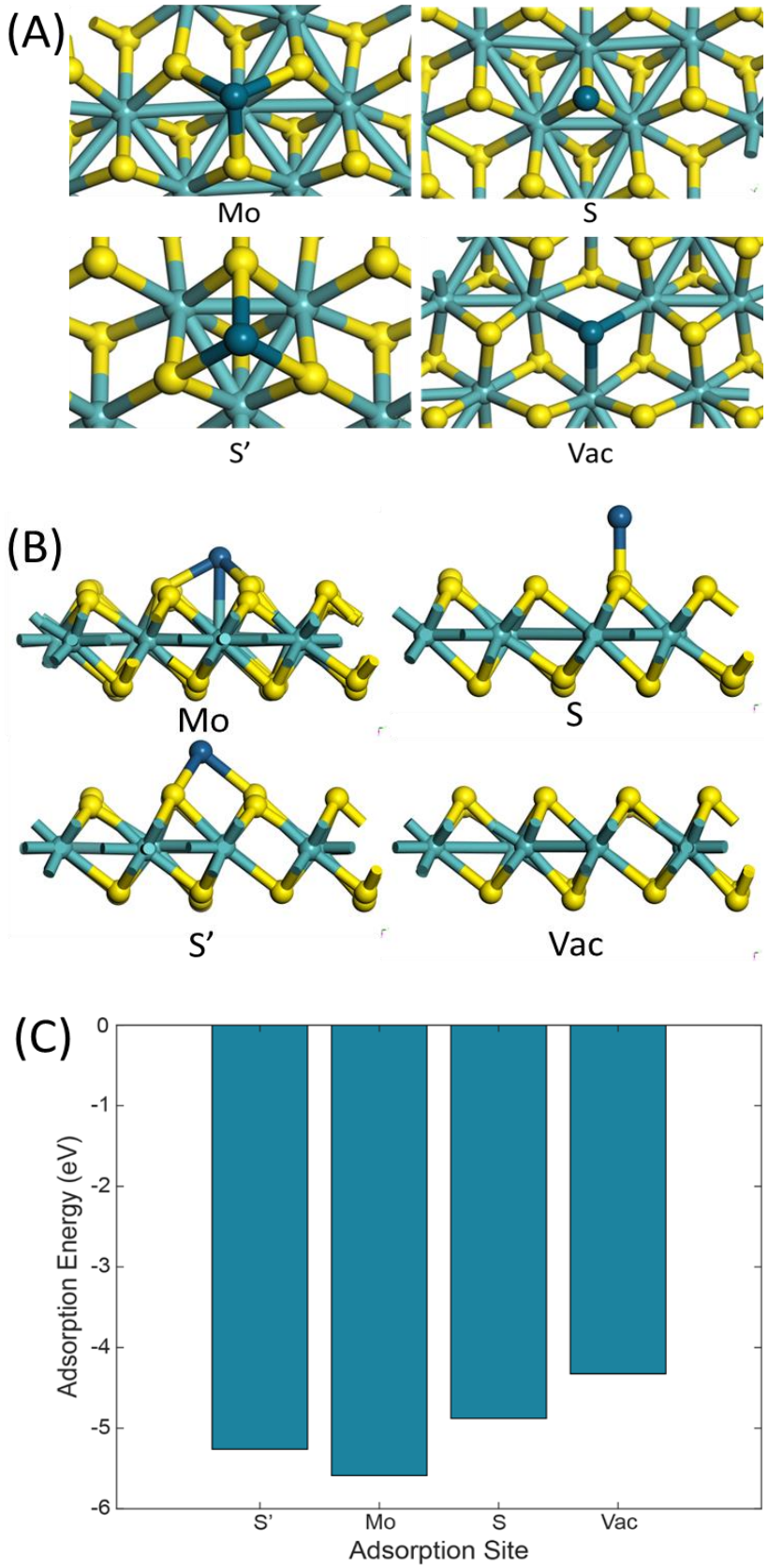


Figure 4.4 (A) Top View and (B) Side View of the four different adsorption sites for Pd on undistorted 1T-$^{S}MoS_2$ and (C) their corresponding adsorption energies calculated by DFT. For undistorted 1T-$^{S}MoS_2$ we use a 4 × 4 unit cell of octahedral 1T with lattice parameters of a = b = 3.18 Å and equivalent computational settings to all other simulations.

Table 4.1. Adsorption energies and distances to closest Mo atoms of Pd and Pt on 1T'-MoS_2.

MoS_2 Polymorph	Dopant	Site	Adsorption Energy (eV)	Mo to TM distance (Å)
1T	Pd	Mo	-5.59	3.00
		S	-4.88	4.25
		S'	-5.26	3.61
		Vac	-4.33	2.71
	Pt	Mo	-6.51	2.91
		S	-5.73	2.08
		S'	-6.02	3.54
		Vac	-5.88	2.61
1T'	Pd	Mo_1	-2.91	2.90
		Mo_2	-2.53	2.84
	Pt	Mo_1	-3.86	2.82
		Mo_2	-3.33	2.74

4.3.2. Chemical Environment of Pt and Pd adatoms

4.3.2.1. XPS analysis

XPS was used to analyse the surface composition of Pt dopants on Pt-1T-$^{S}MoS_2$ (Figure 4.5). We were able to detect the presence of isolated Pt on 1T-$^{S}MoS_2$ with a surface coverage of ca. 2.77% on the MoS_2. This metal content is significantly lower than that of 20% Pt/C commonly used as the benchmark for HER (Table 4.2). Despite the use of room temperature, the Pt 4f XPS spectrum showed that most of the Pt are detected as metal Pt(0) or Pt^{2+} ions, which indicates that Pt(0) atoms were radically reduced from its $HPtCl_4$ precursor and dispersed onto the basal surface during the high energetic sonication process.

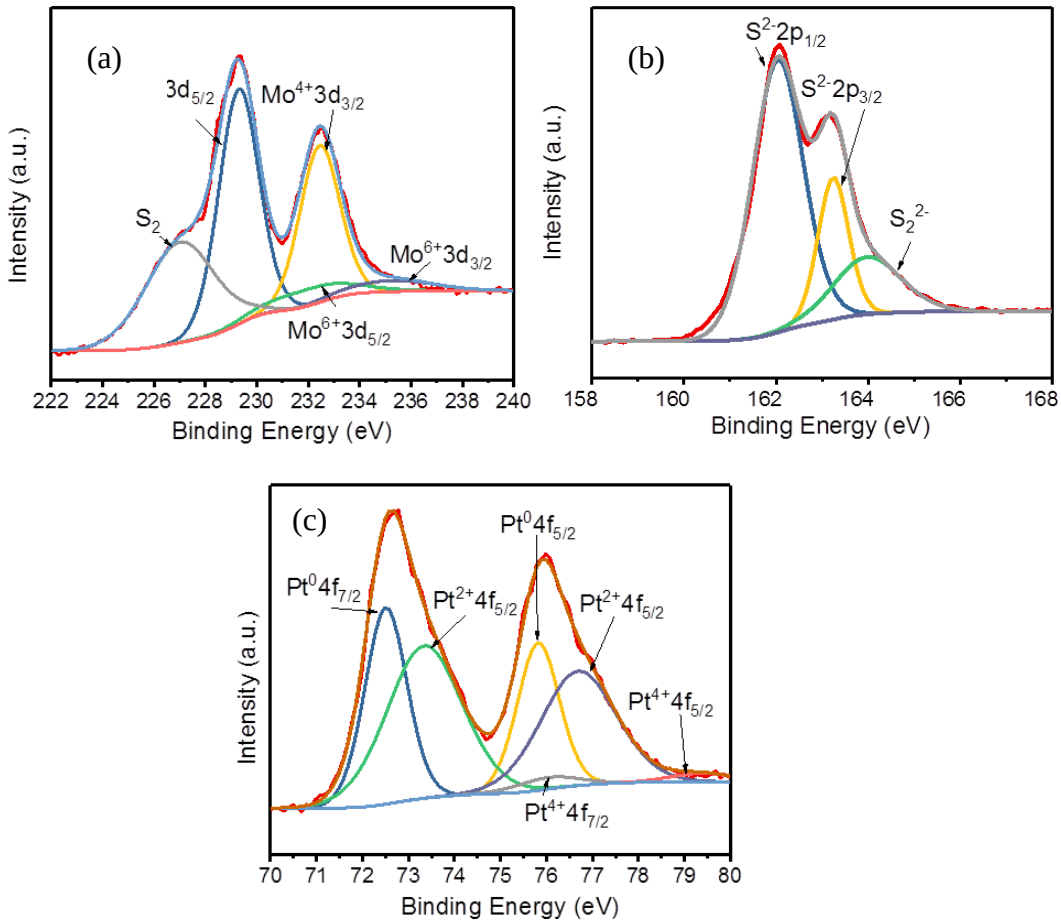


Figure 4.5 XPS Spectra of Pt-1T-$^{S}MoS_2$ (a) Mo 3d (b) S2p (c) Pt 4f

Table 4.2. General XPS assessment of Pt-1T-MoS_2

Name	Start BE	Peak BE	End BE	Height CPS	FWHM (eV)	Area (P) CPS.eV	Area (N) TPP-2M	Atomic %	Atomic %
S2p	173.08	163.43	155.08	132573	3.52	538216.43	3725.22	35.1	72.9
Mo3d	240.08	229.25	220.08	162816	4.24	1049157.79	1290.69	12.16	25.01
C1s	293.58	284.95	281.08	87990.0	2.74	280487.75	3933.48	37.06	
O1s	540.58	532.44	527.08	69971.5	3.25	261859.97	1519.75	14.32	
Pt4f	81.58	73.43	68.08	35683.5	2.33	195315.22	144.87	1.36	2.77

4.3.2.2. XAS Adsorption Analysis

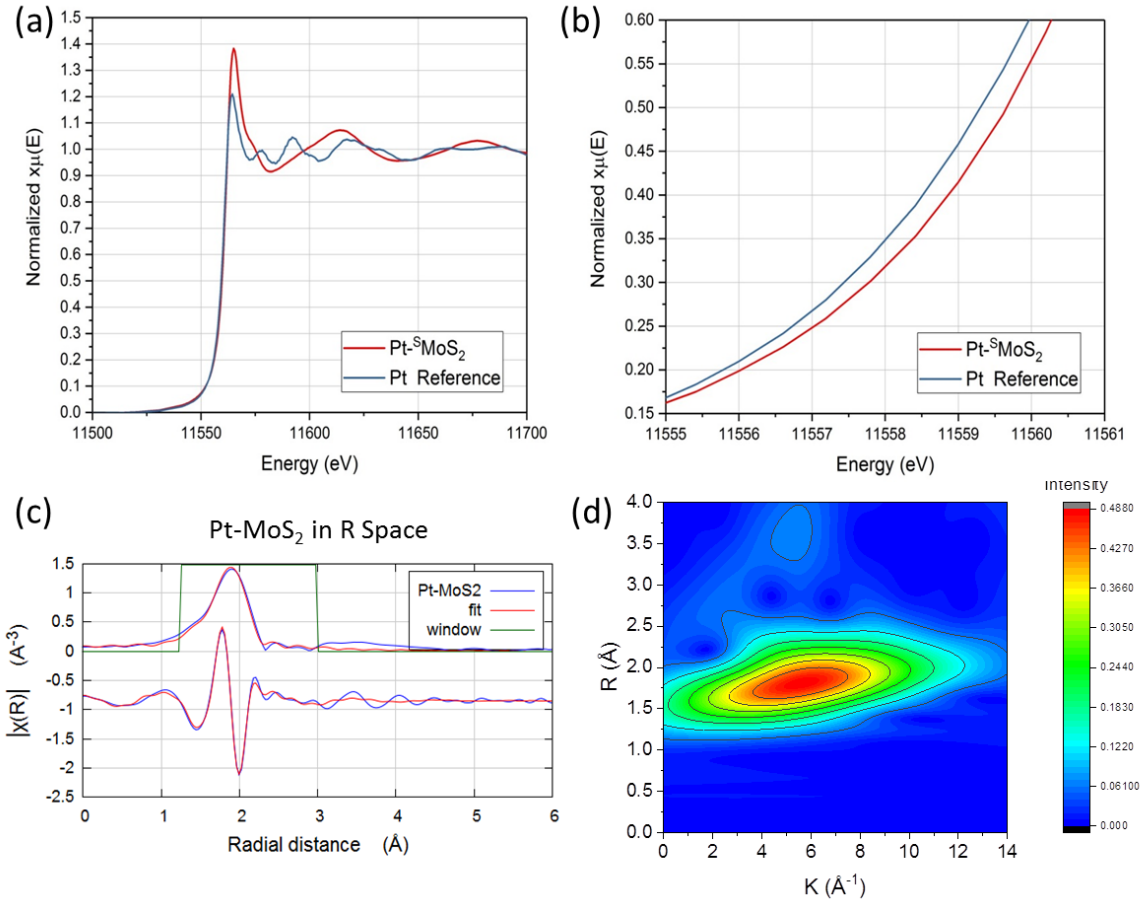


Figure 4.6. XAS Adsorption Analysis of Pt-1T-$^{S}MoS_2$. The Pt K-edge XANES spectra of Pt-1T-SMoS2 and the Pt (0) foil reference. (b) Enlarged version of A for the Pt K-edge region with energy range from 11555eV to 11561eV. (c) Fourier transforms of k3-weighted Pt K-edge of Extended X-ray absorption fine structure spectroscopy (EXAFS) spectra of Pt-SMoS2 and corresponding. (d) Morlet Wavelet transform analysis (Long Range) (Kappa = 8, Sigma = 1, R = 0 to 4 Å).

As seen from Figure 4.6, the chemical environment of single Pt atoms dispersed on the 1T-$^{S}MoS_2$ surface is also analysed by XAS (X-Ray Absorption Spectroscopy) such as XANES and EXAFS. The white line (absorption edge line) intensity of the Pt L3 edge in Pt K-edge XANES spectra refers to the dipole allowed electronic transition from 2p to 5d state. (Figure 4.6a and b) Since the shape of the absorption edge depends greatly on the coordination environment, the XANES spectra for the Pt reference, which bears a FCC structure, will be different to that of the highly dispersed Pt-1T-$^{S}MoS_2$ structure. (Figure 4.6a and Figure 4.6b) Nevertheless, Pt K-edge absorption positions of Pt-1T-$^{S}MoS_2$ are still close to that of Pt (0) foil reference, which suggested the possibility of the presence

of Pt(0) species. The presence of higher Pt oxidation state is also evidenced by the higher binding energy with reference to the Pt (0) as a stronger transition that gives the white line a higher intensity. Using the Pt(0), Pt(II) and Pt(IV) reference[30] for comparison, we are able to estimate the average oxidation state of Pt on the Pt-1T-$^{S}MoS_2$ to be less than 2, as the white line of the catalysis lies in between that of Pt(0) and Pt(II) (Figure 4.7a) This is further confirmed with linear combination fitting technique, which we found that Pt-1T-$^{S}MoS_2$ is composed of approximately 85% Pt(0) and 15% Pt(II).

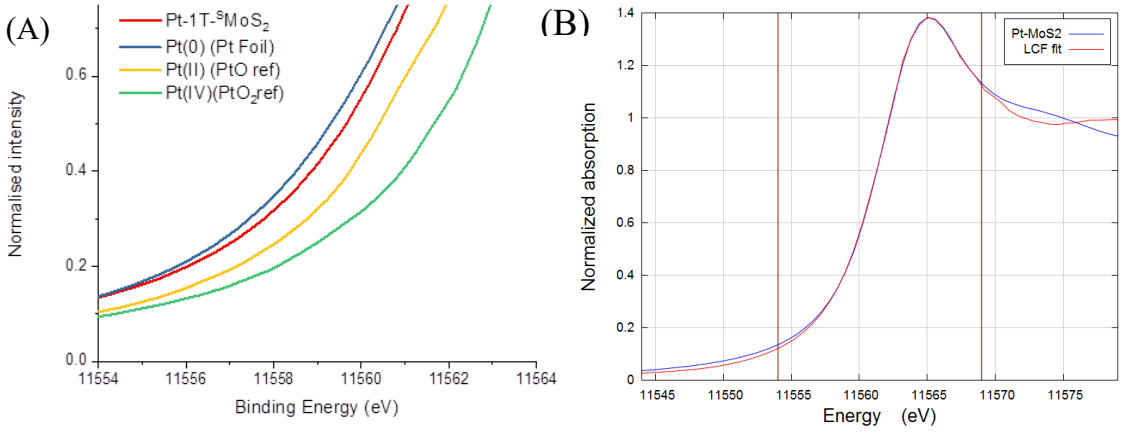


Figure 4.7. Estimation of Oxidation State by XANES. (a) Pt(II) (PtO) and Pt(IV) (PtO_2) XANES reference obtained from the literature[30] and the Pt(0) foil XANES reference are used to compare with that of our Pt-1T-^{S}MoS2 catalysis. (b) Linear Combination Fitting (LCF fit) of Pt-MoS2 with respect to Pt(0) and Pt(II) references.

A first shell of Pt-S contribution {Bond length (Å) = 2.31 ± 0.01, Coordination number =4.2 ± 0.2, Energy difference (eV) =7.4, Debye-Waller Factor =0.006 ± 0.001} is derived from Figure 4.6c. The absence of Pt-Pt interaction indicates that most Pt species on the basal plane of MoS_2 are not metal clusters or nanoparticles but rather single atoms or ions. If clusters nanoparticles are accumulated at the surface, the coordination number of Pt-S will be much higher the value found (4.2 ± 0.2) as well. Furthermore, since only around 3% of Pt was doped onto the MoS_2, Pt atoms are unlikely to be intercalated in between layers as intercalated Pt atoms in this case will be octahedral coordinated to surrounding S. The result agrees with the STEM-EELS results shown in Figure 4.1. No strong Pt-Mo contribution can be found according to the fitting. This indicates that Pt is

not strongly bound to Mo at the lattice but rather to the neighbouring S atoms. This is similar to our previous findings on the chemical environment of transition metal dopants on 2H-$^{S}MoS_2$ basal sites[1]. We also conducted the Wavelet transform (WT) analysis to separate backscattering atoms and provide a higher distance resolution and the resolution in the K-space of Pt K-edge (Figure 2d and Figure S5 for high resolution WT analysis). Only one WT intensity maximum at around 3.75 to 7.5 $Å^{-1}$ arising from the light atom coordinator can be well resolved from 0 to 4.0 Å, whereas the intensity maximum associated with the Pt-Pt coordination at 8.5 $Å^{-1}$ cannot be detected for Pt-1T-$^{S}MoS_2$. This once again reinforces the evidence that metallic Pt-Pt clusters are absent on the surface. (A similar EXAFS for Pd-1T-$^{S}MoS_2$ are presented in figures 4.8 as extra information which gives same conclusions for Pd doping. No Pd clusters can be observed due to the absence of Pd-Pd bond.)

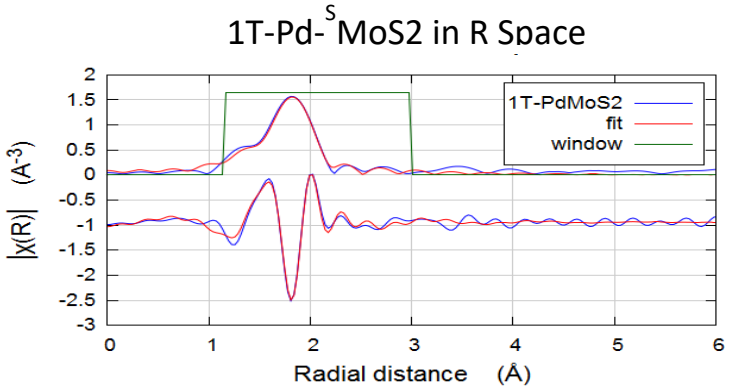


Figure 4.8 XAS Adsorption Analysis of Pd-1T-$^{S}MoS_2$. (a) Fourier transforms of k3-weighted Pt K-edge of Extended X-ray absorption fine structure spectroscopy (EXAFS) spectra of Pd-$^{S}MoS_2$ {Bond length (Å) = 2.33 ± 0.01, Coordination number =4.6 ± 0.2, Energy difference (eV) =7.4, Debye-Waller Factor =0.003 ± 0.001}

4.4 Electrochemical analysis for HER

4.4.1. Electrocatalytic Performance and Stability of Catalyst

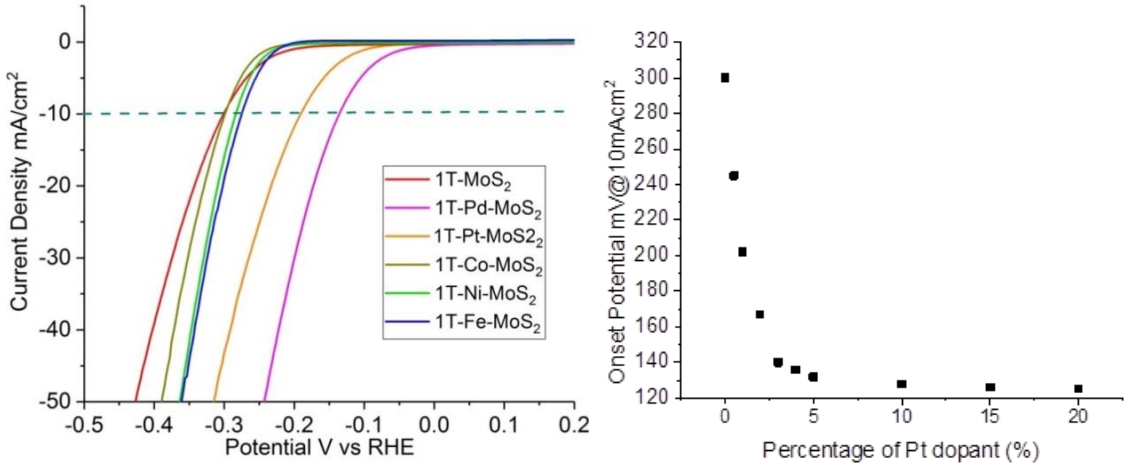


Figure 4.9 Electrochemical testing of TM-1T-$^{S}MoS_2$ (a) LSV of TM-1T-MoS_2 (TM= Fe, Ni, Co, Pt, Pd) (b) Onset potential of Pt-1T-SMoS2 at different Pt doping concentration (Both at a scan rate of 50 mVs^{-1})

An electrochemical screening test using linear sweep voltammogram (LSV) for HER was conducted with five different transition metal elements (3 wt% TM= Fe, Ni, Co, Pt, Pd) chosen as dopant atoms on 1T-$^{S}MoS_2$ using the same preparation method (Figure 4.9a). Fe, Ni, Co doped 1T-MoS_2 all shows only slight improvement in terms of catalytic activity. However, both Pd-1T-$^{S}MoS_2$ and Pt-1T-$^{S}MoS_2$ exhibit significantly smaller onset potentials (at a current density of -10mA/cm^2) of approximately -140mV and -223mV, respectively, when comparing to that of the pristine 1T-$^{S}MoS_2$ (-300mV). This suggests that the incorporation of single Pd and Pt atoms at 3 wt% with such simple doping technique can successfully increase the HER performance significantly as compared to undoped 1T-$^{S}MoS_2$. We have also attempted to optimise the catalytic activity by synthesising Pt-1T-$^{S}MoS_2$ at different doping concentrations (from 0.5 to 20%). HER activity increases when the doping concentration increases from 0.5% to around 3%. This is expected as more Pt/Pd active sites are available for recombination. However, the increase starts to slow down drastically when approaching 3% and remains nearly constant as the dopant concentration increases beyond this. This is possibly due to

aggregation of Pt and Pd atoms into nanoparticles and clusters. While these nanoparticles can help hydrogen production, they at the same time block the 1T adsorption sites of MoS_2. 3% TM doping is picked to minimise the use of metal content and ensure that there will be no aggregations, as confirmed by XAS analysis in the previous section.

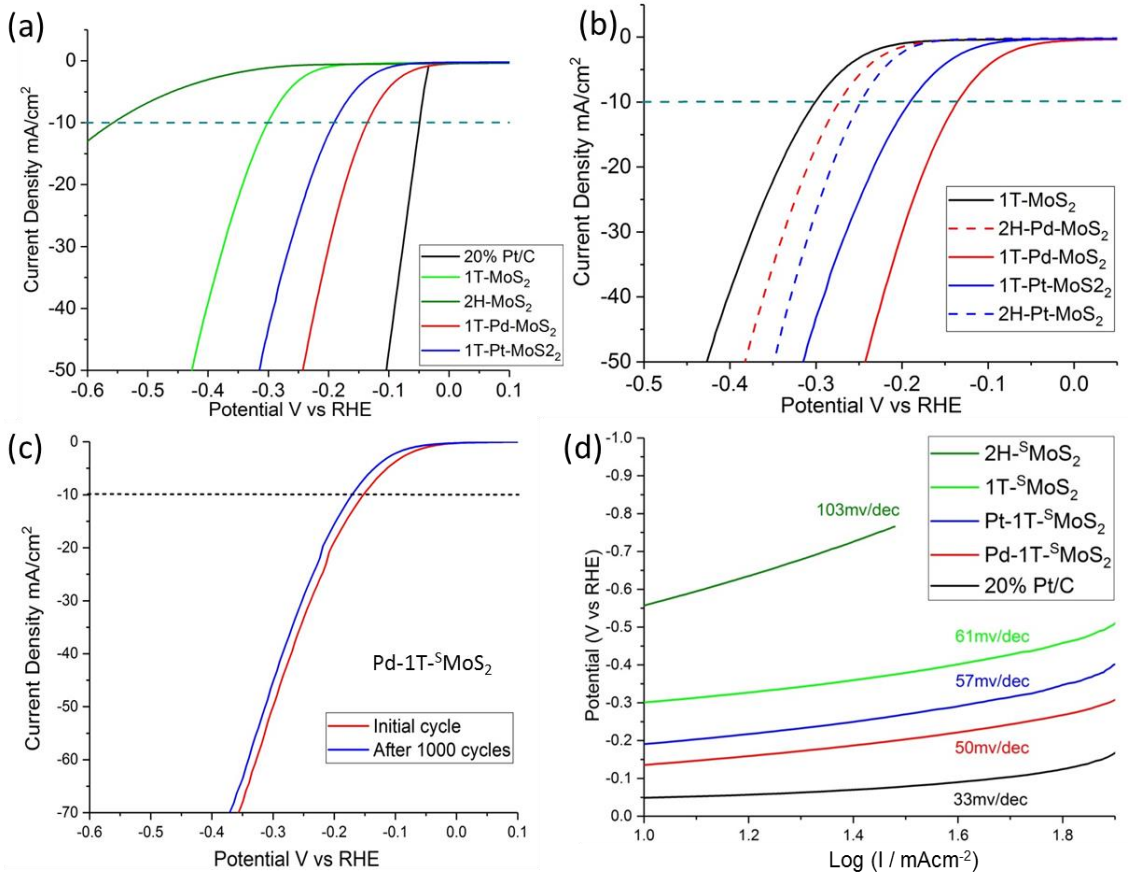


Figure 4.10 Electrochemical testing of Pt-1T-$^{S}MoS_2$ and Pd-1T-$^{S}MoS_2$. (a) LSV of Pd-1T-$^{S}MoS_2$, Pt-1T-$^{S}MoS_2$, 1T-$^{S}MoS_2$ and 2H-$^{S}MoS_2$ nanosheets and the reference 20% Pt/C in 0.5M H_2SO_4 at a scan rate of 50 mVs^{-1}. (b) LSV of 1T-Pd-$^{S}MoS_2$, 2H-Pd-$^{S}MoS_2$ (c) Stability measurement of Pd-1T-$^{S}MoS_2$ for HER, before and after 1000 cycles. (d) Tafel Analysis of Pt-1T-$^{S}MoS_2$ and Pd-1T-$^{S}MoS_2$

As far as we are aware the range of these onset potentials TM-1T-$^{S}MoS_2$ is comparable to those of TM-N-doped graphene, the most promising alternative to Pt/C.[5] Moreover, we also compare the LSV results to that of the 2H phase and show that Pd-1T-$^{S}MoS_2$ has an onset potential that is 200 mV smaller than that of Pd-2H-$^{S}MoS_2$; this comes as no surprise since pristine 2H-$^{S}MoS_2$ is a semiconductor and therefore exhibits poor charge transport that inhibits HER performance (Figure 4.10b). We also examine the durability

of Pd-1T-$^{S}MoS_2$ for HER using cyclic voltammetry. We show there is a marginal increase in onset potential of 10 mV after 1000 cyclic voltammetry cycles. This confirms that the single transition metal atoms are firmly attached on the surface and the 1T phase is not converted back to 2H phase during the electrochemical reaction. (Figure 4.10c)

4.4.2. Tafel Analysis of TM-1T-$^{S}MoS_2$

We then performed Tafel analysis to study the electrochemical kinetics of the HER as catalysed by each TM-1T-$^{S}MoS_2$ sample (Figure 3d) and compared that with results from 2H-$^{S}MoS_2$ as well as 20 % Pt/C. Measurements and analysis using the reference 20% Pt/C catalyst gave a Tafel slope of 33 mV/dec, which is similar to previous results obtained elsewhere.[31,32] At low overpotential, it is widely accepted that a Tafel slope of 30 mV/dec is indicative of HER that proceeds via the Tafel pathway. This mechanism depicts the ready reduction of H^+ on the metal surface giving a high coverage of H. Thus, the rate for HER is limited by H-H recombination to form H_2. [32] In contrast, we have found that 2H-$^{S}MoS_2$ gives a Tafel slope of 103 mV/dec, indicating that the kinetics for H_2 formation is limited by the first Volmer proton reduction step before sufficiently H surface coverage for recombination is achieved. From the results of Tafel analysis on TM-1T-$^{S}MoS_2$ (Figure 3d), Pd-1T-$^{S}MoS_2$ and Pt-1T-$^{S}MoS_2$ have Tafel slopes of 50 and 57 mV/dec, respectively which are slightly smaller compared to that of pristine 1T-$^{S}MoS_2$ (61 mV/dec). Given the *ca.* 24% inclusion of 1T-$^{S}MoS_2$ with 2H- $^{S}MoS_2$ as shown in Figure 4.3a, it is clear that the rate limiting for H_2 formation over the 1T-$^{S}MoS_2$ based catalysts is likely to be on the Tafel step and the presence of TM can further reduce this kinetic barrier.

4.5 HER Mechanism of 1T-$^{S}MoS_2$

4.5.1. Adsorption of H on 1T-$^{S}MoS_2$

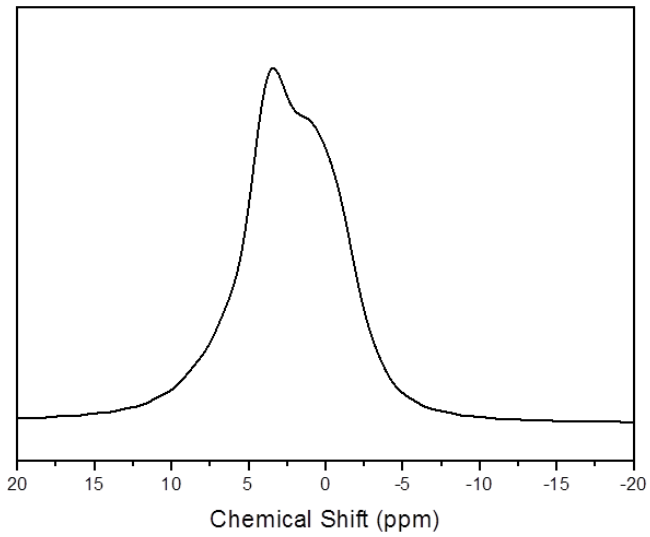


Figure 4.11 1H-SSNMR of 1T-$^{S}MoS_2$

In order to ensure that the 1T-$^{S}MoS_2$ does not suffer from the limited H on its surface as that of 2H-$^{S}MoS_2$, we have measured the H coverage over dried 1T-$^{S}MoS_2$ quenched after HER catalysis with solid-state proton nuclear magnetic resonance (1H-SSNMR). As shown from Figure 4.11, the strong but broad signal of ^{1}H indicative higher H coverage of 1T-$^{S}MoS_2$ can be clearly seen. A series of Density Functional Theory (DFT) calculations are then performed to study the adsorption and recombination of H adatoms on 1T-$^{S}MoS_2$. The simulation are performed on the distorted 1T'-$^{S}MoS_2$ monolayer that is a dynamically stable 2 × 1 reconstruction of 1T-$^{S}MoS_2$. The 1T phase is destabilised by H* adsorption and as a result exists as 1T' under HER conditions[12–15] (Figure 4.12). The morphology of the 1T' surface results in two distinct S adsorption sites that are tensile or compressive strained as a result of Mo-Mo clustering in the reconstruction. Note that in our discussion we do not explicitly distinguish the two phases here through use "1T" to refer to both. We also note that we do not explicitly account for the aqueous solvent in our calculations due to significant computational cost, though instead perform gas phase

simulations with H/H_2 only. While these DFT calculations will allow us to compute free energies of adsorption with respect to H_2 (g) as well as the Tafel barrier, it cannot be used to quantify the barrier for the Volmer or Heyrovsky steps due to artificially introducing changes in the electrostatic potential along the reaction coordinates of these steps. However, given our experimental Tafel analysis suggests that the rate limiting step for HER on TM-1T-$^{S}MoS_2$ is the recombinative desorption of $H_{2\,(g)}$, our calculations should be sufficient to draw some useful conclusions. Here in Table 4.3, the simulation concludes that majority of this signal comes from ^{1}H on compressively strained S site and tensile strained S sites with different number of H attachments, which confers the same conclusion as the experimental NMR result that there are the higher surface H coverage.

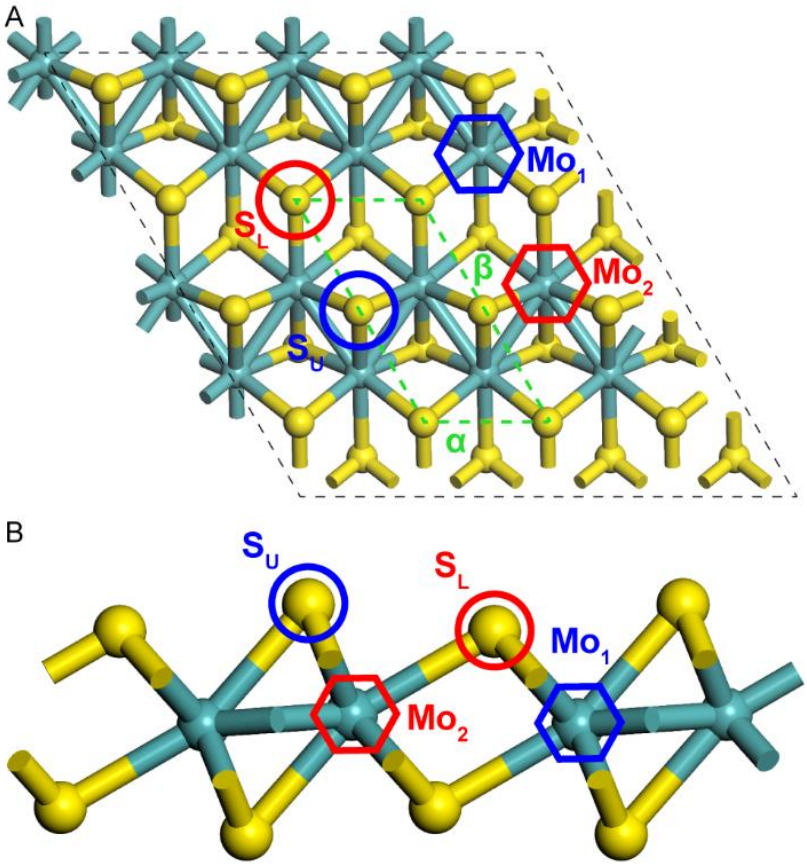


Figure 4.12. Top-down (A) and side-on (B) views of the (4 × 2) 1T'-MoS_2 slab used in DFT calculations. The 1T' unit cell is marked by the green dashed box and lattice parameters α and β are labelled. The 1T'-MoS_2 has two distinct S sites characterised by a compressively strained S in the upper position (S_u) and a tensile strained S in the lower position (S_L). There are also two distinct Mo sites where an Mo is either bound to 1 top layer S_u atom and 2 top layer S_L atoms (Mo_1) or 2 top layer S_u atoms and 1 top layer S_L atom (Mo_2).

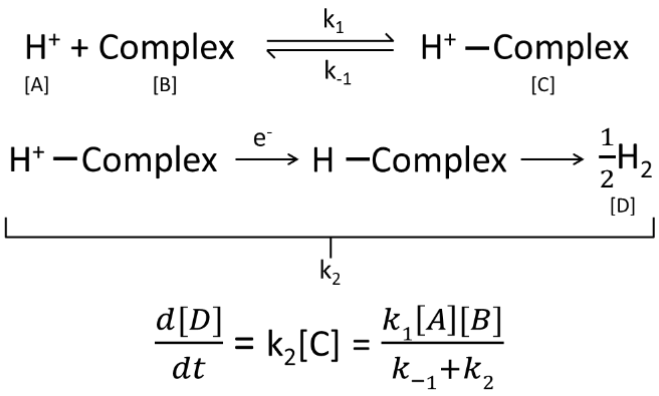
Table 4.3. Simulation of ^{1}H NMR signals shown by 1T'-MoS_2*

Surface	Site(s)	Coverage (%)	Number of H* (n)	ΔE_{nH*}^{ads} (eV)	E_{ZPE} (eV)	ΔG_{nH*} (eV)	Ave. δ (ppm) no G=0 (G=0)
1T'-MoS_2	S_u	6.25	1	0.56	0.21	0.84	7.47 (5.25)
	S_L	6.25	1	-0.11	0.23	0.19	-1.27 (-4.10)
	S_L × 2	12.50	2	-0.01	0.46	0.44	0.30 (-2.58)
	S_L × 3	18.75	3	-0.08	0.68	0.81	1.54 (-2.12)
	S_L × 4	25.00	4	0.21	0.90	1.38	5.67(1.88)
	S_L × 5	31.25	5	0.31	1.12	1.78	4.50 (0.34)
	S_L × 6	37.50	6	0.64	1.34	2.38	2.26(-2.22)

*Adsorption energiesΔE_{nH*}^{ads}, zero point energies E_{ZPE} and free energies of adsorption ΔG_{nH*} for H on S_u and S_L sites of 1T'-MoS_2 as well as that for the lowest energy configurations of n H adatoms (n = 2, 3, 4, 5, 6). Chemical shift values (δ) are calculated using the tensor of Mason[33] as implemented in the VASP code. All δ are relative to tetramethlsilane (TMS). For configurations with multiple H adatoms, values given are averaged from all H present. Two values are given for chemical shifts excluding and including (bracketed) G=0 contributions.

4.5.2. Recombination of H* on 1T-$^{S}MoS_2$

The rate determining step is likely to be recombination of adsorbed H to H_2, where high coverage of surface H in equilibrium with H^+ from the solution is established. As a result, steady state approximation can be adopted to analyse the kinetic parameters of the HER over the 1T-$^{S}MoS_2$. By assuming the rate of change of the intermediate concentration (H adsorbed 1T-$^{S}MoS_2$) is constant throughout the reaction, the overall HER reaction rate can be found by Equation 4.1. Electrochemical chronoamperometry of 1T-MoS_2 at different concentrations of the electrolyte (H_2SO_4) were conducted at -0.5 V for an hour to measure the average charge consumed for hydrogen evolution per minute. Using the Faraday's law of electrolysis (HER rate = $\frac{Q}{Faraday\ constant*2}$), we can roughly estimate the rate of hydrogen production. From our result, the production rate of hydrogen gas has a linear relationship with the number of free protons available to be adsorbed in the range of 0.4 M to 1.2 M of H_2SO_4 (Figure 4.13). The overall rate law shows that the production rate of hydrogen indeed shows a rough linear relationship with [H^+] concentration within experimental error, as stated in Equation 4.1.



Equation 4.1: Steady State Approximation of the hydrogen evolution reaction. 'Complex' refers to 1T-MoS_2 in this case.

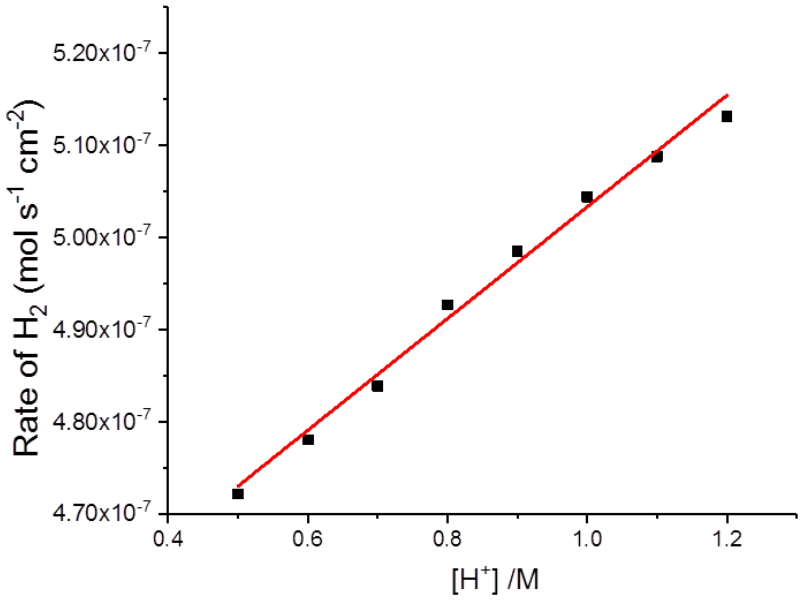


Figure 4.13. A plot of hydrogen production rate against the concentration of H^+ in the electrolyte

Considering the adsorption of H* on pure 1T, we find the most stable adsorption is on a tensile-strained S atom top site where ΔG(H*) is +0.19eV (Table 4.3); this compares well with values reported elsewhere[15]. This value is significantly lower than those reported over 2H structure in the last chapter. Thus our calculations suggest that the adsorption of H* on 1T-$^{S}MoS_2$ is close to thermoneutral and is significantly more so than 2H-$^{S}MoS_2$, hence the superior HER activity of the former. Co-adsorption of two H* adatoms on adjacent tensile-strained S atoms serves as the initial state for the Tafel H-H

recombination step (Figure 4.14). The total free energy of adsorption for two H* adatoms in this configuration is 0.44eV, corresponding to a 0.25eV repulsive interaction to overcome from having 2 H* adatoms at infinite separation. (Table 4.3) The activation barrier to form H_2 (g) from initial state is calculated to be 1.15 eV (or 1.40 eV from infinite separation), with the reaction from infinite separation being near ergodic. This barrier is in good agreement with that computed previously by others and is sufficiently large to inhibit fast recombinative kinetics[15]. This further corroborates our suppositions based on our experimental Tafel and kinetic analyses.

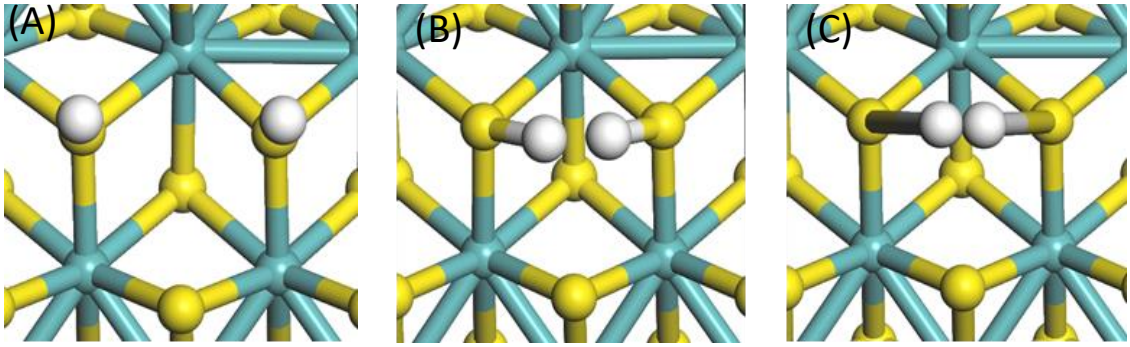


Figure 2.14 (a) Initial state (b) transition State (c) final State of Tafel recombination step of H* on 1T-$^{S}MoS_2$

4.6 HER Mechanism of TM- doped 1T-$^{S}MoS_2$

4.6.1. Adsorption of H on TM- doped 1T-$^{S}MoS_2$

Turning attention to the Pt and Pd-doped 1T-$^{S}MoS_2$ basal plane, we consider both the undistorted and distorted surfaces. In our HAADF-STEM imaging, it is clearly seen that the pure surface has hexagonal symmetry and therefore corresponds to the undistorted 1T-$^{S}MoS_2$ (Figure 4.1). However, it may be converted to distorted 1T'-$^{S}MoS_2$ upon metal doping. Interestingly, upon reconstruction of the 1T'-$^{S}MoS_2$ monolayer, both Pt and Pd can interact to the underneath Mo site (TM bonding to Mo on the second layer) with attempts to relax these atoms at other high symmetry sites (e.g. S top and S') resulting in displacement back to a Mo site. (Figure 4.15) The reduction in surface symmetry of the 1T'-$^{S}MoS_2$ phase up H* induced distortion gives rise to two different Mo top sites depending whether the TM is bound to one compressive-strained S atom and two tensile-strained S atoms (Mo top site 1) or two compressive-strained S atoms and one tensile-strained S atom (Mo top site 2) (Figure 4.16 and Figure 4.17). For both Pt and Pd adsorption, the binding is notably stronger on Mo top site 1 whereby two bonds are formed with tensile-strained S atoms and one with the compressive-strained S atom. (Table 4.4)

Using the most stable Pt- and Pd-doped 1T'-$^{S}MoS_2$ surfaces (Mo top site 1), we computed the free energy of adsorption for H* on various sites types as well as the minimum energy pathway for Tafel H-H recombination thereon. Our calculated adsorption energies show that the most stable site for H* binding proximal to TM on TM-1T'-$^{S}MoS_2$ is directly adsorbed to the Pt or Pd atom, with the H atom tilted away from the TM and between two tensile-strained S atoms (Figure 4.18). The $\Delta G(H^*)$ for this configuration on Pt- and Pd-doped 1T'-$^{S}MoS_2$ are -0.20 eV and +0.49 eV, respectively.

(Table 4.5 and 4.6) We found that H* adsorption to the transition metal dopant atoms is less thermoneutral than the corresponding value calculated for the undoped 1T'-$^{S}MoS_2$ monolayer (+0.19 eV), despite these materials exhibiting superior HER activity. Our work on transition metal doped 2H-$^{S}MoS_2$, as well as similar findings from others, have suggested that S atoms proximal to TM become activated for HER thanks to more thermoneutral H* adsorption.[1,17] However, our calculations show that S atoms proximal to the Pt and Pd dopant bind H* less strongly with ΔG(H*) of +0.73 eV and +0.71 eV, respectively; in both cases the adsorption of H* is less stable and notably further from thermoneutrality than that directly at the dopant site.

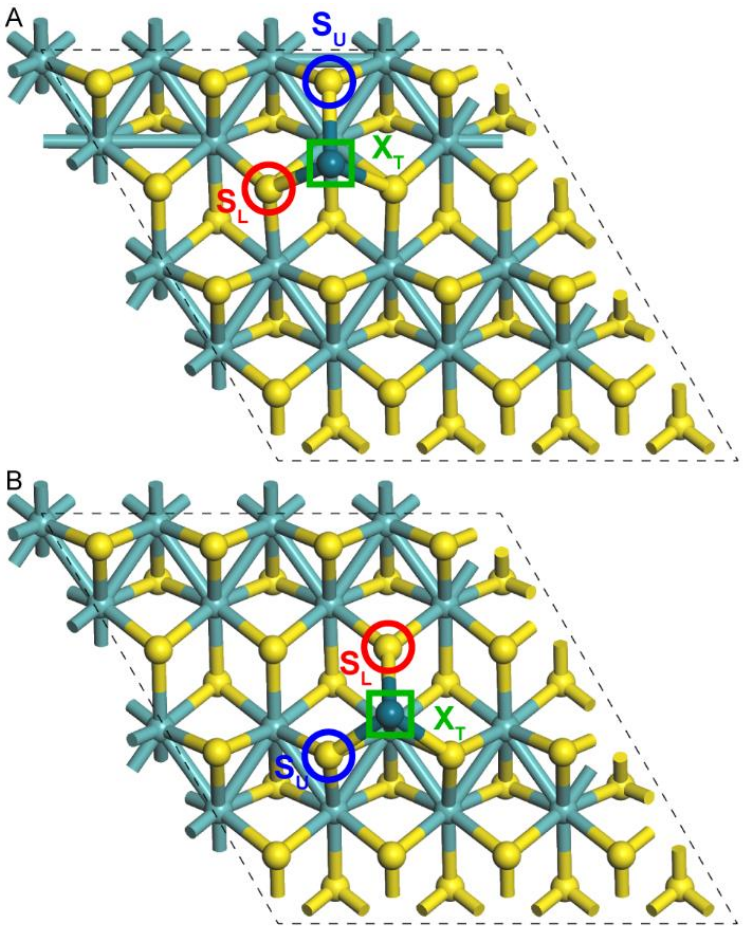


Figure 4.15 Top-down views of the DFT unit cell for a dopant atom X bound in either the Mo_1 (A) or Mo_2 (B) positions. Adsorption sites proximal to the dopant atom are labelled where X_T is the dopant atom top site, S_u is an upper S site directly bound to the X atom and S_L is a lower S site directly bound to the X atom.

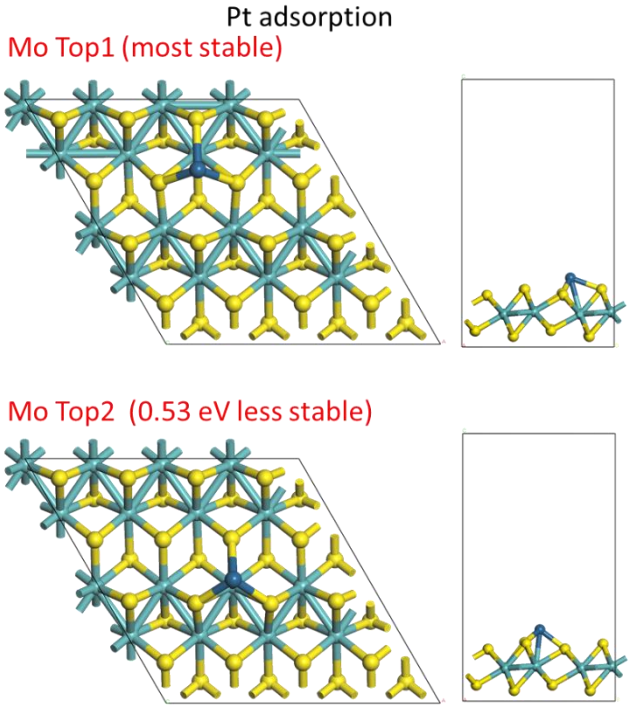


Figure 4.16 Computational simulation of Pt doped at Mo top1 and Mo top 2 sites

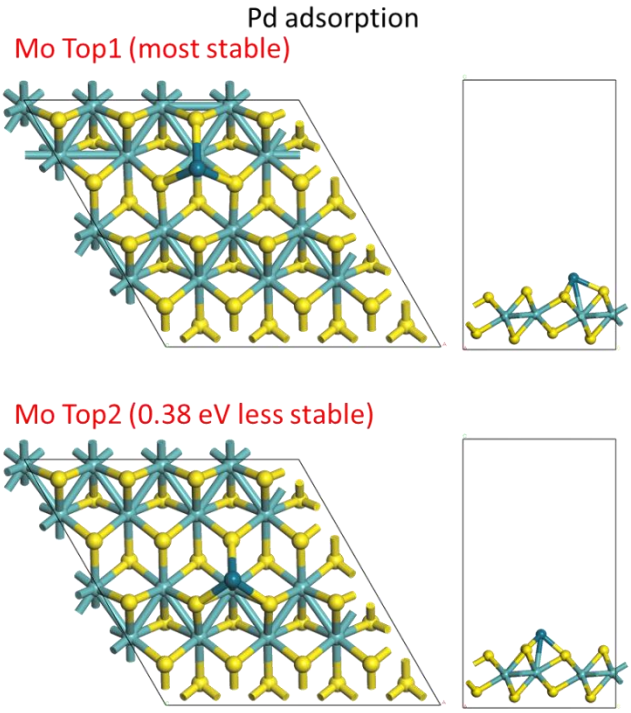


Figure 4.17 Computational simulation of Pd doped at Mo top1 and Mo top 2 site

Table 4.4 DFT calculations of X (X=Pd, Pt) doping on 1T'-MoS_2.

Dopant atom (X)	X Binding Site	Adsorption energy (eV)
Pt	Mo_1	-3.93
Pt	Mo_2	-3.40
Pd	Mo_1	-2.91
Pd	Mo_2	-2.52

Adsorption energies of Pd and Pt dopants (X) on the 1T'-MoS_2 surface relative to the respective metal ions in the gas phase. Two stable adsorption sites were found, both on top of Mo atoms where Mo is either bound to 1 top layer S_u atom and 2 top layer S_L atoms (Mo_1) or 2 top layer S_u atoms and 1 top layer S_L atom (Mo_2).

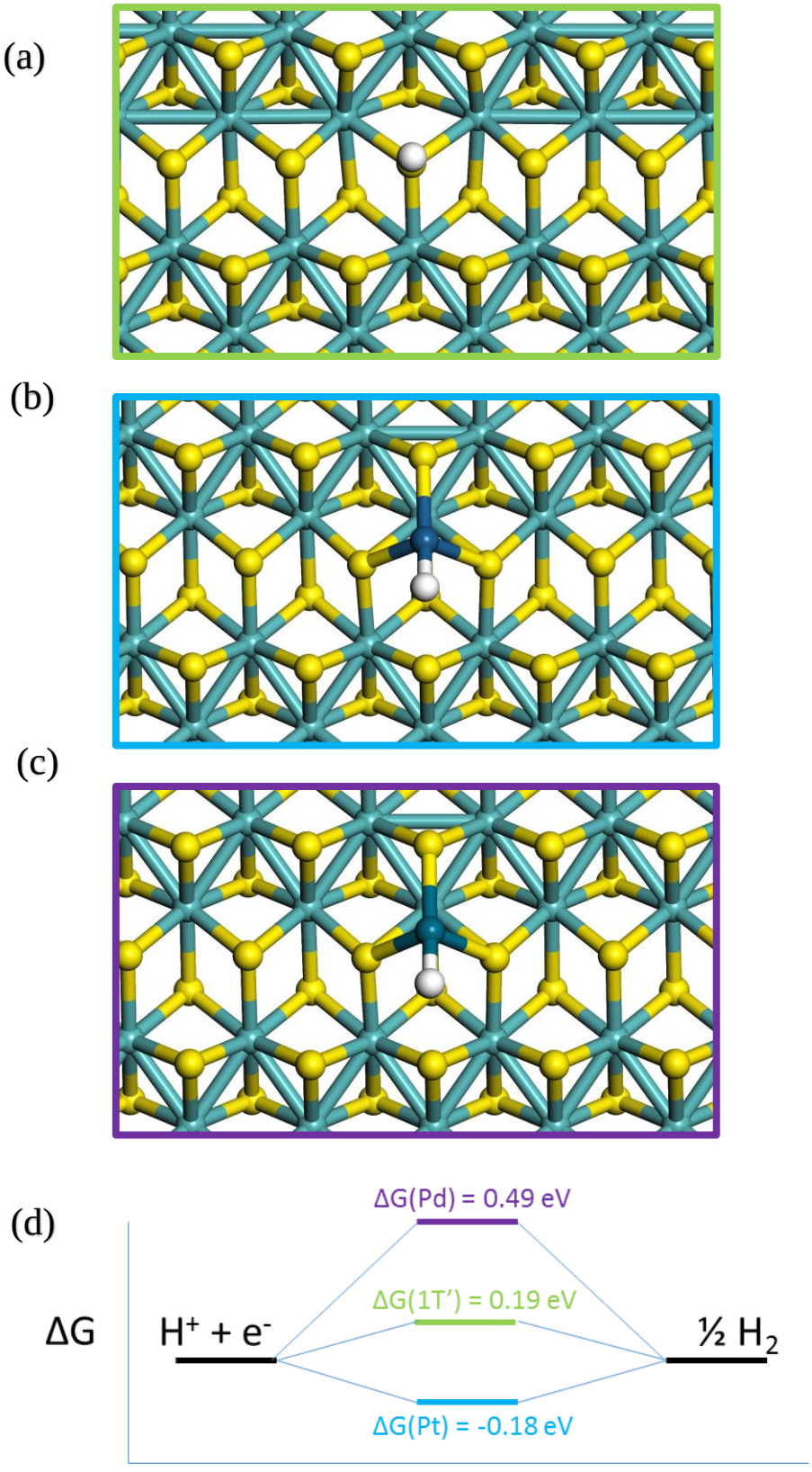


Figure 4.18. Most stable adsorption configuration for 1 H adatom on (a) 1T'-$^{S}MoS_2$ tensile-strained S atom top site (E_{ads}(H)=-0.06 eV) (b) Pt-1T'-$^{S}MoS_2$ top site (E_{ads}(H)=-0.43 eV) and (c) Pd-1T-$^{S}MoS_2$ top site. (E_{ads}(H)=+0.24 eV) (d) ΔG(H*) of 1T'-$^{S}MoS_2$, Pt- and Pd-doped 1T'-$^{S}MoS_2$. ΔG is calculated using the equation: $E_{ads}(H) = E_{DFT}(surf+H) - E_{DFT}(surf) - 0.5*E_{DFT}(H_2)$ and thus ($\Delta G(H) \approx E_{ads}(H)+0.25eV$).

Table 4.5. DFT adsorption and free energies for H binding on Pd 1T'-MoS_2.

Surface	Site(s)	ΔE_{nH*}^{ads} (eV)	E_{ZPE} (eV)	ΔG_{nH*} (eV)
Pd 1T'-MoS_2	S_L	0.43	0.21	0.71
	X_T	0.24	0.18	0.49
	$X_T \times 2$	-0.33	0.37	0.17
	$X_T + S_L$	0.69	0.42	1.24

Adsorption energies ΔE_{nH*}^{ads}, zero point energiesE_{ZPE} and free energies of adsorption ΔG_{nH*} for a H adatom on the Pd top site (X_T), proximal upper S (S_u) and lower S (S_L) sites of 1T'-MoS_2 doped with Pd at the Mo_1 position. Values are also given for the lowest energy configurations of 2 H adatoms at the Pd top site ($X_T \times 2$) and one H adatom at the Pd top site and 1 H adatom at a proximal lower S site ($X_T + S_L$).

Table 4.6. DFT adsorption and free energies for H binding on Pt 1T'-MoS_2.

Surface	Site(s)	ΔE_{nH*}^{ads} (eV)	E_{ZPE} (eV)	ΔG_{nH*} (eV)
Pt 1T'-MoS_2	S_L	0.44	0.22	0.73
	X_T	-0.45	0.20	-0.18
	$X_T \times 2$	-0.89	0.42	-0.34
	$X_T + S_L$	-0.17	0.16	0.40

Adsorption energies ΔE_{nH*}^{ads}, zero point energiesE_{ZPE} and free energies of adsorption ΔG_{nH*} for a H adatom on the Pt top site (X_T), proximal upper S (S_u) and lower S (S_L) sites of 1T'-MoS_2 doped with Pt at the Mo_1 position. Values are also given for the lowest energy configurations of 2 H adatoms at the Pt top site ($X_T \times 2$) and one H adatom at the Pt top site and 1 H adatom at a proximal lower S site ($X_T + S_L$).

4.6.2. Recombination of H* on TM-1T-$^{S}MoS_2$

To explore the aforementioned inconsistency, we compute the Tafel barriers for recombinative H_2 desorption from TM-1T-$^{S}MoS_2$ (Table 4.5 and 4.6). As with the pure 1T-$^{S}MoS_2$ surface we first consider the most stable configuration for the co-adsorption of two H atoms proximal to the transition metal dopants. In both cases this configuration has both H directly bound to the Pt or Pd, though the binding configurations are different depending on the TM. On Pt dopant atoms, the co-adsorption is as two dissociated H adatoms whereas on Pd the adsorption is molecular. Interestingly, we find no molecular state on the former and no dissociated state on the latter. The ΔG(H*) for the co-adsorbed configurations on Pt- and Pd-doped 1T-$^{S}MoS_2$ are -0.34 eV and +0.17 eV, respectively. Our calculations show that on both TM-doped 1T-$^{S}MoS_2$ surfaces, the adsorption of $H_{2\,(g)}$ is non-activated, thereby making the barrier for $H_{2\,(g)}$ evolution via the Tafel mechanism equivalent to the negative of the adsorption energy for 2 H*. Thus, the activation energy

for the Tafel step is lowered from 1.15 eV on undoped 1T-$^{S}MoS_2$ to 0.89 eV and 0.33 eV on Pt- and Pd-doped 1T-$^{S}MoS_2$, respectively (Figure 4.19). The relative ordering of these activation barriers is in line with the HER activities we recorded in experiment.

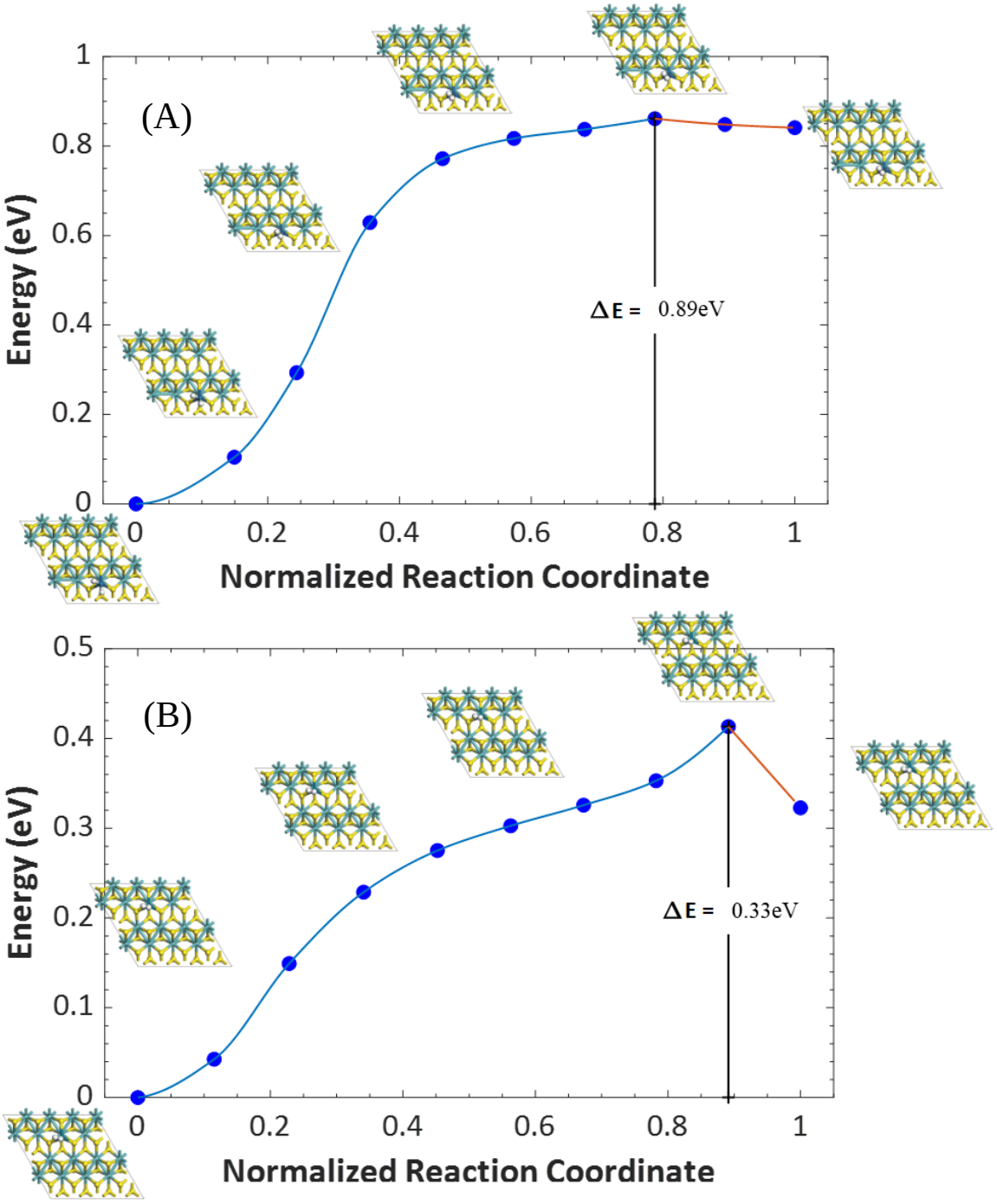


Figure 4.19. Normalised Reaction Coordination Graph of Tafel recombination step for 2 H* adsorbed on (a) Pd-1T-$^{S}MoS_2$ and (b) Pt-1T'-$^{S}MoS_2$ as computed with DFT and the climbing image NEB method

Based on these insights from DFT calculations, we propose that the single dopant atoms are not solely responsible for observed HER activity of TM-1T-$^{S}MoS_2$. If this were the case, we would expect near thermoneutral adsorption of H* or at least values of ΔG(H*) that are closer to zero than that for pure 1T-$^{S}MoS_2$. However in our case, the endothermic and weak adsorption of H* (ΔG(H*) = +0.49 eV) on the dopant atom in Pd-1T-$^{S}MoS_2$ suggests that H^+ reduction via the Volmer step will be unfavourable and slow at this site, when in fact we observe the opposite; our experimental Tafel analysis demonstrates this catalyst is not limited by Volmer kinetics, but rather by $H_{2\,(g)}$ desorption. Given the low coverage of Pd dopant atoms, the largest portions of the catalytic surface remain as undoped 1T-$^{S}MoS_2$ and are therefore still able to perform facile H^+ reduction. Based on our HAADF-STEM imaging, there appears to be a negligible effect to the structure and scattering intensity of Mo as close as first nearest neighbour to the dopant atoms. Thus, if we assume that modifications to the surface chemistry far from the dopant atoms are also negligible, a vast number of pristine 1T-$^{S}MoS_2$ sites will remain highly active for the Volmer step given a low kinetic barrier of 0.16 eV.[15]

The facile uptake of H^+ from the aqueous phase will allow for well-maintained high H coverage across the 1T surface as we have observed experimentally. In fact previous studies of pure 1T phase have suggested the H* coverage at equilibrium to be between 25 and 35 %. [33] A well-established equilibrium coverage in conjunction with high mobility of H* on the surface will facilitate diffusion into the Pd site. Notably such a diffusion of a single H* is endothermic by 0.35 eV, however at higher coverage diffusion into an already occupied Pd site to form the co-adsorbed Tafel step initial state from that on pure 1T-$^{S}MoS_2$ is highly favourable and exothermic by 0.31 eV. Thus, diffusion across the surface will allow H* to be shuttled from regions of pristine 1T-$^{S}MoS_2$ to the well-

dispersed Pd dopant sites (Oxidative Addition) where the latter can facilitate H-H recombination via the Tafel step (Reductive Elimination) and therefore the composite single TM doped catalyst clearly operates bi-functionally (Figure 4.20). This mechanistic cycle ultimately accounts for the detection of both Pd^0 and Pd^{2+} species in our X-ray analyses. (Figure 4.21) Notably, we do not explore the possibility of the dopant atom facilitating the Heyrovsky step as this would require explicit modelling of the interfacial solvent, however it remains entirely possible that these single atoms also lower the Heyrovsky barrier as well as the Tafel barrier, though in either case the catalyst will be bi-functional.

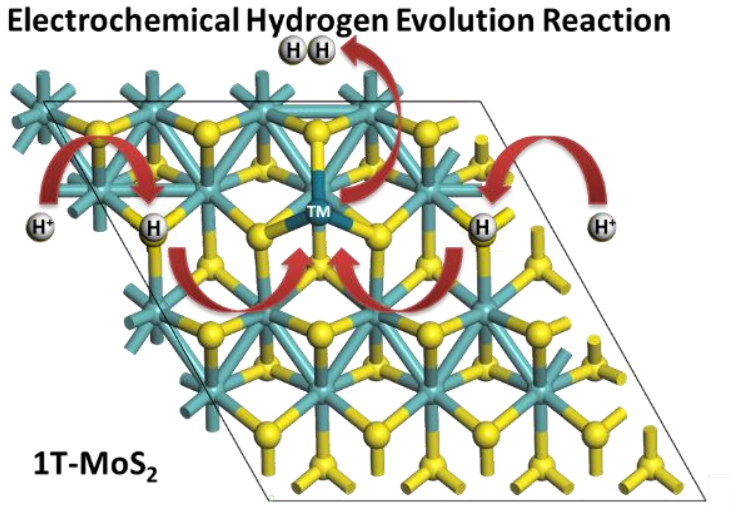


Figure 4.20. Simplified mechanism of electrochemical HER catalysed by TM-1T'-^{S}MoS2

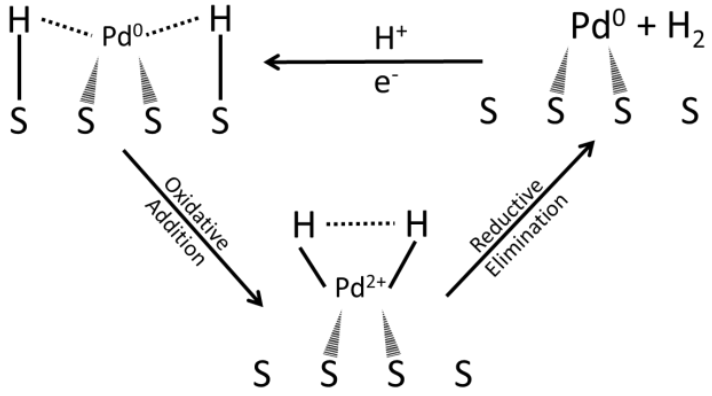


Figure 4.21 The change in oxidation state of a doped single Pd on 1T'-$^{S}MoS_2$ atom during HER reaction.

4.7 Conclusions

In conclusion, we have provided direct experimental evidence that single transition metal atoms such as Pd and Pt can be chemically attached to the S sites of basal plane of the n-butyl lithium exfoliated 1T-$^{S}MoS_2$ by a mild radical assisted reduction of metal precursors using sonication in water/isopropanol at room temperature. The HADDF-STEM images, EELS mapping and XAS analyses suggest that there is no significant change to the crystallographic parameters of the underneath allergically unstable monolayer 1T-$^{S}MoS_2$ polymorph; hence no conversion to 2-H phase upon the metal doping is reassured. Despite the low metal doping content their measured HER activity is shown to be far superior than corresponding 2-H $^{S}MoS_{2;}$ no significant deactivation is observed after 1000 catalytic cycles. High hydrogen coverage at steady state is maintained on this metallic 1-T surface during the HER as revealed by ^{1}H NMR and kinetic analysis. Tafel slope analysis and DFT modelling suggest that the first proton reduction step from water on this surface is greatly facilitated, hence rendering the Volmer step non-rate limiting, in contrast to that of 2-H $^{S}MoS_2$. The inclusion of single Pd doper can also offer dramatic acceleration on the rate limiting recombination of H to H_2. As a result, a bifunctional catalysis for HER over this tailored composite structure is for the first time demonstrated, which outperforms most reported catalysts in this area. As shown from the DFT calculations, both the geometric and electronic factors exerted by the single TM dopants are therefore important parameters in further tuning the 2D 1T-$^{S}MoS_2$ structure for rational design of the composite materials as efficient bifunctional electrocatalysts with immense potential for various electrochemical applications in the energy industries.

4.8 References

(1) Lau, T. H. M.; Lu, X.; Kulhavý, J.; Wu, S.; Lu, L.; Wu, T. S.; Kato, R.; Foord, J. S.; Soo, Y. L.; Suenaga, K.; Tsang, S. C. E. Transition Metal Atom Doping of the Basal Plane of MoS2monolayer Nanosheets for Electrochemical Hydrogen Evolution. *Chem. Sci.* **2018**, *9*, 4769–4776.

(2) Tsai, C.; Abild-pedersen, F. Tuning the MoS 2 Edge-Site Activity for Hydrogen Evolution via Support Interactions. **2014**.

(3) Li, T.; Galli, G. Electronic Properties of MoS 2 Nanoparticles. *J. Phys. Chem. C* **2007**, *111*, 16192–16196.

(4) Ito, Y.; Cong, W.; Fujita, T.; Tang, Z.; Chen, M. High Catalytic Activity of Nitrogen and Sulfur Co-Doped Nanoporous Graphene in the Hydrogen Evolution Reaction. *Angew. Chemie - Int. Ed.* **2015**, *54*, 2131–2136.

(5) Zhong, Y.; Xia, X. H.; Shi, F.; Zhan, J. Y.; Tu, J. P.; Fan, H. J. Transition Metal Carbides and Nitrides in Energy Storage and Conversion. *Adv. Sci.* **2015**, *3*.

(6) Ambrosi, A.; Sofer, Z.; Pumera, M. Lithium Intercalation Compound Dramatically Influences the Electrochemical Properties of Exfoliated MoS2. *Small* **2015**, *11*, 605–612.

(7) Kappera, R.; Voiry, D.; Yalcin, S. E.; Branch, B.; Gupta, G.; Mohite, A. D.; Chhowalla, M. Phase-Engineered Low-Resistance Contacts for Ultrathin MoS2transistors. *Nat. Mater.* **2014**, *13*, 1128–1134.

(8) Splendiani, A.; Sun, L.; Zhang, Y.; Li, T.; Kim, J.; Chim, C. Y.; Galli, G.; Wang, F. Emerging Photoluminescence in Monolayer MoS2. *Nano Lett.* **2010**, *10*, 1271–1275.

(9) Acerce, M.; Voiry, D.; Chhowalla, M. Metallic 1T Phase MoS2nanosheets as Supercapacitor Electrode Materials. *Nat. Nanotechnol.* **2015**, *10*, 313–318.

(10) Lukowski, M. A.; Daniel, A. S.; Meng, F.; Forticaux, A.; Li, L.; Jin, S. Enhanced Hydrogen Evolution Catalysis from Chemically Exfoliated Metallic MoS2 Nanosheets. *J. Am. Chem. Soc.* **2013**, *135*, 10274–10277.

(11) Voiry, D.; Salehi, M.; Silva, R.; Fujita, T.; Chen, M.; Asefa, T.; Shenoy, V. B.; Eda, G.; Chhowalla, M. Conducting MoS2 Nanosheets as Catalysts for Hydrogen Evolution Reaction. *Nano Lett.* **2013**, *13*, 6222–6227.

(12) Tsai, C.; Chan, K.; Nørskov, J. K.; Abild-Pedersen, F. Theoretical Insights into the Hydrogen Evolution Activity of Layered Transition Metal Dichalcogenides. *Surf. Sci.* **2015**, *640*, 133–140.

(13) Putungan, D. B.; Lin, S.; Kuo, J. A First-Principles Examination of Conducting Reaction and Its Enhancement by Strain †. **2015**, *2*, 21702–21708.

(14) Phys, J. C. A New (2 × 1) Dimerized Structure of Monolayer 1T-Molybdenum Disulfide , Studied from First Principles Calculations. **2016**, *174702*.

(15) Tang, Q.; Jiang, D. E. Mechanism of Hydrogen Evolution Reaction on 1T-MoS2from First Principles. *Acs Catal.* **2016**, *6*, 4953–4961.

(16) Wypych, F.; Schollhorn, R. 1T-MoS2 , a New Metallic Modification of Molybdenum Disulfide. *J. CHEM. SOC.. C'HEM. COMMUN.* **1992**, No. 1386, 1386–1388.

(17) Liu, G.; Robertson, A. W.; Li, M. M.-J. J.; Kuo, W. C. H. H.; Darby, M. T.; Muhieddine, M. H.; Lin, Y.-C. C.; Suenaga, K.; Stamatakis, M.; Warner, J. H.; Tsang, S. C. E. MoS2 Monolayer Catalyst Doped with Isolated Co Atoms for the Hydrodeoxygenation Reaction. *Nat. Chem.* **2017**, *9*, 810–816.

(18) Ding, Q.; Song, B.; Xu, P.; Jin, S. Efficient Electrocatalytic and Photoelectrochemical Hydrogen Generation Using MoS 2 and Related Compounds. *CHEMPR* **2016**, *1*, 699–726.

(19) Carolina, N. Rapid Synthesis of Gold and Platinum Nanoparticles Using Metal Displacement Reduction with Sonomechanical Assistance. **2006**, *18*, 18–21.

(20) Jin, B.; Bang, H.; Suslick, K. S. Applications of Ultrasound to the Synthesis of Nanostructured Materials. **2010**, 1039–1059.

(21) Kresse, G.; Furthmu, J. Efficient Iterative Schemes for Ab Initio Total-Energy Calculations Using a Plane-Wave Basis Set ¨. **1996**, *54*.

(22) Kresse, G.; Furthmiiller, J. Efficiency of Ab-Initio Total Energy Calculations for Metals and Semiconductors Using a Plane-Wave Basis Set Av *. **1996**, *6*, 15–50.

(23) Kresse, G.; Joubert, D. From Ultrasoft Pseudopotentials to the Projector Augmented-Wave Method. **1999**, *59*, 11–19.

(24) Blöchl, P. E. Projector Augmented-Wave Method. *Phys. Rev. B* **1994**, *50*.

(25) Perdew, J. P.; Burke, K.; Ernzerhof, M. Generalized Gradient Approximation Made Simple. **1996**, No. 3, 3865–3868.

(26) Hu, T.; Li, R.; Dong, J. A New (2 × 1) Dimerized Structure of Monolayer 1T-Molybdenum Disulfide, Studied from First Principles Calculations. *J. Chem. Phys.* **2013**, *139*.

(27) Henkelman, G.; Jónsson, H. Improved Tangent Estimate in the Nudged Elastic Band Method for Finding Minimum Energy Paths and Saddle Points. **2016**, *9978*.

(28) Henkelman, G.; Jónsson, H. A Dimer Method for Finding Saddle Points on High Dimensional Potential Surfaces Using Only First Derivatives. **2010**, *7010*.

(29) Henkelman, G.; Jo, H. A Climbing Image Nudged Elastic Band Method for Finding Saddle Points and Minimum Energy Paths and Minimum Energy Paths. **2014**, *9901*.

(30) Setthapun, W.; Williams, W. D.; Kim, S. M.; Feng, H.; Elam, J. W.; Rabuffetti, F. A.; Poeppelmeier, K. R.; Stair, P. C.; Stach, E. A.; Ribeiro, F. H.; Miller, J. T.;

Marshall, C. L. Genesis and Evolution of Surface Species during Pt Atomic Layer Deposition on Oxide Supports Characterized by in Situ XAFS Analysis and Water-Gas Shift Reaction. *J. Phys. Chem. C* **2010**, *114*, 9758–9771.

(31) Tavares, M. C.; Machado, S. A. S.; Mazo, L. H. Study of Hydrogen Evolution Reaction in Acid Medium on Pt Microelectrodes. *Electrochim. Acta* **2001**, *46*, 4359–4369.

(32) Ding, Q.; Song, B.; Xu, P.; Jin, S. Efficient Electrocatalytic and Photoelectrochemical Hydrogen Generation Using MoS 2 and Related Compounds. *CHEMPR* **2016**, *1*, 699–726.

(33) Mason, J. Conventions for the Reporting of Nuclear Magnetic Shielding (or Shift) Tensors Suggested by Participants in the NATO ARW on NMR Shielding Constants at the University of Maryland , College Park , July 1992. **1993**, *2*, 285–288.

Chapter 5

Rhenium and Indium doped 1T-$^{S}MoS_2$ for Electrochemical Reduction of Carbon Dioxide

5.1. Introduction

Carbon capture and utilisation is currently one of the growing research areas in mitigating climate change. It aims to capture waste CO_2 and convert it into more reduced carbon feedstocks with the help of hydrogen. High energy-density liquid fuels, such as methanol and ethanol, are some of the important liquefied hydrocarbon products of this conversion process that have multiple industrial and energy applications[1]. Today, around 42% of the global CO_2 emissions are produced during fuel combustion for generating electricity and heat[2]. To reduce the expected increase of global average temperature to 2 °C by 2050, the global anthropogenic CO_2 emission has to be reduced by at least 50%[3]. Catalytic systems connected to carbon capture systems can be installed at large point sources such as power plants for effective CO_2 reduction reaction (CO_2RR) to help alleviate the CO_2 emissions and produce valuable hydrocarbons[2]. Since electrochemical CO_2RR can be operated both under ambient condition and scaled-up easily, this makes electrocatalytic cell a favourable system in this case.

However, there are still challenges that limited the electrocatalytic system to be widely commercialised. The onset potential of the CO_2RR reaction is closed to that of electrochemical hydrogen evolution reaction (HER), the reaction which we have discussed in the last two chapters. Thus, the optimised applied potential and reaction

conditions in an aqueous electrochemical cell need to be carefully tuned to avoid the interference from this competing reaction. Although traditional metal catalysts are often used in CO_2RR because of their high activity and stability, the selectivity of heterogeneous catalyst is still of great concern as it is difficult to control the reaction pathway. Electroreduction of CO_2 involves multiple charge transfers to convert CO_2 into more active hydrocarbons. The initial adsorption of CO_2 onto the cathodic surface is generally considered to be the rate-determining step due to its high energy barrier[4]. Adsorbed CO_2 ($*CO_2^{\bullet-}$) will then readily interact with other available intermediates, such as other adsorbed C species or adsorbed H, for further recombinative processes. The distribution of end products is found to be governed by the reactivity of the active sites of the catalyst.[5] It is therefore important to understand the reaction mechanism of this rate-determining step at an atomic level when designing a catalyst for improved electrochemical CO_2RR.

In the last two chapters, we focused on the electrocatalytic performance of Pt and Pd doped metallic molybdenum disulphide monolayers (Pt-1T-$^{S}MoS_2$ and Pd-1T-$^{S}MoS_2$) for electrochemical HER. It was found that the basal sites of 1T-MoS_2 are preferable for H adsorption while the doped single Pd and Pt atoms are superior recombination sites of adsorpted H for forming dihydrogen gas. Clearly, these two metal atom modifiers can favour HER, which should be avoided for this application. Herein, we would like to extend the scope of research by studying electrochemical CO_2RR with the related findings we just obtained. To our knowledge, the catalytic behaviour of single metal doped 1T-MoS_2 materials for CO_2RR has not been studied. While for 2H-MoS_2, there is only one example for now. Single Nb atoms doped onto the vertically aligned ultrathin 2H-MoS_2 exhibits CO2RR activity with 82% faradaic efficiency (FE) to CO at -0.8V[6],

which is much higher than that of monolayer MoS_2[7] (16.6% CO FE at -1.15V). DFT calculations showed that the MoS_2 surface facilitates the formation of *CO intermediate and thus the rate determining step of the overall reaction will be on the *CO desorption. The presence of single Nb atom alternate the electronic density of surrounding edges sites which ultimately weaken the *CO binding to the active edge sites.

Herein, we investigated the electrocatalytic CO_2RR performance of Re and In doped 1T-$^{S}MoS_2$. Re and In atoms were chosen as the dopants since their filled electron orbitals, especially the stereochemical lone-pair electrons in the latter, were expected to facilitate bonding with CO_2 by π back donation. Electrochemical system coupled with in-situ Fourier-transform infrared spectrometer (FTIR) spectrometer was used to further study their electrochemical interfaces and adsorbed intermediates in real time. A highly sensitive 700 MHz liquid ^{1}H nuclear magnetic resonance spectrometer (NMR) was also employed to quantify the liquid hydrocarbon products in the electrolyte. Both Re-1T-$^{S}MoS_2$ and In doped 1T-$^{S}MoS_2$ exhibit improved intrinsic CO_2 reduction activity when compared to pristine MoS_2. Our DFT calculations demonstrated that the incorporation of these two single atom dopants is able to suppress the competitive hydrogen evolution reaction but enhance CO_2RR in our aqueous electrochemical system. The NMR results also suggested that Re and In can help to facilitate the production of alcohols from the CO_2RR.

5.2. Computational and Experimental Details

5.2.1. Electrochemical Measurement

A three-electrode system controlled by μ-AUTOLAB III potentiostat (Eco-Chemie, Netherlands) was applied to carry out the general electrochemical measurements. The electrochemical cell was also attached onto the in situ ATR-IR spectrometer for real time

analysis. A platinum coil counter electrode and an Ag|AgCl (1molL^{-1} KCl) reference electrode were used in this study. To prepare the working electrode, 4 mg of the electrocatalyst and 80 μL of 5 wt% Nafion®117 solution was dispersed in 1 mL of water/ethanol (4:1 v/v) and then followed by 30 min sonication to create a homogeneous ink. The ink was then drop-coated onto the surface of a glassy carbon rotating electrode with a surface diameter of 3 mm. CO_2 saturated 0.5M $KHCO_3$ was used as the electrolyte for the electrochemical reduction of CO_2. All measurements were calibrated with respect to the reversible hydrogen electrode (RHE).

5.2.2. Density Functional Theory

All periodic, spin-polarized, planewave DFT total energy minimization calculations were performed using the Vienna Ab Initio Simulation Package (VASP) version 5.4.1 [8,9] with the projector augmented wave (PAW) method [10,11] to model core ionic potentials and the functional of Perdew-Burke-Ernzerhof (PBE) for the exchange-correlation.[12] Our calculations used a 4 × 2 single nanosheet slab of 1T'-MoS_2 where a layer of 16 Mo atoms is sandwiched by two 16 S atom layers and all atoms were free to move. The lattice parameters of the 1T'-MoS_2 unit cell were optimized using an anisotropic volume expansion giving a = 3.18 Å and b = 6.56 Å, in good agreement with previous work.[13] Note a 4 × 4 unit cell was used for undistorted 1T-MoS_2 calculations where a = b = 3.18 Å. A vacuum region of approximately 17 Å was used to minimize periodic interactions in the z-direction. We used 5 × 5 × 1 and 4 × 4 × 1 Monkhorst-Pack k-point meshes to sample the Brillouin zone for 1T' and 1T, respectively. The planewave kinetic energy cutoff was set to 400 eV in all cases. To aid with convergence, we employed Gaussian smearing with a smearing width set to 0.05 eV. We ensured electronic self-consistency up to a tolerance of 10^{-6} eV and during ionic relaxation, we performed conjugate gradient minimization of the Hellmann-Feynman forces to within a tolerance of 10^{-2} eV·Å^{-1}. To

locate transition states we utilized the dimer and climbing image NEB methods as implemented in VASP Transition State Tools version 3.1.[14–16] We confirmed that the transition states correspond to 1st order saddle points on the potential energy surface through vibrational frequency analysis using finite displacements of 0.02 Å.

The free energy change upon the adsorption of n hydrogen adatoms (ΔG_{nH*}) is computed from the adsorption energy of hydrogen (ΔE_{nH*}^{ads}) according to the following equations:

$$\Delta E_{nH*}^{ads} = E_{Tot}(slab + nH) - E_{Tot}(slab) - \frac{n}{2} E_{Tot}(H_2)$$

where $E_{Tot}(slab + nH)$, $E_{Tot}(slab)$ and $E_{Tot}(H_2)$ are the DFT total energies of H adsorbed on the 1T'-MoS_2 slab, the clean 1T'-MoS_2 slab and gas phase H_2;

$$\Delta G_{nH*} = \Delta E_{nH*}^{ads} + \Delta E_{ZPE} - T \cdot \Delta S_n$$

where ΔE_{ZPE} is the difference in the zero point energy of hydrogen in the adsorbed state and the gas phase, T is the temperature and ΔS_{nH*} is the entropy difference between adsorbed and gas phase hydrogen. The latter can be approximated as $\Delta S_{H*} \approx -\frac{1}{2} S_{H_2}^0$ (Reference), where $S_{H_2}^0$ is the entropy of gaseous molecular hydrogen at standard conditions (298 K, 1 bar). Note that more negative values of ΔG_{nH*} correspond to more stable binding.

The free energy change upon the adsorption of different adsorbate in CO_2RR is computed from the according to the following equations:

$$\Delta E_{ads} = E_{Tot}^{slab} - E_{Tot}^{doped\text{-}1T} - \{ xE_{Tot}^{H2O} + yE_{Tot}^{H2} + zE_{Tot}^{CO2} \}$$

where $E_{Tot}(slab)$, $E_{Tot}(doped1T)$, $E_{Tot}(H_2O)$, $E_{Tot}(H_2)$ and $E_{Tot}(CO_2)$ are the DFT total energies of the adsorbate adsorbed on the 1T'-MoS_2 slab, the clean 1T'-MoS_2 slab and gas phase gas phase CO_2, H_2O and H_2.

5.3. Structural Characterisation of Re and In doped 1T-$^{S}MoS_2$

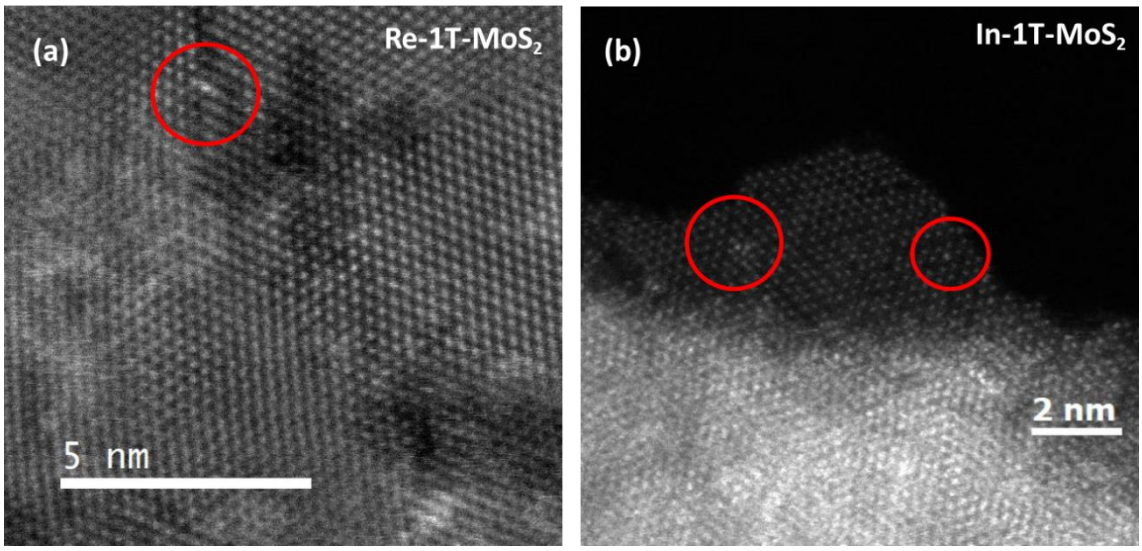


Figure 5.1 HAADF-STEM of Re-1T-$^{S}MoS_2$ and In-1T-$^{S}MoS_2$.

3% Re- and In- doped 1T-$^{S}MoS_2$ were synthesised by reacting ReO_2 and In_2O_3 precursors, respectively with as-prepared 1T-$^{S}MoS_2$ in an ultrasonic bath. (As aforementioned in the previous chapter, we refer both phases as "1T" with no attempt to distinguish the small 2H phase from the 1T phase to avoid unnecessary complications.) All the synthetic procedures of 1T-$^{S}MoS_2$ and doped 1T-$^{S}MoS_2$ can be found in Chapter 4.2 and thus is not repeated here. To confirm the successful doping of fully dispersed single Re and In atoms onto 1T-$^{S}MoS_2$ surface, high-angle annular dark field scanning transmission electron microscopy (HAADF-STEM) was employed. Bright spots corresponding to single Re and In atoms with sizes of around 0.2 nm can be observed in the red circles in figure 5.1a and b. 1T surface can also be observed on the surface which indicates the successful phase transition during monolayer exfoliation[17]. It should be noted that our nanosheets appears not to be fully monolayers as unavoidable restacking process occurs during the drop-casting of the catalyst on the STEM grids for imaging.

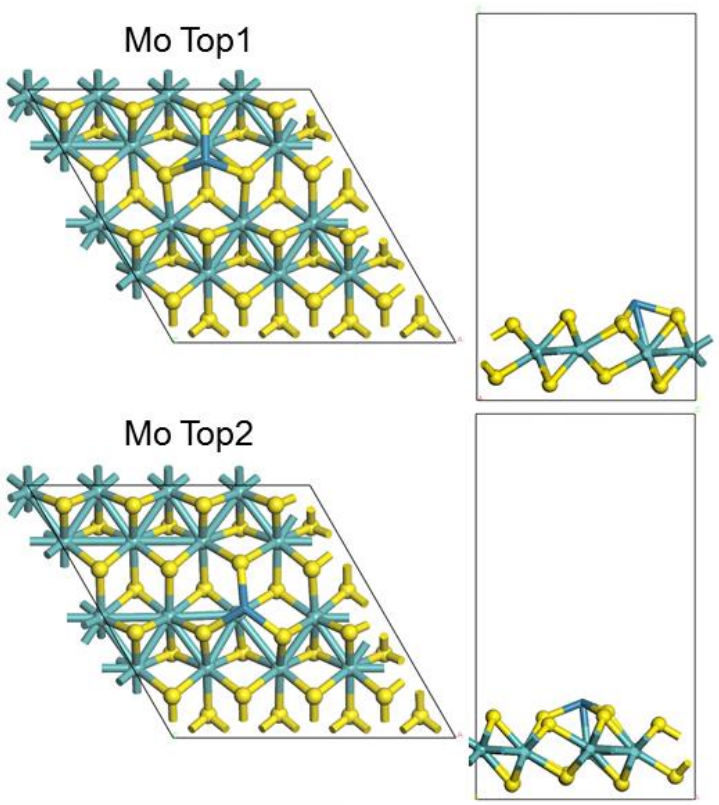


Figure 5.2 Computational simulation of Re doped at Mo top1 and Mo top 2 sites of 1T'-$^{S}MoS_2$

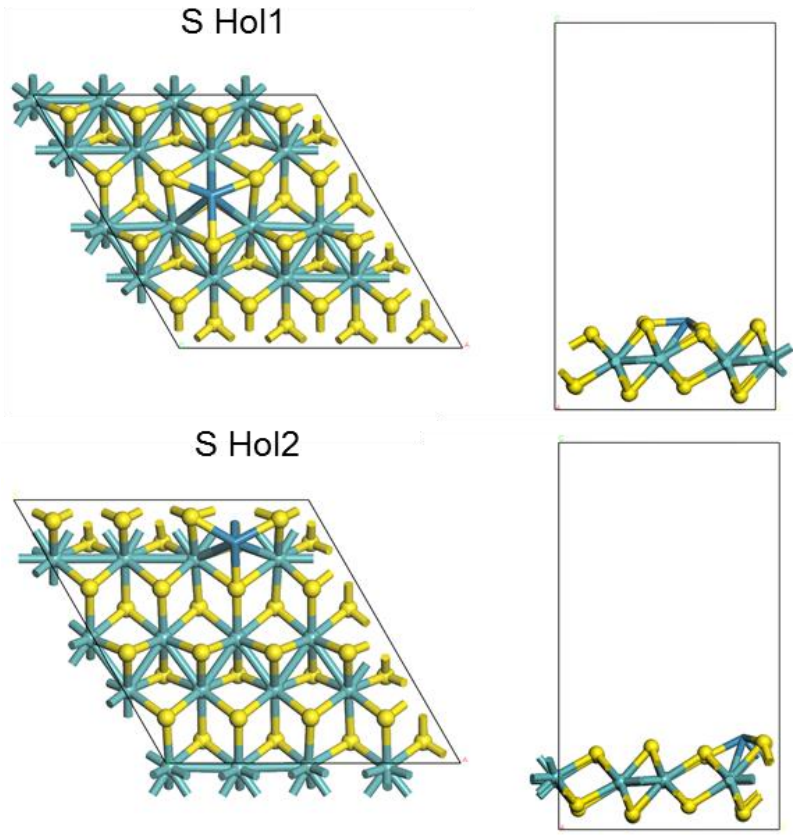


Figure 5.3 Computational simulation of Re doped at S ho1 1 and S hol 2 sites on 1T'-$^{S}MoS_2$

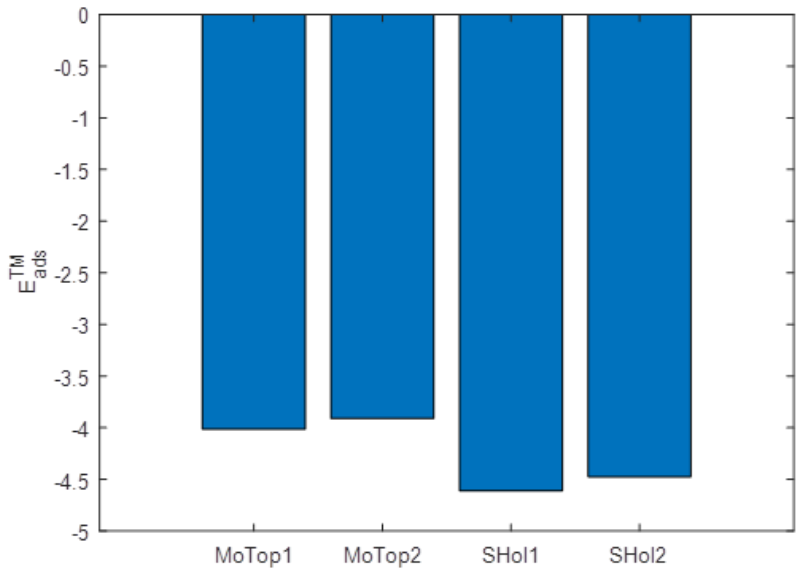


Figure 5.4 Adsorption energies of Re doped on different sites of 1T'-$^{S}MoS_2$

Computational calculations were conducted to study the possible doping sites for Re and In atoms. Due to the reduction in surface symmetry of the 1T'-$^{S}MoS_2$ upon lattice distortion, Re atom can be possible bound to two different Mo top sites, namely: Mo Top 1: one compressive-strained S atom and two tensile-strained S atoms and Mo Top 2: two compressive-strained S atom and one tensile-strained S atoms (Figure 5.2). Also, there are two different S hollow sites, namely: S Hollow site 1: one compressive-strained S atom and two tensile-strained S atoms and S Hollow site 2: two compressive-strained S atom and one tensile-strained S atoms (Figure 5.3). The adsorption energies of Re doped on different doping sites were calculated and shown in Figure 5.4, which suggest that S hollow site 1 is the most thermodynamic stable adsorption site. Thus, Re atom can be octahedrally coordinated to 3 x S and 3 x Mo in the hollow site. Similarly, there are two possible sites for In adsorption, namely: S hollow site 1 and Mo top site 1 (Figure 5.5), and the calculation of adsorption energies suggested Mo top site is the more stable one between the two sites. It is noticed that In actually is positioned close to the Mo top site

but primarily bridged between 2 x S atoms according to energy minimization. (Figure 5.6)

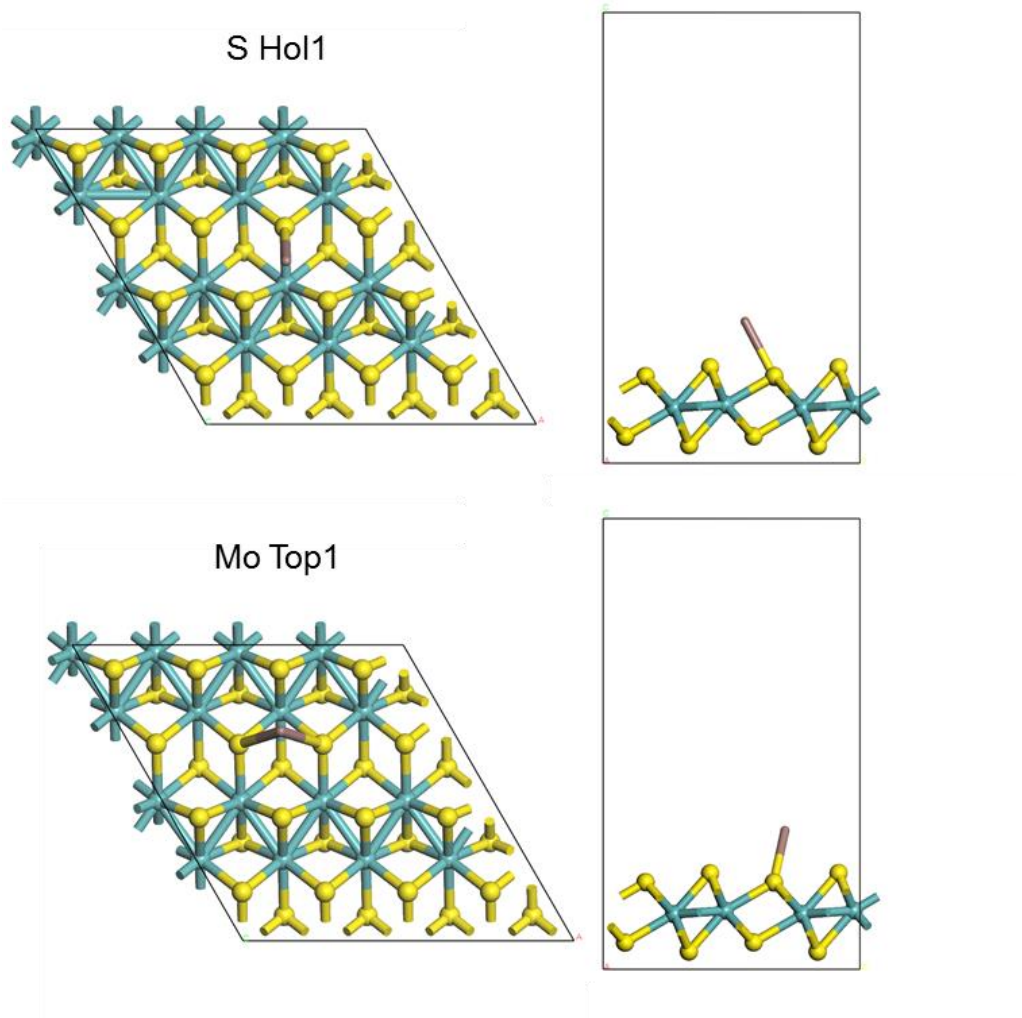


Figure 5.5 Computational simulation of In doped at S ho1 1 and Mo hol 1 sites on 1T'-$^{S}MoS_2$

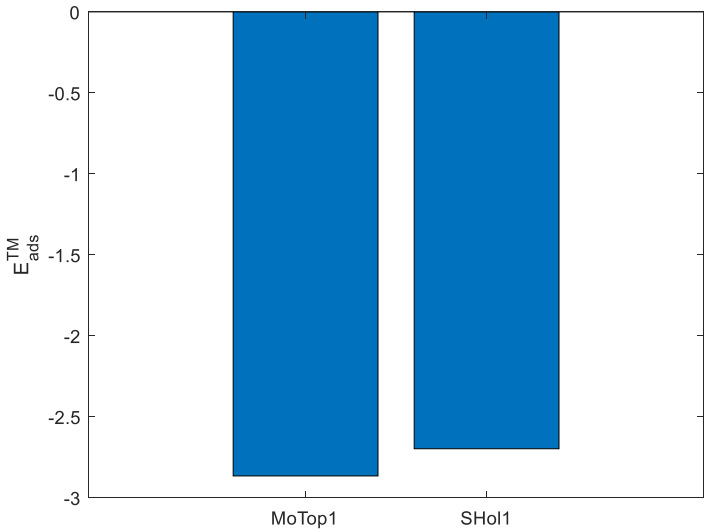


Figure 5.6 Adsorption energies of Re doped on different sites of 1T'-$^{S}MoS_2$

5.4. Electrochemical analysis of Re and In doped 1T-$^{S}MoS_2$ for CO_2RR

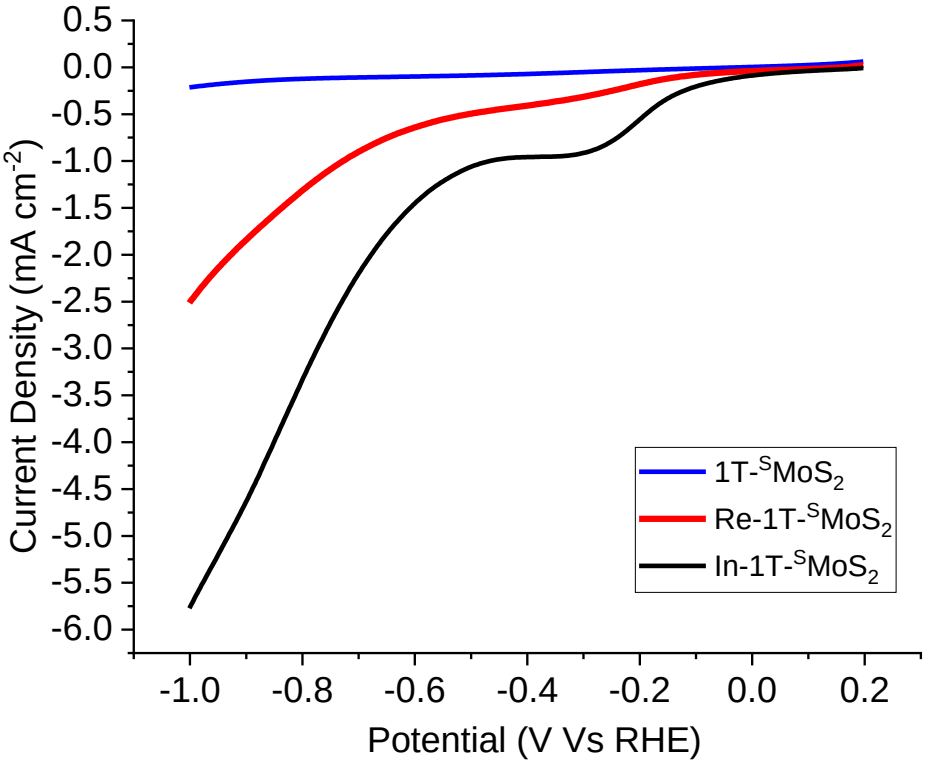


Figure 5.7 LSV curves of 1T-MoS_2 materials at a potential range from 0.3 to -1.0V in CO_2 saturated 0.5M $KHCO_3$ with a scan rate of 50mV/s.

The activity in the electrochemical reduction of CO_2 was evaluated by linear sweep voltammetry (LSV). Figure 5.7 shows the LSV curves of Re-1T-$^{S}MoS_2$, In-1T-$^{S}MoS_2$, and pristine 1T-$^{S}MoS_2$ at a potential range from 0.2 V to -1.0 V in CO_2 saturated 0.5M $KHCO_3$ with a scan rate of 50 mV/s. It can be seen that the pristine 1T-$^{S}MoS_2$ exhibited negligible CO_2 reduction activities. The shape of the other two LSV curves suggested that a multiple-stepwise CO_2 reduction process occurred as two shoulder peaks can be observed at ~-0.2V and ~-0.6V, respectively. In general, In-1T-MoS_2 produced a larger cathodic current density among the three samples.

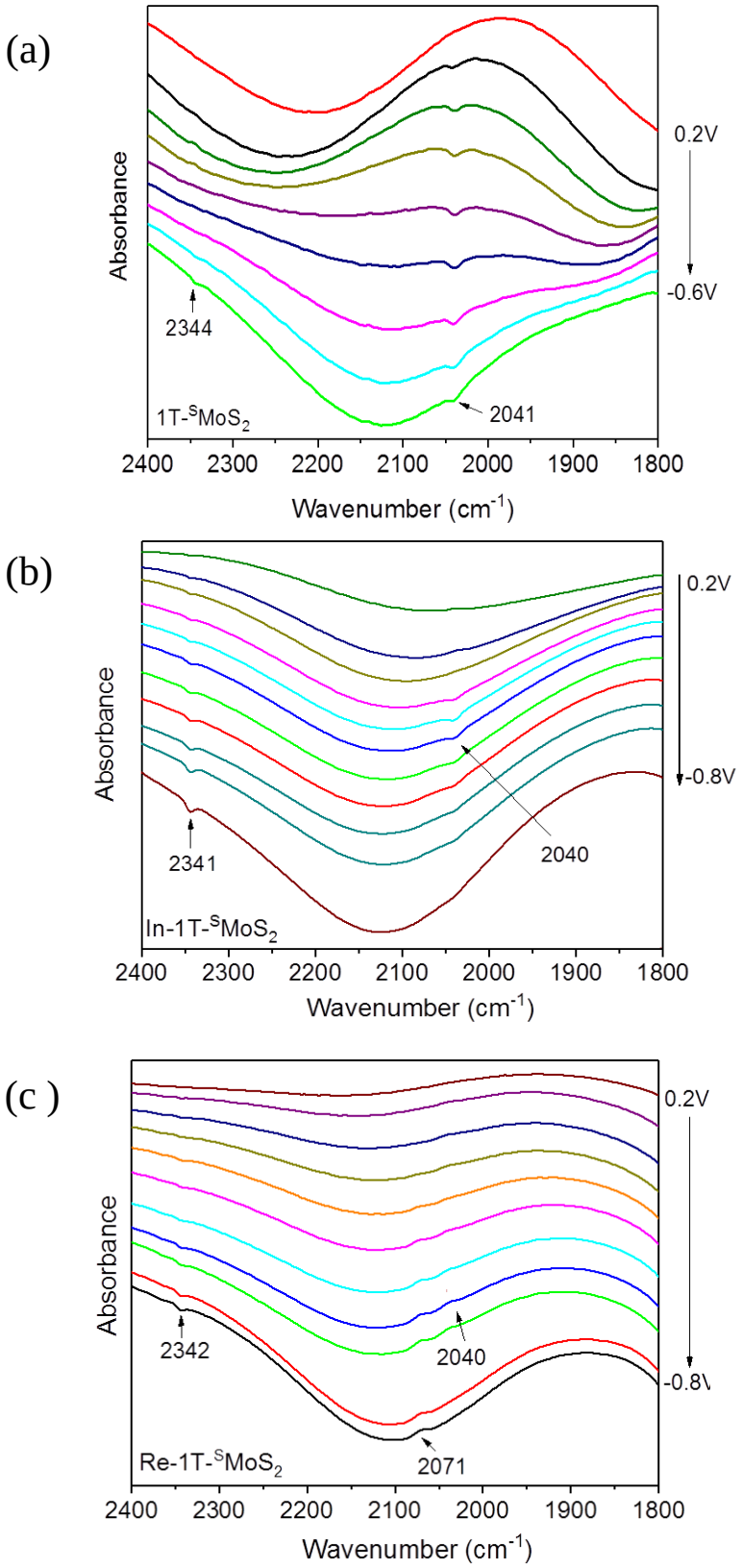


Figure 5.8 Real-time ATRIR spectra from 1800-2400 cm^{-1} recorded during cathodic scans of different 1T-$^{S}MoS_2$ materials in a CO_2-satuated 0.5M $KHCO_3$ solution as compared with background.

The electrochemical system was coupled with an in-situ Fourier-transform infrared spectrometer (FTIR) to study the electrochemical interface in real time. According to the literature, chemisorbed *CO can be detected as a broad and asymmetric band located between 2100 cm^{-1} and 1900 cm^{-1} at an applied potential lower than -0.4 V versus RHE in a CO_2-saturated bicarbonate-based electrolyte[18–20]. Due to the use of aqueous electrochemical cell, our IR spectra were severely interference by the large water peaks at around 3500 cm^{-1} and 1600 cm^{-1}. Despite this interference, we were still able to detect the small but sharp, linearly absorbed *CO peak at around 2040 cm^{-1} in the broad chemisorbed *CO peak in all cases. Enlarged regions of ATR-IR spectra of each MoS_2 materials between 2400 cm^{-1} and 1800 cm^{-1} are presented in Figure 5.8. Interestingly, the chemisorpted CO* species on pristine 1T-MoS_2 can be detected even at 0V applied potential, which is progressively attenuated compared to the background at higher reduction potentials. (Figure 5.8a) This suggests that the 1T-$^{S}MoS_2$ can facilitate the *CO absorption in the presence of CO_2 under standard condition without the input of external energy. This is in accordance with the DFT results presented in previous work[6], which showed that formation of CO adsorption species is favourable on pure 1T-$^{S}MoS_2$. However, the calculation also points out that *CO is difficult to be desorbed back to electrolyte because of high energy barrier. This may suggest that the surface is easily fouled with a negligible CO_2 reducibility observed from previous LSV curve in Figure 5.7 before the strong cathodic reduction potentials are applied.

For In-1T-$^{S}MoS_2$ and Re-1T-$^{S}MoS_2$, the *CO broad adsorption bands can marginally be observed at around 2040 cm^{-1} in both spectra indicative of their higher reactivity with reference to the gas CO peak with the lowest potential applied (Figure 5.8 b and c). However, there appears a progressive consumption compared to background at higher

potentials. Another *CO band can be detected at 2071 cm^{-1} at higher potentials in the Re-1T-$^{S}MoS_2$ spectra, suggesting a related product(s) could be presented. Similar to the literatures aforementioned, both of the chemisorbed *CO bands emerged at -0.2 V with a growing intensity. Their intensity then reached the maxima at around -0.6 V and started to drop beyond this point. These two potential values are also consistent with the position of shoulder peaks in the LSV curves illustrated in Figure 5.7. This indicated that *CO started to accumulate on both surface at around -0.2V while the onset of generation of alcohols/hydrocarbons was triggered at around -0.6V [19,20]. Based on the results, we can describe the CO_2RR is a potential dependent reaction when catalysed by In-1T-$^{S}MoS_2$ and Re-1T-$^{S}MoS_2$. It should be noted that since metallic 1T-$^{S}MoS_2$ has been demonstrated as a decent HER catalyst in Chapter 4, H_2 gas bubbles would start to evolve at the electrode surface when the applied potential goes beyond -0.6V. Thus, the IR spectrum for 1T-$^{S}MoS_2$ had been severely affected, so the measurement was ceased at this point. The competitive hydrogen production happened for In-1T-$^{S}MoS_2$ and Re-$^{S}MoS_2$ when potential was beyond -0.8V.

5.5. Product Analysis by Liquid ^{1}H NMR

Chronoamperometry scans were carried out for 5400 s (vs RHE) for all three samples. Analysis of gaseous product(s) was attempted by coupling the electrochemical system to a gas chromatography spectrometer. Unfortunately, no signals for any gaseous products could be detected in the potential range from -0.2 to − 1.0 V. In contrary, the liquid products in the electrolyte could be analysed and quantified by highly sensitive 700MHz H^1 liquid NMR spectroscopy (Bruker AVIII 700). (Figure5.9) 4,4-dimethyl-4-silapentane-1-sulfonic acid (DSS) was used as the internal reference due to its high water solubility. In the case of 1T-$^{S}MoS_2$, no liquid products (or a very trace amount that is below the detection limit) could be detected at both potential -0.6V and -0.8V.

(Figure5.9c) The Faradic efficiency (FE) of detected products for In-1T-$^{S}MoS_2$ and Re-1T-$^{S}MoS_2$ was listed in table 5.1. Repeated example experiments suggested that these products are not a result of contaminations. For Re doped sample, the results showed that a surprisingly large amount of C_4 t-butanol was detected as the major product. It was previously reported by Francis and co-workers that t-butanol was a minor product (FE <1%) of electrochemical CO_2RR when catalysed by thin MoS_2 films with high basal surface area[21]. However, no further explanation or experimental/computational evidence was given regarding the reaction pathway. Acetone and formate could also be found in the electrolyte as minor products. (Figure 5.9a) While for In doped 1T-$^{S}MoS_2$, ethanol can be clearly detected as the major product instead of t-butanol and methanol, while formate and acetone were found as minor products. Overall, we can conclude that no liquid products could be detected in the electrolyte of 1T-$^{S}MoS_2$, while CO_2 can be reduced into higher-order liquid alcohols when Re and In atoms are doped onto the basal sites of 1T-$^{S}MoS_2$.

Table 5.1 Faradaic Efficiency of Liquid Products

	Faradaic Efficiency of Liquid Products @-0.8V Vs RHE				
	Formate	Methanol	Ethanol	Acetone	t-butanol
Re-1T-$^{S}MoS_2$	0.13%	--	--	3.97%	8.51%
In-1T-$^{S}MoS_2$	0.20%	0.15%	3.50%	1.49%	--

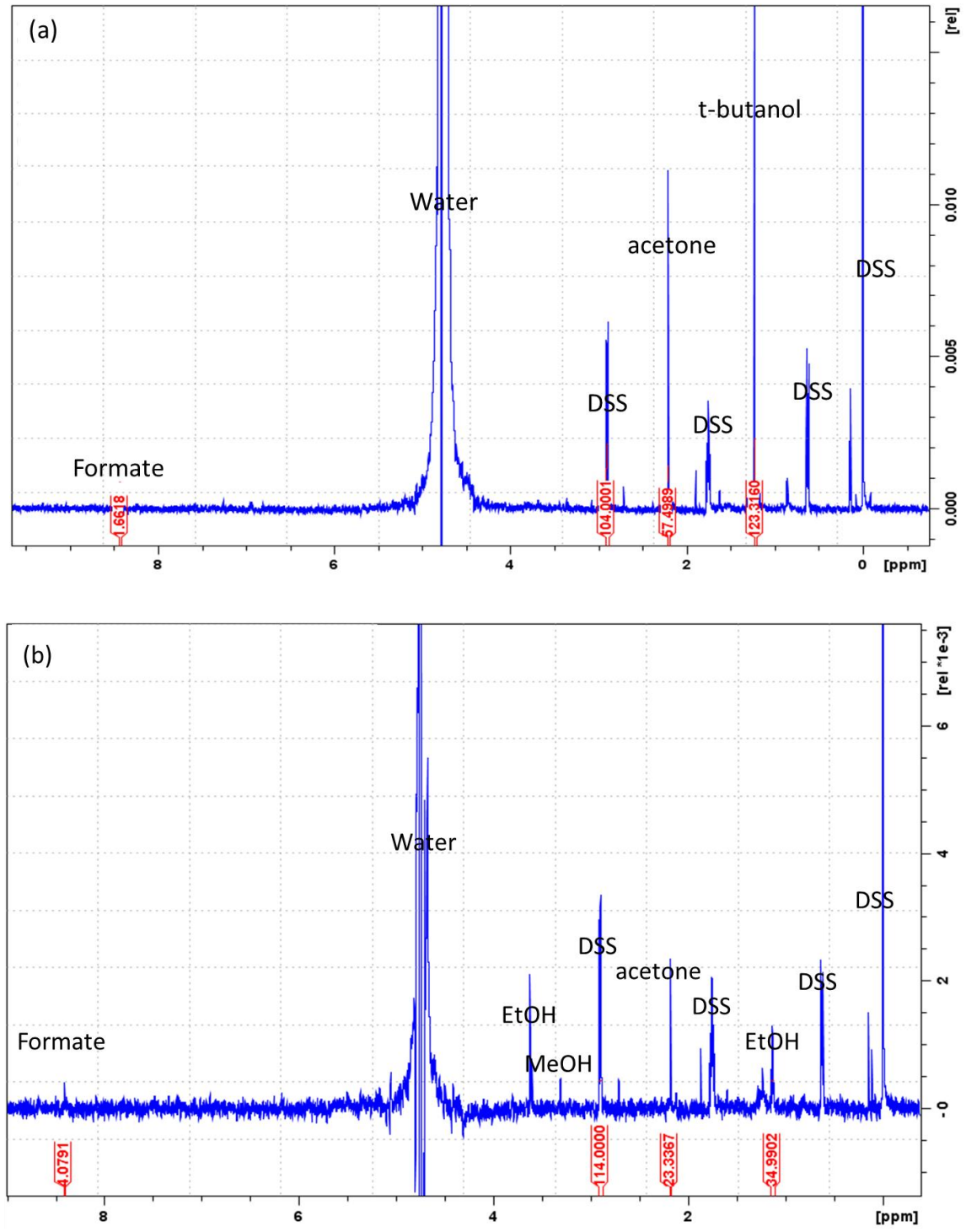
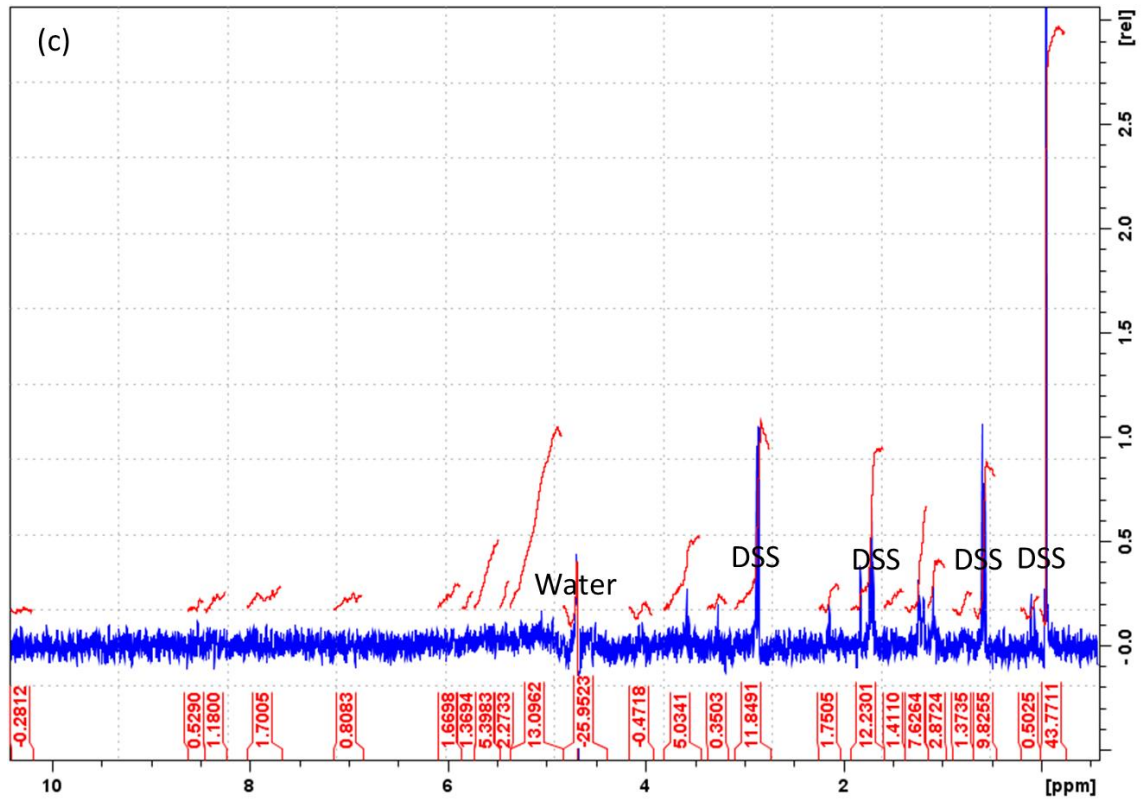


Figure 5.9 H^1 NMR spectra of 0.5M $KHCO_3$ electrolyte after undergoing chronoamperometry for 5400s at -0.8V with peaks assigned to corresponding liquid products. The working electrode was drop-casted with (a) Re-1T-$^{S}MoS_2$, (b) In-1T-$^{S}MoS_2$ (c) 1T-$^{S}MoS_2$. 4,4-dimethyl-4-silapentane-1-sulfonic acid (DSS) was used as the reference.



(Continued) Figure 5.9 H^1 NMR spectra of 0.5M $KHCO_3$ electrolyte after undergoing chronoamperometry for 5400s at -0.8V with peaks assigned to corresponding liquid products. The working electrode was drop-casted with (a) Re-1T-$^{S}MoS_2$, (b) In-1T-$^{S}MoS_2$ (c) 1T-$^{S}MoS_2$. 4,4-dimethyl-4-silapentane-1-sulfonic acid (DSS) was used as the reference.

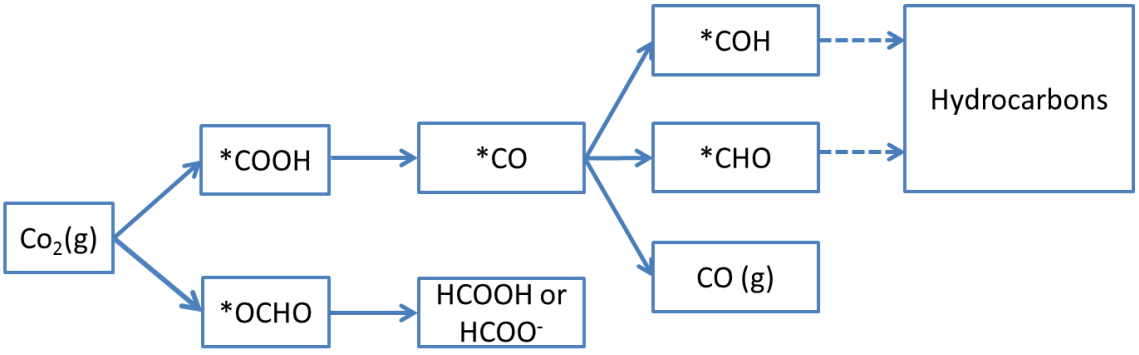


Figure 5.10 Simplified tree diagram for general reaction pathway for electrochemical CO_2RR.

5.6. The function of Re and In dopants on 1T-$^{S}MoS_2$ for electrochemical CO_2RR

5.6.1. Competitive Hydrogen Evolution Reaction

In the last chapter, we demonstrated that single metal doped 1T-$^{S}MoS_2$ materials behave as bifunctional catalysts in hydrogen production. H adsorption takes place at the basal metallic S sites and the absorbed H then hopped to the dopant atoms for the Tafel recombination step. Since hydrogen evolution reaction is the competitive reaction in aqueous condition, we compute the Tafel barriers for recombinative H_2 desorption from Re-1T-$^{S}MoS_2$ and In-1T-$^{S}MoS_2$ using the same computational method described in Chapter 4.6.2. Unlike Pt and Pd atoms, the activation energy for the Tafel step is increased from 1.15 eV on undoped 1T-$^{S}MoS_2$ to 1.35 eV on Re-1T-$^{S}MoS_2$.This suggested that HER reaction is not favourable on the Re atoms. For In atoms, the Tafel mechanism from the state where 2 x H are bound to In is actually endothermic by 1.25 eV. This may suggest that it is extremely favourable for H_2 to recombine from this state. However, the reason this step is endothermic by such a large amount is that H is very unstable on In atom. If two protons adsorb to two S sites of 1T-$^{S}MoS_2$ and then diffuse to the In atom, there is a reaction barrier of 1.47 eV making this step extremely unfavourable. Therefore, In does not promote HER through the Tafel mechanism as H will not bind to the In atom. Moreover, the unstable binding of H on In will also make the Volmer step slow. In summary, both the presence of Re and In atoms on the basal planes of 1T-$^{S}MoS_2$ do not facilitate hydrogen production and the doping might even reduce the overall HER activity as the amount of S atoms available for H adsorption are reduced during the process. This justifies that the two metal dopants on 1T-$^{S}MoS_2$ are found to be able to catalyse the CO_2RR at the expense of HER.

5.6.2. Reducing Adsorbed CO

Initially, we plan to incorporate Re and In atoms onto 1T-$^{S}MoS_2$ because they are expected to facilitate CO_2 adsorption onto the basal plane due to π back donation of their filled electrons[22–24]. However, we do not expect that the CO_2 can already be readily absorbed onto pure MoS_2 to form *CO even without input of external energy. From the NMR results, we are able to detect a small amount of formate (FE<1%) for both Re- and In-doped sample as well. Since formate are generated via the formation of the *$HCOO^-$ (or *$OCHO^-$) intermediate instead of *CO, this indicates that In and Re atoms did facilitate *$HCOO^-$ in contrary to pure 1T-$^{S}MoS_2$. More importantly, both Re and In doped samples can trigger the formation of high-order alcohols, as indicated by the NMR spectra, while this cannot be observed for undoped MoS_2. Adsorbed carbon monoxide (*CO) is the common intermediate for all alcoholic products in CO_2RR. Therefore, the disappearance of *CO bands in the IR spectrum of Re-1T-$^{S}MoS_2$ and In-1T-$^{S}MoS_2$ at -0.8 V would suggest that these *CO are possibly reduced into *CHO and then ultimately alcohols and other hydrocarbons like acetone because more electrons were provided to the reaction interface. (Figure 5.10) The results indirectly suggested that the formation of *CHO from *CO is possibly the rate-determining step for pure $^{S}MoS_2$ but not the doped ones, indicating that the Re and In dopants can at least facilitate the reaction step involving the reduction of *CO into *CHO in the whole reduction mechanism.

5.7. Conclusions

From the experimental results, we can conclude that single Re and In dopants can be once again incorporated onto exfoliated 1T-$^{S}MoS_2$ monolayers. Despite the low doping concentration, the CO_2RR activity of the two doped samples is shown to be significantly superior to that of their pristine counterpart. The presence of two shoulder peaks on their LSV curves indicates the possibility of a multiple-step reduction process. Further surface analysis by in-situ FTIR-potentiostat system revealed that the reaction catalysed by Re and In doped MoS_2 is potential dependent. Adsorbed carbon monoxide is expected to be further reduced to higher hydrocarbon, which is unobservable for the monolayers. This is further confirmed by NMR spectra that the high-order alcohols are produced as the major products with a reasonable Faradaic efficiency. The roles of the dopants are also investigated. Computational simulations suggested that the doping configurations of these two atoms are different from that of Pt and Pd atoms. The Re and In dopants do not encourage competitive hydrogen product, unlike Pt and Pd atoms investigated in early chapters. Instead, they facilitate rate-determining hydrogenation of adsorbed carbon monoxide into hydrocarbons as compared to unmodified MoS_2. Overall, we have reconfirmed that 1T-MoS_2 functionalised by single atoms can be tailored into efficient electrocatalyst for different electrochemical applications in the energy industries.

5.8. References

(1) Ma, J.; Sun, N.; Zhang, X.; Zhao, N.; Xiao, F.; Wei, W.; Sun, Y. A Short Review of Catalysis for CO2 Conversion. *Catal. Today* **2009**, *148*, 221–231.

(2) Cuéllar-Franca, R. M.; Azapagic, A. Carbon Capture, Storage and Utilisation Technologies: A Critical Analysis and Comparison of Their Life Cycle Environmental Impacts. *J. CO2 Util.* **2015**, *9*, 82–102.

(3) Ipcc, W. G. I. Climate Change 2007: The Physical Science Basis Contribution of Working Group I. *Fourth Assess. Rep. Intergov. panel Clim. Chang. Cambridge Univ. Press. Cambridge* **2007**.

(4) Schouten, K. J. P.; Kwon, Y.; Van Der Ham, C. J. M.; Qin, Z.; Koper, M. T. M. A New Mechanism for the Selectivity to C1and C2species in the Electrochemical Reduction of Carbon Dioxide on Copper Electrodes. *Chem. Sci.* **2011**, *2*, 1902–1909.

(5) Jhong, H. R. M.; Ma, S.; Kenis, P. J. Electrochemical Conversion of CO2 to Useful Chemicals: Current Status, Remaining Challenges, and Future Opportunities. *Curr. Opin. Chem. Eng.* **2013**, *2*, 191–199.

(6) Abbasi, P.; Asadi, M.; Liu, C.; Sharifi-Asl, S.; Sayahpour, B.; Behranginia, A.; Zapol, P.; Shahbazian-Yassar, R.; Curtiss, L. A.; Salehi-Khojin, A. Tailoring the Edge Structure of Molybdenum Disulfide toward Electrocatalytic Reduction of Carbon Dioxide. *ACS Nano* **2017**, *11*, 453–460.

(7) Xu, J.; Li, X.; Liu, W.; Sun, Y.; Ju, Z.; Yao, T.; Wang, C.; Ju, H.; Zhu, J.; Wei, S.; Xie, Y. Carbon Dioxide Electroreduction into Syngas Boosted by a Partially Delocalized Charge in Molybdenum Sulfide Selenide Alloy Monolayers. *Angew. Chemie - Int. Ed.* **2017**, *56*, 9121–9125.

(8) Kresse, G.; Furthmu, J. Efficient Iterative Schemes for Ab Initio Total-Energy

Calculations Using a Plane-Wave Basis Set ¨. **1996**, *54*.

(9) Kresse, G.; Furthmiiller, J. Efficiency of Ab-Initio Total Energy Calculations for Metals and Semiconductors Using a Plane-Wave Basis Set Av *. **1996**, *6*, 15–50.

(10) Kresse, G.; Joubert, D. From Ultrasoft Pseudopotentials to the Projector Augmented-Wave Method. **1999**, *59*, 11–19.

(11) Blöchl, P. E. Projector Augmented-Wave Method. *Phys. Rev. B* **1994**, *50*.

(12) Perdew, J. P.; Burke, K.; Ernzerhof, M. Generalized Gradient Approximation Made Simple. **1996**, No. 3, 3865–3868.

(13) Hu, T.; Li, R.; Dong, J. A New (2 × 1) Dimerized Structure of Monolayer 1T-Molybdenum Disulfide, Studied from First Principles Calculations. *J. Chem. Phys.* **2013**, *139*.

(14) Henkelman, G.; Jónsson, H. Improved Tangent Estimate in the Nudged Elastic Band Method for Finding Minimum Energy Paths and Saddle Points. **2016**, *9978*.

(15) Henkelman, G.; Jónsson, H. A Dimer Method for Finding Saddle Points on High Dimensional Potential Surfaces Using Only First Derivatives. **2010**, *7010*.

(16) Henkelman, G.; Jo, H. A Climbing Image Nudged Elastic Band Method for Finding Saddle Points and Minimum Energy Paths and Minimum Energy Paths. **2014**, *9901*.

(17) Lukowski, M. A.; Daniel, A. S.; Meng, F.; Forticaux, A.; Li, L.; Jin, S. Enhanced Hydrogen Evolution Catalysis from Chemically Exfoliated Metallic MoS2 Nanosheets. *J. Am. Chem. Soc.* **2013**, *135*, 10274–10277.

(18) Zhu, S.; Li, T.; Cai, W. Bin; Shao, M. CO2 Electrochemical Reduction As Probed through Infrared Spectroscopy. *ACS Energy Lett.* **2019**, *4*, 682–689.

(19) Wuttig, A.; Liu, C.; Peng, Q.; Yaguchi, M.; Hendon, C. H.; Motobayashi, K.; Ye, S.; Osawa, M.; Surendranath, Y. Tracking a Common Surface-Bound Intermediate

during CO2-to- Fuels Catalysis. *ACS Cent. Sci.* **2016**, *2*, 522–528.

(20) Zhu, S.; Jiang, B.; Cai, W. Bin; Shao, M. Direct Observation on Reaction Intermediates and the Role of Bicarbonate Anions in CO2 Electrochemical Reduction Reaction on Cu Surfaces. *J. Am. Chem. Soc.* **2017**, *139*, 15664–15667.

(21) Francis, S. A.; Velazquez, J. M.; Ferrer, I. M.; Torelli, D. A.; Guevarra, D.; McDowell, M. T.; Sun, K.; Zhou, X.; Saadi, F. H.; John, J.; Richter, M. H.; Hyler, F. P.; Papadantonakis, K. M.; Brunschwig, B. S.; Lewis, N. S. Reduction of Aqueous CO 2 to 1-Propanol at MoS 2 Electrodes. *Chem. Mater.* **2018**, *30*, 4902–4908.

(22) Kaneco, S.; Iwao, R.; Iiba, K.; Itoh, S. I.; Ohta, K.; Mizuno, T. Electrochemical Reduction of Carbon Dioxide on an Indium Wire in a KOH/Methanol-Based Electrolyte at Ambient Temperature and Pressure. *Environ. Eng. Sci.* **1999**, *16*, 131–137.

(23) White, J. L.; Bocarsly, A. B. Enhanced Carbon Dioxide Reduction Activity on Indium-Based Nanoparticles. *J. Electrochem. Soc.* **2016**, *163*, H410–H416.

(24) Oh, S.; Gallagher, J. R.; Miller, J. T.; Surendranath, Y. Graphite-Conjugated Rhenium Catalysts for Carbon Dioxide Reduction. *J. Am. Chem. Soc.* **2016**, *138*, 1820–1823.

Chapter 6

Conclusions and Future Works

Two-dimensional materials and single atom catalyst are two emerging frontiers in heterocatalysis. Their combination endows this new type of catalysts with enormous potential. The thesis thus demonstrated a chronological approach to functionalise monolayer molybdenum disulphide with single metal atoms for electrocatalytic applications with the support of state-of-the-art analytical techniques and computational simulations.

Naturally available semiconducting molybdenum disulphide was first exfoliated into monolayers. We then provided the direct experimental evidence that different single atoms can be chemically attached to the basal surface of the as-prepared monolayers. Electrochemical testing and spectroscopic results suggested that Ni and Co atoms show opposite doping behaviour even though they are neighbours in the periodic table. In-depth comprehension on the structural and electronic properties of these dopants are further examined experimentally and computationally, which confirmed that geometric and electronic factors exerted by transition metal dopants can alternate the hydrogen affinity of surrounding sulphur at the basal plane in hydrogen production. With this knowledge, we moved to investigate the electrocatalytic activity of metallic molybdenum disulphide monolayers, which was not well studied at that time due to the instability of this polytype. We developed a new synthetic method to chemically attach single transition metals to this metallic polytype by a mild radical assisted reduction of metal precursors using sonication at ambient condition. Electrochemical analysis showed that the catalytic ability in hydrogen production of as-prepared samples is far superior to that of our doped semiconducting

molybdenum disulphide. Further experimental and computational investigation of the structural and electronic properties via a comparative study between Pt and Pd dopants revealed that the inclusion of single doper can offer the dramatic acceleration on the rate limiting recombination of adsorbed hydrogen on the sulphur at the basal plane. We thus demonstrated that this composite structure can act as a bifunctional catalysis for hydrogen production. It also showed dopants played a different role when decorated on different polytypes of molybdenum disulphide. Since we discovered a highly active and cost-effective catalyst that can possibly be tailored for different electrocatalytic reactions, we would like to reassure this by extending the scope to study its electrocatalytic activity for carbon dioxide reduction. Electrochemical testing coupled with real time spectroscopic technique suggested that incorporation of Re and In dopants can facilitate multiple-step reduction processes with enhanced electrical performance. Product analysis confirmed that the presence of high-order alcohols which cannot be observed in the case of the undoped catalyst. Overall, we have provided in-depth characterisations and theoretical calculations at atomic level on these doped molybdenum disulphide monolayer materials for electrochemical applications. It is hoped that these results in this thesis can provide important references for the future design of other single atom catalyst on two-dimensional materials.

Since the research projects in this thesis are mainly focused on comparative study between two selected dopants, the trend of geometric and electronic properties exerted by transition metal atoms has yet to be fully investigated. Future works with more experimental and computational studies on transition metals dopants across a period of elements in the periodic table for both molybdenum disulphide polytypes can be conducted. The reaction mechanism of carbon dioxide reduction is much more complex than that of hydrogen production. Constructing free energy plot will be beneficial to understand the whole reaction pathway.

The competitive hydrogen production can be supressed in non-aqueous electrolyte. Thus, we can optimise the reaction condition of electrochemical carbon dioxide reduction. It is also important to bridge the gap between these novel catalysts studied in the laboratory and the commercial catalyst used in industry. For this, we should investigate the catalytic performance of our doped molybdenum disulphide in commercial water electrolyser at real industrial settings.